ELSEVIER

Physics Reports 366 (2002) 331–405

PHYSICS REPORTS

www.elsevier.com/locate/physrep

The Alpha Magnetic Spectrometer (AMS) on the International Space Station: Part I – results from the test flight on the space shuttle

AMS Collaboration

M. Aguilar[a], J. Alcaraz[a], J. Allaby[b], B. Alpat[c], G. Ambrosi[c,d], H. Anderhub[e], L. Ao[f], A. Arefiev[g], P. Azzarello[d], E. Babucci[c], L. Baldini[h,i], M. Basile[h], D. Barancourt[j], F. Barao[k,l], G. Barbier[j], G. Barreira[k], R. Battiston[c], R. Becker[i], U. Becker[i], L. Bellagamba[h], P. Béné[d], J. Berdugo[a], P. Berges[i], B. Bertucci[c], A. Biland[e], S. Bizzaglia[c], S. Blasko[c], G. Boella[m], M. Boschini[m], M. Bourquin[d], L. Brocco[h], G. Bruni[h], M. Buénerd[j], J.D. Burger[i], W.J. Burger[c], X.D. Cai[i], C. Camps[n], P. Cannarsa[e], M. Capell[i,*], D. Casadei[h], J. Casaus[a], G. Castellini[h,o], C. Cecchi[c], Y.H. Chang[p], H.F. Chen[q], H.S. Chen[r], Z.G. Chen[f], N.A. Chernoplekov[s], T.H. Chiueh[p], K. Cho[t], M.J. Choi[u], Y.Y. Choi[u], Y.L. Chuang[v], F. Cindolo[h], V. Commichau[n], A. Contin[h], E. Cortina-Gil[d], M. Cristinziani[d], J.P. da Cunha[w], T.S. Dai[i], C. Delgado[a], J.D. Deus[e], N. Dinu[c,1], L. Djambazov[e], I. D'Antone[h], Z.R. Dong[x], P. Emonet[d], J. Engelberg[y], F.J. Eppling[i], T. Eronen[z], G. Esposito[c], P. Extermann[d], J. Favier[aa], E. Fiandrini[c], P.H. Fisher[i], G. Fluegge[n], N. Fouque[aa], Yu. Galaktionov[g,i], M. Gervasi[m], P. Giusti[h], D. Grandi[m], O. Grimms[e], W.Q. Gu[x], K. Hangarter[n], A. Hasan[e], V. Hermel[ad], H. Hofer[e], M.A. Huang[v], W. Hungerford[e], M. Ionica[c,1], R. Ionica[c,1], M. Jongmanns[e], K. Karlamaa[y], W. Karpinski[ab,5], G. Kenney[e], J. Kenny[c], D.H. Kim[t], G.N. Kim[t], K.S. Kim[u], M.Y. Kim[u], A. Klimentov[g,i], R. Kossakowski[aa], V. Koutsenko[g,i], M. Kraeber[e], G. Laborie[j], T. Laitinen[z], G. Lamanna[c], E. Lanciotti[a], G. Laurenti[h], A. Lebedev[i], C. Lechanoine-Leluc[d], M.W. Lee[t],

*Corresponding author.

E-mail address: michael.capell@cern.ch (M. Capell).

[1]Permanent address: HEPPG, Univ. of Bucharest, Romania.

[2]Permanent address: Nuclear Physics Institute, St. Petersburg, Russia.

[3]Now at National Institute for High Energy Physics, NIKHEF, NL-1009 DB Amsterdam, The Netherlands.

[4]Supported by ETH Zürich.

[5]Supported by the Deutsches Zentrum für Luft– und Raumfahrt, DLR.

[6]Supported by the National Natural Science Foundation of China.

PII: S0370-1573(02)00013-3

S.C. Lee[v], G. Levi[h], P. Levtchenko[c], C.L. Liu[ac], H.T. Liu[r], I. Lopes[w], G. Lu[f], Y.S. Lu[r], K. Lübelsmeyer[ab], D. Luckey[i], W. Lustermann[e], C. Maña[a], A. Margotti[h], F. Mayet[j], R.R. McNeil[ad], B. Meillon[j], M. Menichelli[c], A. Mihul[ae], A. Mourao[l], A. Mujunen[y], F. Palmonari[h], A. Papi[c], H.B. Park[t], W.H. Park[t], M. Pauluzzi[c], F. Pauss[e], E. Perrin[d], A. Pesci[h], A. Pevsner[af], M. Pimenta[k,l], V. Plyaskin[g], V. Pojidaev[g], M. Pohl[d], V. Postolache[c,1], N. Produit[d], P.G. Rancoita[m], D. Rapin[d], F. Raupach[ab], D. Ren[e], Z. Ren[v], M. Ribordy[d], J.P. Richeux[d], E. Riihonen[z], J. Ritakari[y], S. Ro[t], U. Roeser[e], C. Rossin[j], R. Sagdeev[ag], D. Santos[j], G. Sartorelli[h], C. Sbarra[h], S. Schael[ab], A. Schultz von Dratzig[ab], G. Schwering[ab], G. Scolieri[c], E.S. Seo[ag], J.W. Shin[t], V. Shoutko[i], E. Shoumilov[g], R. Siedling[ab], D. Son[t], T. Song[x], M. Steuer[i], G.S. Sun[x], H. Suter[e], X.W. Tang[r], Samuel C.C. Ting[i], S.M. Ting[i], M. Tornikoski[y], J. Torsti[z], J. Trümper[ah], J. Ulbricht[e], S. Urpo[y], E. Valtonen[z], J. Vandenhirtz[ab], F. Velcea[c,1], E. Velikhov[s], B. Verlaat[e,3], I. Vetlitsky[g], F. Vezzu[j], J.P. Vialle[aa], G. Viertel[e], D. Vité[d], H. Von Gunten[e], S. Waldmeier Wicki[e], W. Wallraff[ab], B.C. Wang[ac], J.Z. Wang[f], Y.H. Wang[v], K. Wiik[y], C. Williams[h], S.X. Wu[i,p], P.C. Xia[x], J.L. Yan[f], L.G. Yan[x], C.G. Yang[r], J. Yang[u], M. Yang[r], S.W. Ye[q,4], P. Yeh[v], Z.Z. Xu[q], H.Y. Zhang[ai], Z.P. Zhang[q], D.X. Zhao[x], G.Y. Zhu[r], W.Z. Zhu[f], H.L. Zhuang[r], A. Zichichi[h], B. Zimmermann[e], P. Zuccon[c]

[a] *Centro de Investigaciones Energéticas, Medioambientales y Tecnológicas, CIEMAT, E-28040 Madrid, Spain*[8]
[b] *European Laboratory for Particle Physics, CERN, CH-1211 Geneva 23, Switzerland*
[c] *INFN-Sezione di Perugia and Universitá Degli Studi di Perugia, I-06100 Perugia, Italy*[7]
[d] *University of Geneva, CH-1211 Geneva 4, Switzerland*
[e] *Eidgenössische Technische Hochschule, ETH Zürich, CH-8093 Zürich, Switzerland*
[f] *Chinese Academy of Launching Vehicle Technology, CALT, 100076 Beijing, China*
[g] *Institute of Theoretical and Experimental Physics, ITEP, Moscow, 117259 Russia*
[h] *University of Bologna and INFN-Sezione di Bologna, I-40126 Bologna, Italy*[7]
[i] *Massachusetts Institute of Technology, Cambridge, MA 02139, USA*
[j] *Institut des Sciences Nucleaires, IN2P3/CNRS, F-38026 Grenoble, France*
[k] *Laboratorio de Instrumentacao e Fisica Experimental de Particulas, LIP, P-1000 Lisboa, Portugal*
[l] *Instituto Superior Técnico, IST, P-1096 Lisboa, Portugal*
[m] *INFN-Sezione di Milano, I-20133 Milan, Italy*[7]
[n] *III. Physikalisches Institut, RWTH, D-52056 Aachen, Germany*[5]
[o] *CNR–IROE, I-50125 Florence, Italy*
[p] *National Central University, Chung-Li, Taiwan 32054*
[q] *Chinese University of Science and Technology, USTC, Hefei, Anhui 230 029, China*[6]
[r] *Institute of High Energy Physics, IHEP, Chinese Academy of Sciences, 100039 Beijing, China*[6]
[s] *Kurchatov Institute, Moscow, 123182 Russia*
[t] *CHEP, Kyungpook National University, 702-701 Daegu, South Korea*
[u] *Ewha Womens University, 120-750 Seoul, South Korea*
[v] *Academia Sinica, Taipei 11529, Taiwan*
[w] *Laboratorio de Instrumentacao e Fisica Experimental de Particulas, LIP, P-3000 Coimbra, Portugal*

[7] Also supported by the Italian Space Agency.
[8] Also supported by the Comisión Interministerial de Ciencia y Tecnología.

[x] Institute of Electrical Engineering, IEE, Chinese Academy of Sciences, 100080 Beijing, China
[y] Helsinki University of Technology, FIN-02540 Kylmala, Finland
[z] University of Turku, FIN-20014 Turku, Finland
[aa] Laboratoire d'Annecy-le-Vieux de Physique des Particules, LAPP, F-74941 Annecy-le-Vieux CEDEX, France
[ab] I. Physikalisches Institut, RWTH, D-52056 Aachen, Germany[5]
[ac] Chung–Shan Institute of Science and Technology, Lung-Tan, Tao Yuan 325, Taiwan
[ad] Louisiana State University, Baton Rouge, LA 70803, USA
[ae] Institute of Microtechnology, Politechnica University of Bucharest and University of Bucharest, R-76900 Bucharest, Romania
[af] Johns Hopkins University, Baltimore, MD 21218, USA
[ag] University of Maryland, College Park, MD 20742, USA
[ah] Max–Planck Institut für extraterrestrische Physik, D-85740 Garching, Germany
[ai] Center of Space Science and Application, Chinese Academy of Sciences, 100080 Beijing, China

Received 1 October 2001
editor: J.V. Allaby

Abstract

The Alpha Magnetic Spectrometer (AMS) was flown on the space shuttle *Discovery* during flight STS-91 (June 1998) in a 51.7° orbit at altitudes between 320 and 390 km.

A search for antihelium nuclei in the rigidity range 1–140 GV was performed. No antihelium nuclei were detected at any rigidity. An upper limit on the flux ratio of antihelium to helium of $< 1.1 \times 10^{-6}$ was obtained.

The high energy proton, electron, positron, helium, antiproton and deuterium spectra were accurately measured.

For each particle and nuclei two distinct spectra were observed: a higher energy spectrum and a substantial second spectrum. Positrons in the second spectrum were found to be much more abundant than electrons. Tracing particles from the second spectra shows that most of them travel for an extended period of time in the geomagnetic field, and that the positive particles (p and e^+) and negative ones (e^-) originate from two complementary geographic regions. The second helium spectrum flux over the energy range 0.1–1.2 GeV/nucleon was measured to be $(6.3 \pm 0.9) \times 10^{-3} (m^2\ s\ sr)^{-1}$. Over 90 percent of the helium flux was determined to be ^{3}He at the 90% confidence level.

PACS: 95.55.−n

Contents

1. Introduction

The apparent absence of antimatter (antihelium, anticarbon, etc.) in the universe is one of the great puzzles in particle physics. Theories [1] which predict either the existence of antimatter in segregated domains or the total absence of antimatter have no firm foundation in experimental data. The existence (or absence) of antimatter nuclei in space is closely connected with the foundation of the theories of elementary particle physics, CP-violation, baryon number non-conservation, Grand Unified Theory (GUT), etc. Balloon-based cosmic ray searches for antinuclei at altitudes up to 40 km have been carried out for more than 20 years; all such searches have been negative [2,3]. The absence of annihilation gamma ray peaks excludes the presence of large quantities of antimatter within a distance of the order of 10 Mpc from the Earth. Baryogenesis models are not yet supported by particle physics experimental data. To date baryon non-conservation and large levels of CP-violation have not been observed.

Cosmological observations show that the matter of the universe is mostly dark matter. If dark matter, or a fraction of it, is non-baryonic and consists of almost non-interacting particles like neutralinos, it can be detected in cosmic rays through its annihilation into positrons or antiprotons, resulting in deviations (in the case of antiprotons) or structures (in the case of positrons) to be seen in the otherwise predictable cosmic ray spectra (see [4] and references therein).

The search for antimatter and dark matter is greatly facilitated if the search is performed outside the Earth's atmosphere. The Alpha Magnetic Spectrometer (AMS) [5] is the first large acceptance magnetic spectrometer to perform a high statistics study of cosmic particles in the background free

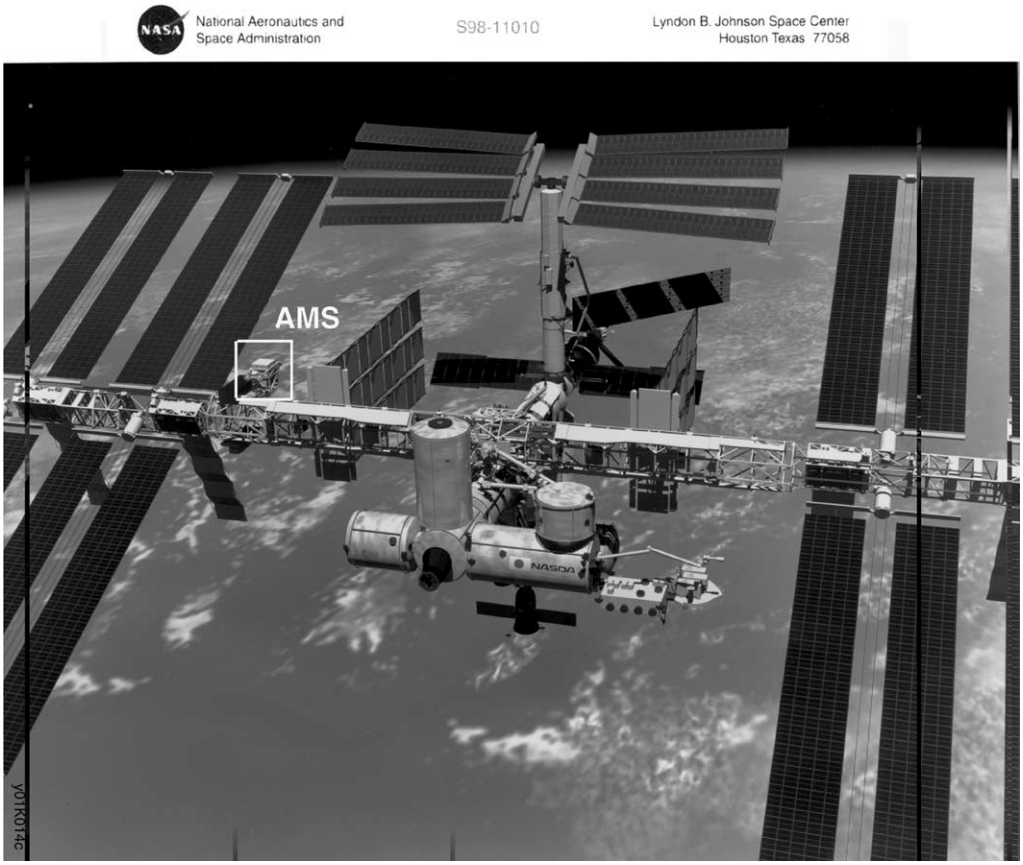

Fig. 1.1. A TeV detector in space: AMS-02 on the International Space Station.

environment of a space flight. The AMS experiment [6] has as its main objective to improve our knowledge in this physics domain.

In the year 2005, the AMS detector will be installed on the International Space Station (ISS) (Fig. 1.1). The mission is scheduled to last for 3–5 years. Fig. 1.2a shows the AMS-02 detector for the Space Station. It contains the following main components:

(1) A 20 layer Transition Radiation Detector (TRD) to identify positrons with a rejection factor of 10^2–10^3 against hadrons from 1.5 to 300 GeV.
(2) Four layers of Time of Flight (TOF) hodoscopes to provide precision time of flight measurements ($\sim$ 120 ps), $\mathrm{d}E/\mathrm{d}x$ measurements and the primary trigger.
(3) The superconducting magnet which provides a bending power of $BL^2 = 0.86\ \mathrm{Tm}^2$.
(4) Eight layers (6.45 m^2) of double-sided silicon tracker which provide a coordinate resolution of 10 μm in the bending plane and 30 μm in the non-bending plane.
(5) Veto counters to ensure that only particles passing the magnet aperture will be accepted.
(6) A Ring Imaging Čerenkov Counter (RICH) which measures the velocity (to 0.1% accuracy) of particles or nuclei and $|Q|$. This information, together with the measurement of momentum in the magnet, will enable AMS to directly measure the mass of particles and nuclei.

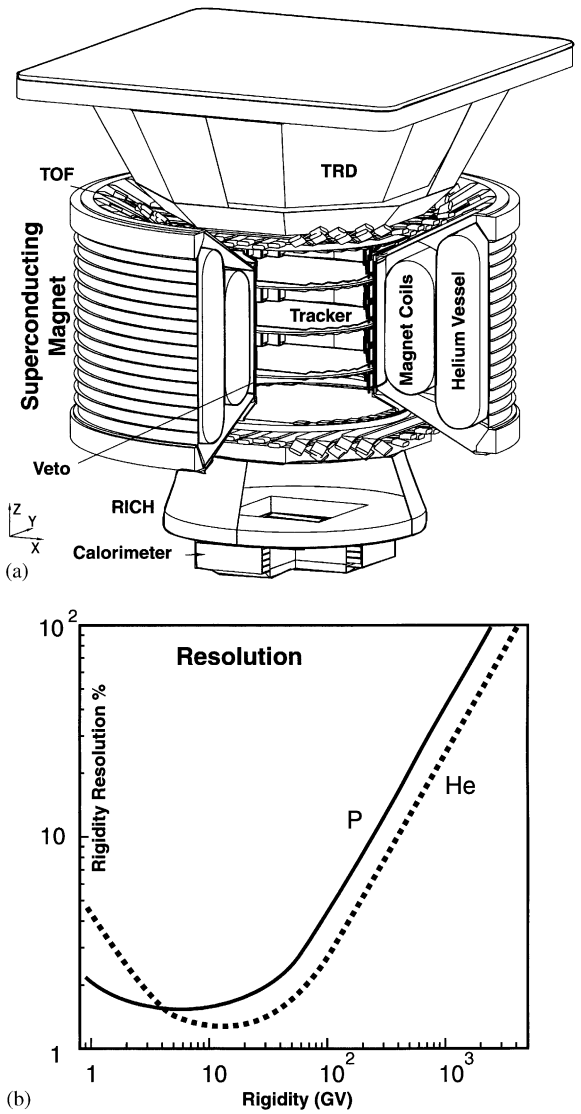

Fig. 1.2. (a) AMS-02 schematic. (b) Rigidity resolution of p and He in AMS-02.

(7) A 3-D sampling calorimeter (ECAL) made out of $15X_0$ of lead and plastic fibers to measure the energy of gamma rays, electrons and positrons and to distinguish electrons and positrons from hadrons with a rejection of 10^4 in the range 1.5 GeV–1 TeV.

Thus the value of the particle charge $|Q|$ is measured independently in the Tracker, RICH and TOF. The signed charge ($\pm Q$) and the momentum of the particle are measured by the 8 layers of double-sided silicon tracker in the magnet. The velocity, β, is measured by the TOF, TRD and RICH. Hadron rejection is provided by TRD and ECAL.

The detector is designed with the following properties:

(a) Minimal material in the particle trajectory so that the material itself is not a source of background nor a source of large angle nuclear scattering.
(b) Many repeated measurements of momentum and velocity so as to ensure that particles which experience large angle nuclear scattering within the detector be swept away by the spectrometer and not confused with the signal.
(c) A solid angle of 0.5 m^2 sr for the $\overline{He}$ search.
(d) Hadron/positron rejection of $> 10^6$.
(e) $\Delta\beta/\beta = 0.1\%$ to distinguish ^{9}Be, ^{10}Be, and ^{3}He, ^{4}He isotopes.
(f) A proton rigidity, R, resolution of 20% at 0.5 TV and a helium resolution of 20% at 1 TV, as seen in Fig. 1.2b, where $R = pc/|Z|e$ (GV).

Prior to the main mission an engineering precursor flight using a prototype of AMS, AMS-01, was flown on the space shuttle (STS-91, June 1998). The goal of the flight was to test the spectrometer design principles and to gain experience in the operation of the detector under real space flight conditions. According to a NASA-DOE agreement, the main purpose of AMS-01 is an engineering test flight to comply with NASA safety regulations to ensure that the design and construction of the high-energy physics detector can safely operate in space. For the AMS group, we also wanted to measure all the particle rates so as to refine the AMS-02 experiment on the space station. No effort was made to select especially high energy $e^{\pm}$ or low energy antiprotons. This will be done with the AMS-02 detector.

During the 10 day mission a vast amount of data on the fluxes of different cosmic particles in near Earth orbit was collected. In this report, we summarize the physics results from the precursor mission. First a description of the experimental apparatus and the performance of different subdetectors are given. Special attention is paid to the requirements arising from space flight and space environment conditions. Improved limits on the presence of antimatter in space are reported. Results on the measurements of the different particle fluxes are presented and discussed.

The knowledge obtained in the precursor flight is being used extensively in the redesign and construction of the spectrometer for the space station mission.

2. AMS-01 detector

The detector design principles and limitations as well as main construction techniques of the precursor flight version were reported in earlier publications [5,6]. In this report the essential performance characteristics will be given with short descriptions of the subsystems. Fig. 2.1 schematically shows the AMS detector elements: A permanent magnet with silicon microstrip tracker planes, scintillation counter hodoscopes above and below the magnet, two layers of a threshold Čerenkov counter and veto counters covering the inner surface of the magnet. Fig. 2.2 shows how the different detector parts were integrated together. Since the assembly must withstand the acceleration and vibrational loads of the shuttle launch and landing, the detector elements underwent a complicated procedure of "space qualification" which included vibration and thermo-vacuum tests as well as the proper choice of construction materials and mechanical design with first natural frequency well above the Space Shuttle first eigenfrequency of < 50 Hz.

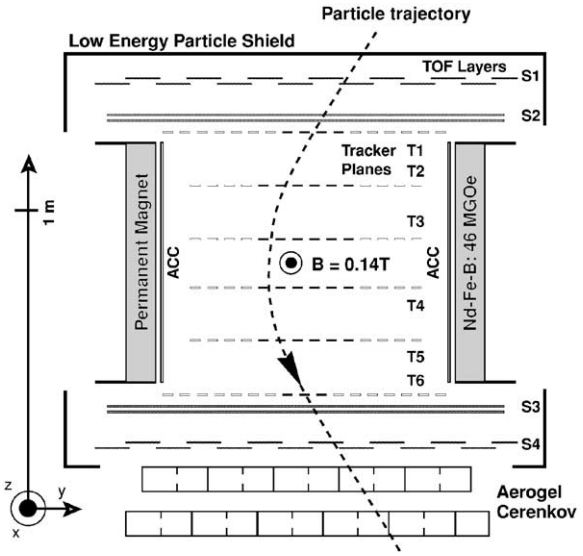

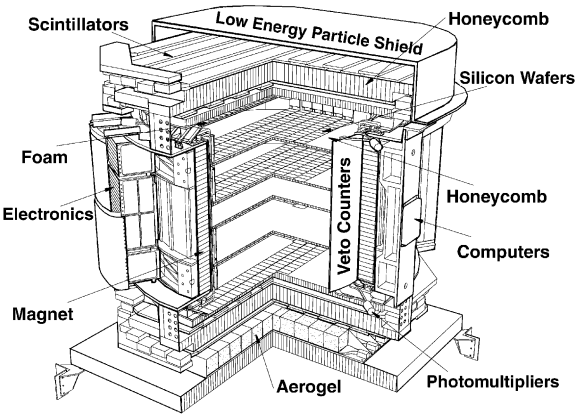

Fig. 2.1. Schematic view of AMS as flown on STS-91 showing the cylindrical permanent magnet, the silicon microstrip tracker planes T1–T6, the time of flight (TOF) hodoscope layers S1–S4, the aerogel Čerenkov counter, the anticoincidence counters (ACC) and the low energy particle shields (LEPS).

Fig. 2.2. Iso-view of the AMS detector. Some construction elements such as honeycomb and foam are shown as well as the position of the electronics crates.

2.1. Magnet

The choice of a permanent magnet and its design principles were reported in detail in Ref. [5]. The magnet has a cylindrical shape, a length of 800 mm, an inner diameter of 1115 mm and an outer diameter 1298 mm resulting in a geometrical acceptance of 0.82 m^2 sr. The magnet was made from 64 sectors. Each sector was composed of 100 $2'' \times 2'' \times 1''$ high-grade Nd–Fe–B blocks. Fig. 2.3 shows the arrangement of the field directions of the 64 sectors. We used the highest grade Nd–Fe–B blocks with an energy level of $(BH)_{\max} = 50 \times 10^6$ GOe. This configuration produced a dipole field of 1.5 kG and a negligible dipole moment.[9] Before the construction of full scale magnets, many smaller magnets were built to confirm and measure the field inside the magnet, the dipole moment and the flux leakage. Fig. 2.4 shows the dimensions of the AMS-01 flight magnet.

Three full scale magnets were built:

(a) The first magnet was used in acceleration and vibration tests for space qualification.
(b) The second magnet was the flight magnet.
(c) The third magnet was built without glue for NASA safety tests.

The design of the AMS magnet was carried out by MIT together with the Institute of Electrical Engineering of the Chinese Academy of Science, Beijing. The magnet, the supporting structure and space qualification testing were completed by the Institute of Electrical Engineering and the

[9] The Earth's magnetic field is 0.5 G. A strong dipole moment would result in an undesirable torque on the vehicle.

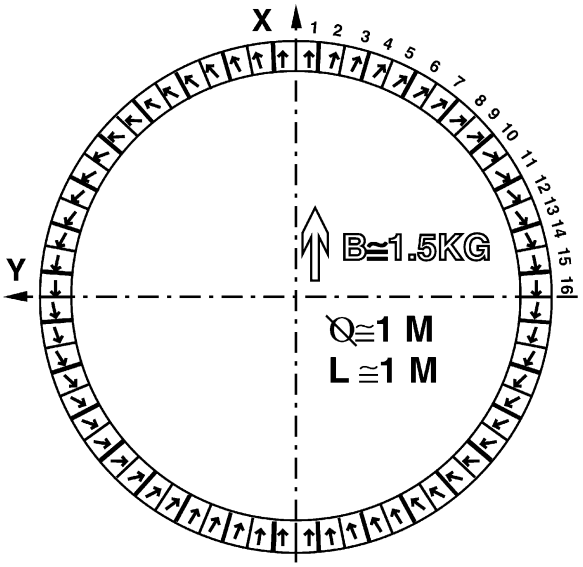

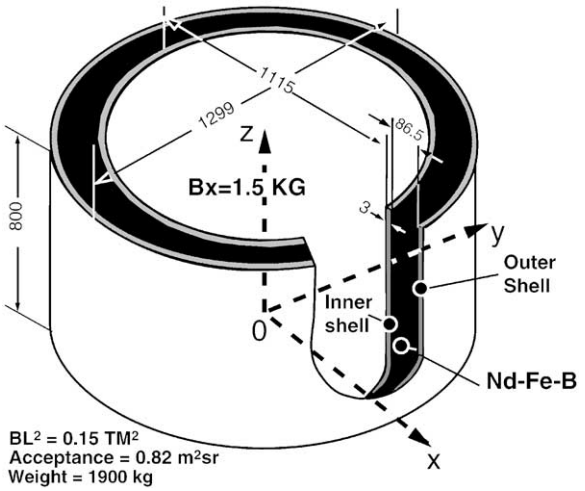

Fig. 2.3. Magnetic field orientation of the AMS-01 magnet sectors.

Fig. 2.4. Properties of the AMS flight magnet (dimensions in mm).

Chinese Academy of Launch Vehicle Technology (CALT). Fig. 2.5 shows the first magnet undergoing vibration testing. Fig. 2.6 shows it undergoing centrifuge testing up to 17.7g.

Fig. 2.7 shows the comparison of the sine sweep test results before and after the 17.7g centrifuge test. The test results indicate that there is no deformation in the detector before and after this test and that the eigenfrequency for the magnet is above the shuttle eigenfrequency of < 50 Hz.

The flight magnet was completed and transported to the Swiss Federal Institute of Technology (ETH) for integration on 15 March 1997. An independent team of specialists from CERN, together with ETH physicists, mapped the entire volume of the flight magnet and determined that the field agreed with the design value at the 1% level.

The third full scale magnet was built because of the lack of knowledge of the glue performance over an extended period in the space environment. We built this magnet without using any glue to be tested to destruction to ensure that AMS could be returned on the Shuttle to Earth even if the glue completely failed. Fig. 2.8 shows a schematic of the test procedure on the third magnet. The result of the test shows that, even with loads that were 3–10 times higher than what the stress analysis indicated were required to fail the structure, it would not break.

The total weight of the magnet including the support structure is 2.2 tons. The magnetic field is directed orthogonally to the cylinder longitudinal axis and the maximum bending power of the magnet is $BL^2 = 0.15\,\mathrm{Tm}^2$. The field drops down rather quickly outside the magnet to become less then 3 G anywhere at a distance of 2 m from the magnet center.[10] The variation of the main (bending) component of the field along the longitudinal magnet axis is shown in Fig. 2.9.

[10] NASA requires the leakage field to be < 60 G so as not to interfere with the life support system of the astronauts.

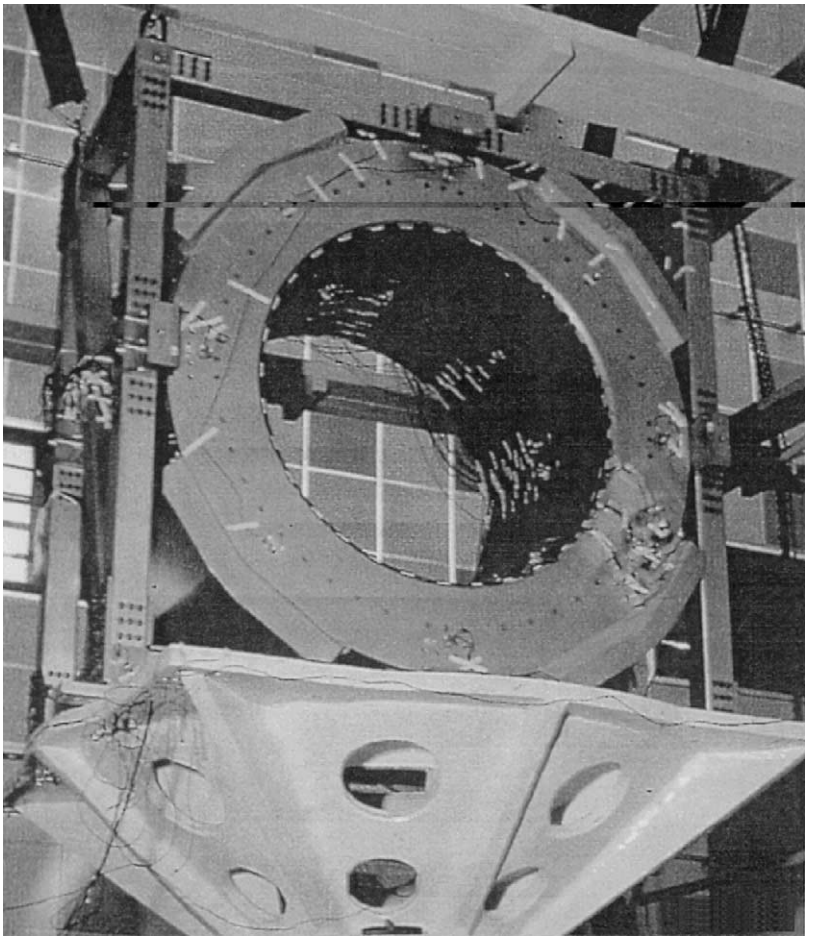

Fig. 2.5. AMS magnet undergoing vibration tests in Beijing.

2.2. Scintillation counter hodoscopes

The scintillation hodoscopes consist of four planes of coincidence counters (see Fig. 2.1), that is, two identical double planes (Fig. 2.10), situated at the top and the bottom of the magnet. A plane of counters consists of paddles of scintillators of different length. To avoid inefficiency in particle detection the adjacent paddles have a 5 mm overlap. The paddles of a double plane are orthogonal to each other to allow the measurement of two coordinates.

The system measures the time of flight (TOF), the absolute charge [7] and the direction (upward or downward) of charged particles. It also provides the primary trigger by coincidence.

Each plane consists of 14 modules. A module (Fig. 2.11a) contains a 10 mm thick, 110 mm wide, 720–1360 mm long scintillator paddle. Each paddle is connected on both ends to 3 photomultipliers (Hamamatsu R5900) via 50 mm long trapezoidal light guides (Fig. 2.11b). The paddles are wrapped with aluminized mylar and put into a two-shell, 0.6 mm thick, carbon fiber cover. The photomultipliers (PMs) are fixed with a plastic housing to the light guides. A 3 mm optical silicon rubber sheet is

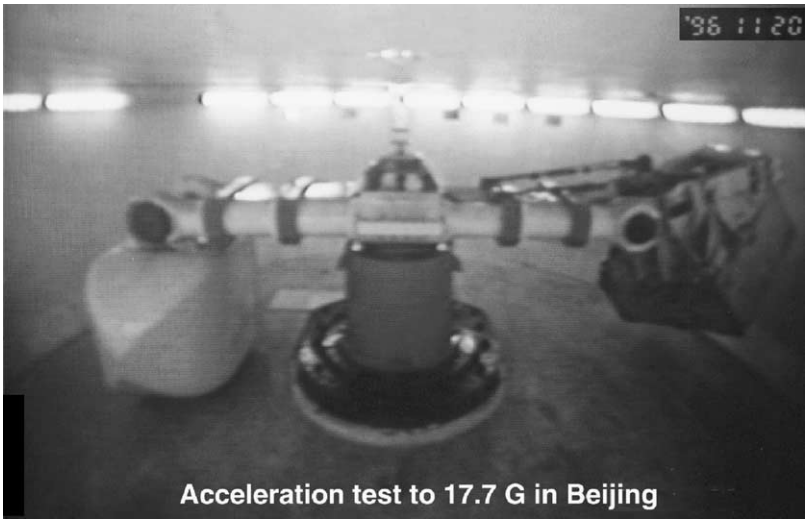

Fig. 2.6. AMS magnet undergoing static load centrifuge testing in Beijing.

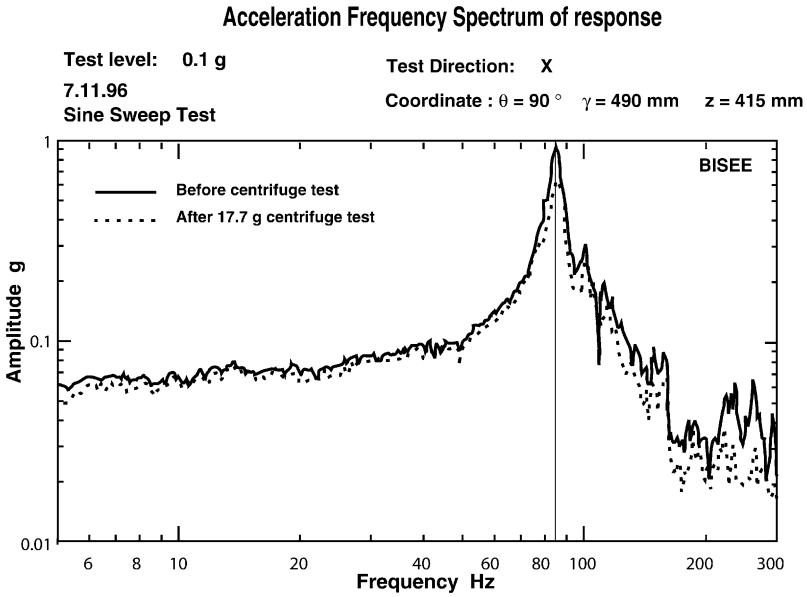

Fig. 2.7. Sine sweep test frequency spectrum response of AMS magnet before and after 17.7g centrifuge test.

put between the light guide and the PM photocathode window in order to mechanically decouple the PM from the paddle.

The signals from the three PMs on each side of the paddle are summed to provide one signal from the anodes and one from the 2nd to the last dynodes. The HV distribution resistor chain is mounted on two printed circuit boards (PCBs) behind each PM (Fig. 2.12). On the PCB attached to the central PM there are also a summing circuit and the output cables. As the PMs can only work

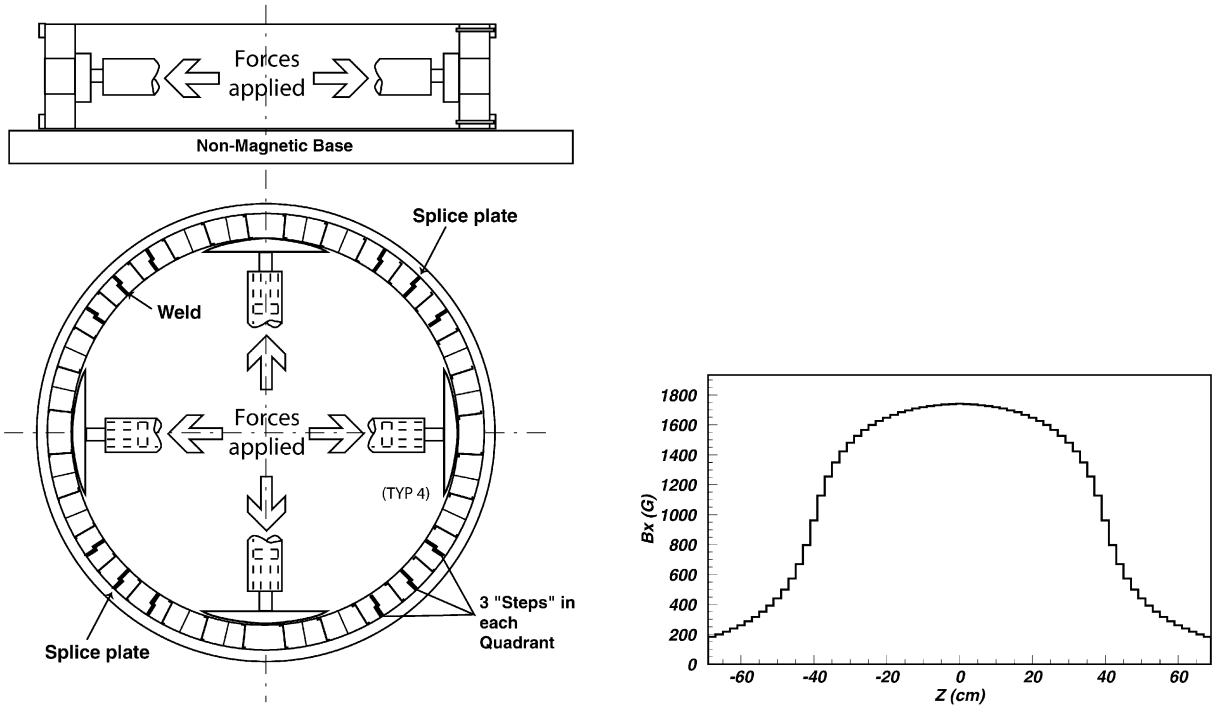

Fig. 2.8. Schematic of the third magnet to test to destruction.

Fig. 2.9. Main (bending) field component variation along the magnet longitudinal axis. $Z = 0$ corresponds to the magnet center. The magnet edges are at ± 40 cm.

in a weak magnetic field without performance degradation, the PMs and the electronic circuits are protected from the residual magnetic field, about 200 G, by a 0.5 mm thick shielding case made of permalloy. Two large PCBs mounted on top of each plane (see Fig. 2.10) contain two HV power supplies each. The power supplies produce and distribute the HV to the 42 PMs of each side of the plane. The same PCB holds the electronic circuits which allow the HV to be set individually for each PM. The operating pressure was expected to be higher initially than the ambient pressure of 10^{-12} bar due to outgassing, and the resulting electric surface conductivity is about 7 orders of magnitude larger than on the ground [8]. In order to avoid discharges, all PM sockets were potted with silicon rubber and the PCB surfaces were coated with a special varnish. For stiffness the modules are mounted onto a support made of a 100 mm thick aluminum honeycomb panel glued between two 5 mm thick aluminum skins. Carbon fiber brackets are used to fix the modules to the honeycomb panels. Each panel supports two scintillator planes.

Each read-out and trigger electronics module consists of a PCB mounted in an electronics crate mounted outside the magnet which processes signals from 4 channels. Each channel provides:

- A trigger signal (above a threshold of 150 mV) which is sent to the general trigger system.
- A high resolution (25 ps bin size) time measurement of the delay between the input anode signal (above a threshold of 30 mV) and the trigger signal arriving from the general trigger.

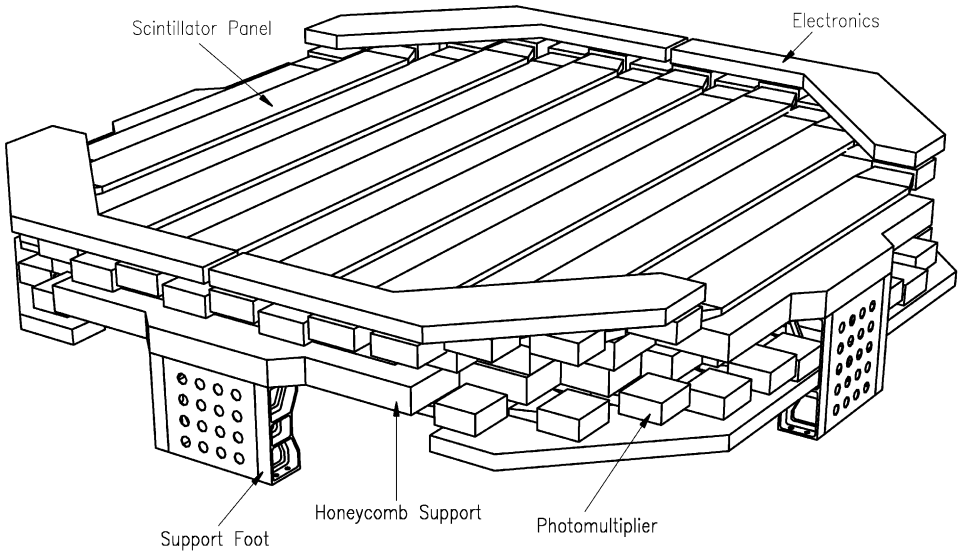

Fig. 2.10. Double plane hodoscope assembly (located on the top of the magnet), corresponding to S1 and S2 of Fig. 2.1.

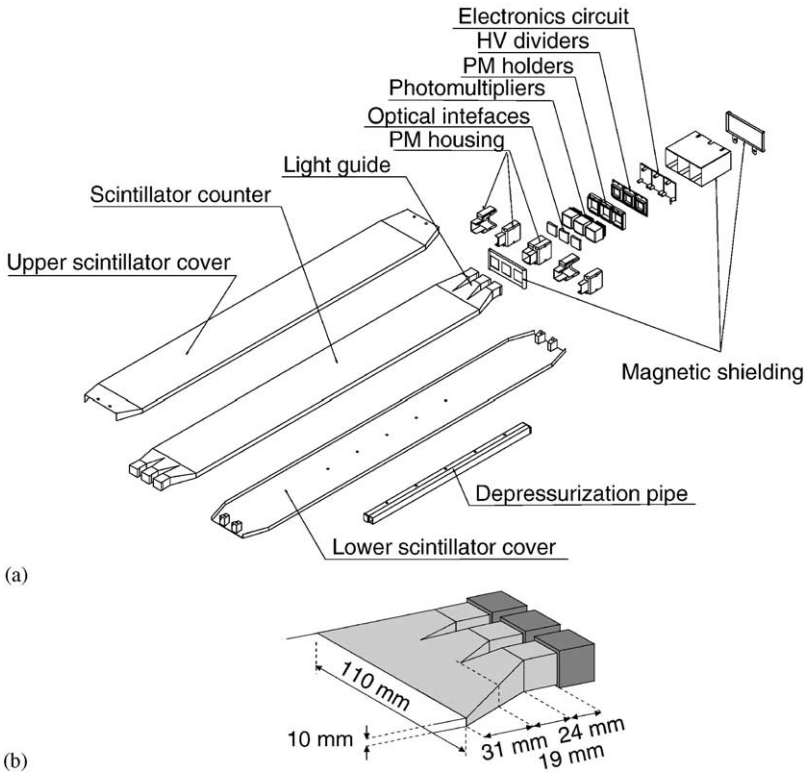

Fig. 2.11. (a) View of one scintillator module assembly; (b) design of the light guide.

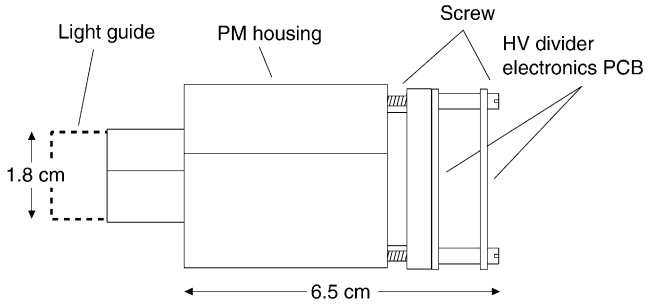

Fig. 2.12. Photomultiplier assembly.

- The integrated input anode signal.
- The integrated input dynode signal.
- A time-over-threshold signal which gives an estimate of the signal time (with 1 ns bin size) to tag off-time particles in a time interval of 10 μs before and 6.5 μs after the trigger.

The time and position of the particle in a paddle are derived from the high precision time measurements from the two sides of the counter. The anode dynamic range allowed the measurement of the particle charge up to $|Z| = 2$–3. The dynode signal extends the measurement range by a factor of about 5.

All elements passed a rigorous test and selection procedure before installation. The assembled modules were tested using cosmic rays. The average number of photoelectrons produced in the PMs by a minimum ionizing particle hitting the center of the counter was determined to be between 200 and 310 depending on the counter length. The following characteristics of the 56 modules were derived from the tests: Light attenuation length in paddles was ~ 2000 mm, effective velocity of light in the counter was 155 ± 1 mm/ns, time and position resolution were correspondingly 115–125 ps and 14.5–18.5 mm depending on the counter length.

The TOF system performance during the flight is illustrated by Fig. 2.13. The TOF resolution for helium ($Z = 2$) particles, as shown in Fig. 2.13, is typically 105 ps. The accuracy in the time of flight measurement obtained using the flight data is in agreement with the test measurements made before the flight. The performance of the TOF system proved to be stable throughout the shuttle mission. Fig. 2.14 shows the signal rate on one of the longest counters as a function of time for the 25 h period when the shuttle flew with the bay facing outer space. The variation of the rate with changing latitude is clearly visible, as well as the high rate periods when the detector passes through the South Atlantic Anomaly. The saturation limit of the readout electronics is about 20 kHz, in agreement with laboratory measurements.

2.3. The silicon tracker

Silicon detectors, commonly used as tracking devices in ground-based accelerator experiments, offer the best resolution in terms of position measurement. However, a large scale application of these devices in space has never been previously made. The AMS tracker consists of six planes of silicon sensors providing 10 μm (30 μm) position resolution in the bending (non-bending) plane of

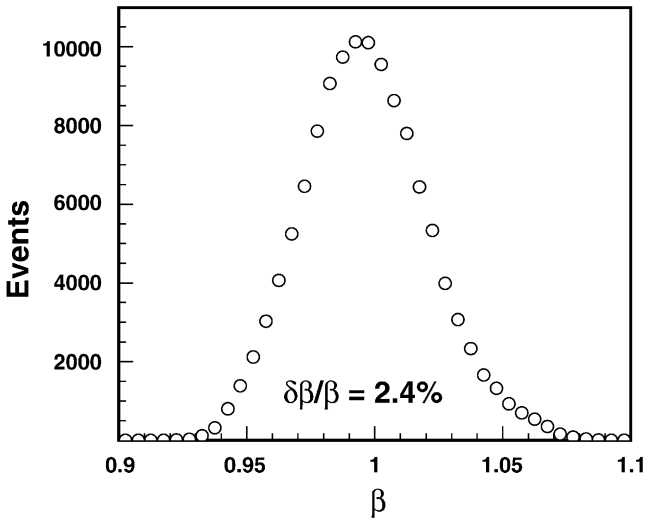

Fig. 2.13. Measured velocity, $\beta = v/c$, distribution for $|Z| = 2$ events with $R > 16$ GV.

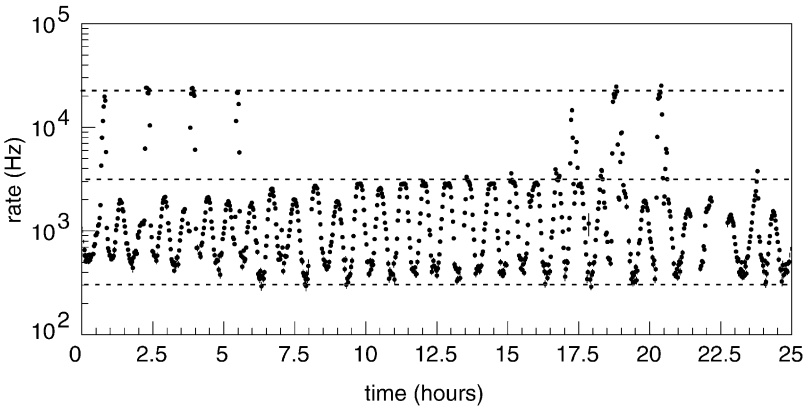

Fig. 2.14. Counting rate of a paddle as function of time during flight.

the 0.15 T field of the magnet. The silicon tracker measures both position and energy loss of particles. The energy loss measurements are combined with the energy loss and velocity measurements of the scintillators to determine the particle's charge. Once the charge is known, the momentum is determined by the coordinate measurements in the silicon, which are used to reconstruct the trajectory in the magnet field.

The silicon tracker is composed of double-sided microstrip sensors similar to those used for the ALEPH and L3 microvertex detectors at the Large Electron-Positron collider (LEP) at CERN [9,10]. The sensor design makes use of capacitive charge coupling [11] with implantation strip pitches of 27.5 μm for *p*-side and 26 μm for the *n*-side, where the *p*-side measures the coordinate in the bending plane and the *n*-side in the non-bending plane. The corresponding readout pitches were 110 and 208 μm.

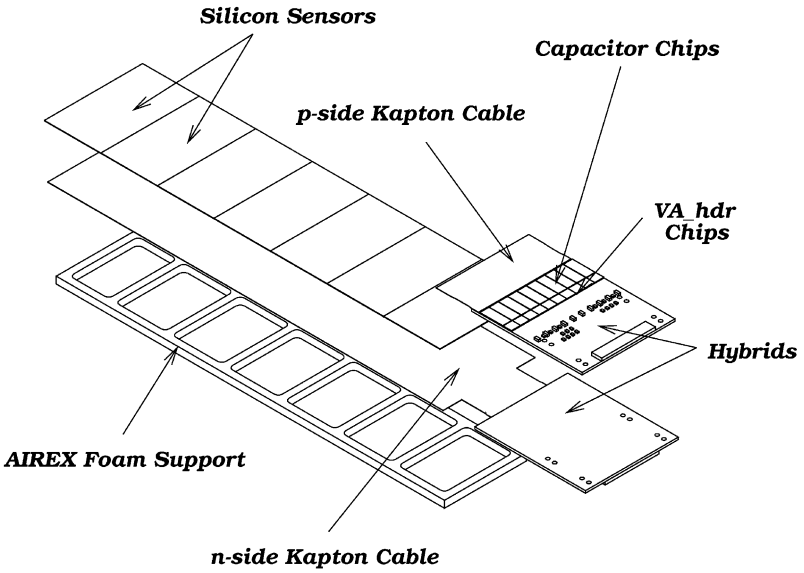

Fig. 2.15. View of a silicon tracker ladder.

A detailed description of the AMS tracker construction and performance is given in [12]. The silicon sensors are grouped together for readout and biasing in ladders of varying lengths to match the cylindrical geometry of the magnet, the maximum length of silicon for a single readout channel attaining 600 mm. The relatively large input capacitance, as well as the need for a high dynamic range, led to the development of a new front-end readout chip.

A metalized kapton foil, glued directly to the silicon sensors, serves as a routing cable to bring the *n*-side signals to the *n*-side front-end hybrid, which is located at the ladder end closest to the magnet wall. It is back to back with the *p*-side front-end hybrid which is connected to the strips by a short foil. Fig. 2.15 shows the principal elements of the ladder viewed from the *p*-side of the silicon sensors.

The average material thickness of an interior tracker plane, including ladders, represents 0.65% of a radiation length at normal incidence. Fig. 2.16 shows the assembled silicon tracker. The surrounding support structure is divided into three parts: a carbon fiber cylindrical shell which supports the interior planes 2–5, and two carbon fiber flanges which support the exterior planes 1 and 6. The hybrid pairs are mounted on carbon fiber-metal cooling bars which evacuate the heat generated by the front-end electronics to the exterior of the tracker volume. One to three meter long flat cables carry the analog and digital signals, as well as detector and bias voltages, between the hybrids and the Tracker Data Reduction (TDR) and power supply cards, which are located in crates mounted on the magnet support structure.

2.3.1. Performance during flight

After stabilization of the bias voltages, no significant change of the ladder dark current levels was observed when compared to the values measured during ground operation. The tracker calibration performed by the TDR determines the pedestals and pedestal widths for each channel, and the average

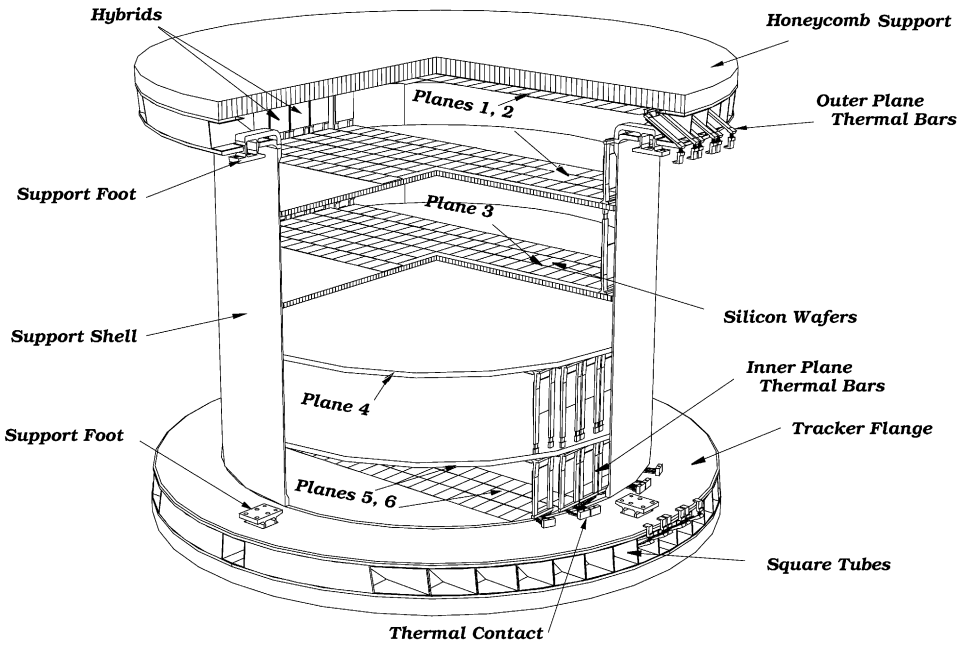

Fig. 2.16. The assembled AMS silicon tracker. Silicon ladders installed for the STS-91 flight are visible.

common noise widths of each chip. The ADC level of each channel is corrected by subtracting the common noise level, defined as the average ADC value recorded by the 64 channels of each chip. The first calibration results showed that the pedestals and pedestal widths of all channels during flight were very close to their pre-launch values.

Tracker calibrations were made automatically every 30 min during data taking. In addition, pedestal values were updated between calibrations using the event data. Abnormal interruptions of the data acquisition system, which required a reboot of the TDRs, triggered a new tracker calibration in order to reload the TDR buffers with valid calibration data for pedestal subtraction.

Fig. 2.17 shows the average pedestal widths for the p-side strips, and the temperature recorded at the AMS magnet, versus time. The tracker noise levels exactly follow the temperature variation related to solar exposure. The correlation between the two is linear over the observed range of temperatures with a slope of 0.025 ADC count/$^\circ$C. The silicon dark currents measured during the flight display an identical behavior.

During the whole flight the average common noise widths were stable within ± 0.5 ADC channels at the level of 7 and 10 ADC channels for p- and n-side chips respectively. In general, the common noise changes did not affect the overall tracker noise performance. The online cluster algorithm of the TDR used a threshold of $3\sigma_{\mathrm{ped}}$ to define cluster "seed" strips. Neighboring strips were included if their signals exceeded $1\sigma_{\mathrm{ped}}$.

The cluster signal-to-noise is defined as the total cluster charge divided by the root-mean-square of the pedestal widths of the member strips: $[\sum_i s_i]/[\sum_i \sigma_i^2]^{1/2}$, where s_i and σ_i are the strip signal and pedestal width. The cluster charges were normalized to correspond to the 300 μm path-length in the silicon and corrected to $\beta \geqslant 0.95$, i.e. for β smaller than 0.95 the cluster charge was multiplied

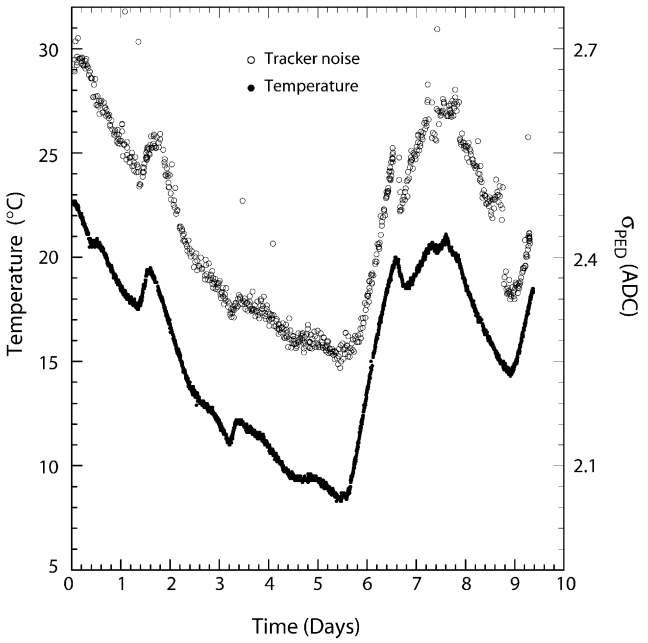

Fig. 2.17. Comparison of AMS temperature and tracker noise (σ_{PED} (ADC), the pedestal width) during the flight: temperature indicated on y-axis at left, p-side noise on y-axis at right.

Table 2.1
Threshold momentum for different particle species in the ATC

Particle	$e^{\pm}$	$\pi^{\pm}$	p, $\bar{p}$	He, $\overline{He}$
P_{thres}	1.91 MeV/c	0.52 GeV/c	3.51 GeV/c	14.0 GeV/c

by a factor $(\beta/0.95)^2$. The cluster signal-to-noise during the flight varied in a manner that reflects the noise behavior described above. The signal-to-noise ratio was stable throughout the whole period of tracker assembly, preflight tests and the flight at the level of about 7.5 : 1 and 4 : 1 for the p- and n-sides.

Because of the lower signal-to-noise performance on the n-side, the fraction of proton tracks with 4,5, and 6 planes which were reconstructed without n-side information is 50%, 58%, and 67% respectively. For the $|Z| > 2$ nuclei, the fraction of reconstructed tracks without n-side information is less than 10%.

The silicon tracker worked during flight as designed, unaffected by the launch and operation in space.

2.4. The Aerogel Threshold Čerenkov counter

The Aerogel Threshold Čerenkov counter (ATC) allows to extend the range of particle identification beyond the limit set by the time of flight measurement. Table 2.1 shows the thresholds for the

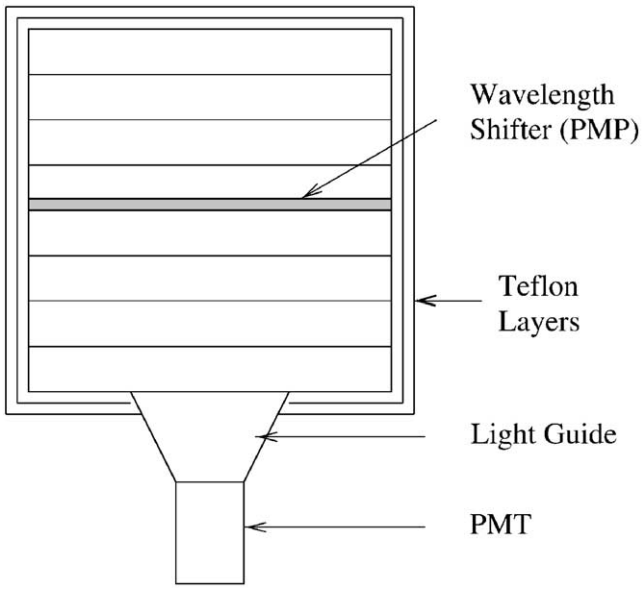

Fig. 2.18. An aerogel cell. The 8 blocks of aerogel are shown together with 3 enclosing teflon layers and the PMP wavelength shifter layer in the middle of the cell.

refraction index ($n = 1.035 \pm 0.001$) of the chosen radiator. The ATC detector [13] is constructed of $110 \times 110 \times 88\,\mathrm{mm}^3$ cells (see Fig. 2.18) filled with eight 11 mm thick aerogel blocks. Each cell is viewed by a photomultiplier. The emitted photons are internally reflected until they reach a PM by three 250 μm thick teflon layers surrounding the aerogel blocks. To reduce the Čerenkov photon losses connected with Rayleigh scattering and absorption (both decreasing with the increase of the photon wavelength, $L_R \propto \lambda_\gamma^4$, $L_{\mathrm{abs}} \propto \lambda_\gamma^2$) a wavelength shifter is placed in the middle of each cell (see Fig. 2.18). The shifter consists of a 25 μm layer of tedlar soaked in a PMP solution (1-phenyl-3-mesityl-2-pyrazolin). To avoid any contact between PMP and the aerogel, the shifter layer is put into a polyethylene envelope of 50 μm thickness. The shifter transforms the 300 nm Čerenkov photons into 420 nm photons. The wavelength of the shifted photons matches the maximum efficiency of the photomultiplier (Hamamatsu R-5900). The use of the shifter results in a $\sim 40\%$ increase in the number of photoelectrons. The 168 cells are grouped in modules enclosed in a carbon fiber structure. The modules are arranged in 2 rectangular layers. There are 8×10 cells in the upper and 8×11 cells in the lower layer. In order to minimize the signal loss for tracks passing between cells, the two layers are offset and fixed above and below a 50 mm thick honeycomb support plate. Two diagonally adjacent cells are coupled into one readout channel. The ATC uses the same readout electronics as the TOF counters, but optimized to accept the much lower input signals of just several photoelectrons. The ATC performance test and calibration was done using charged particles from a test beam at CERN and cosmic ray particles collected prior to and during the flight. The Čerenkov threshold is 0.37 ± 0.16 photoelectrons for all channels. The response to $\beta = 1$ particles (above the electronics threshold) is measured to be $n_{p.e} = 3.51 \pm 0.02$ for the upper plane and $n_{p.e} = 4.02 \pm 0.02$ for the lower plane.

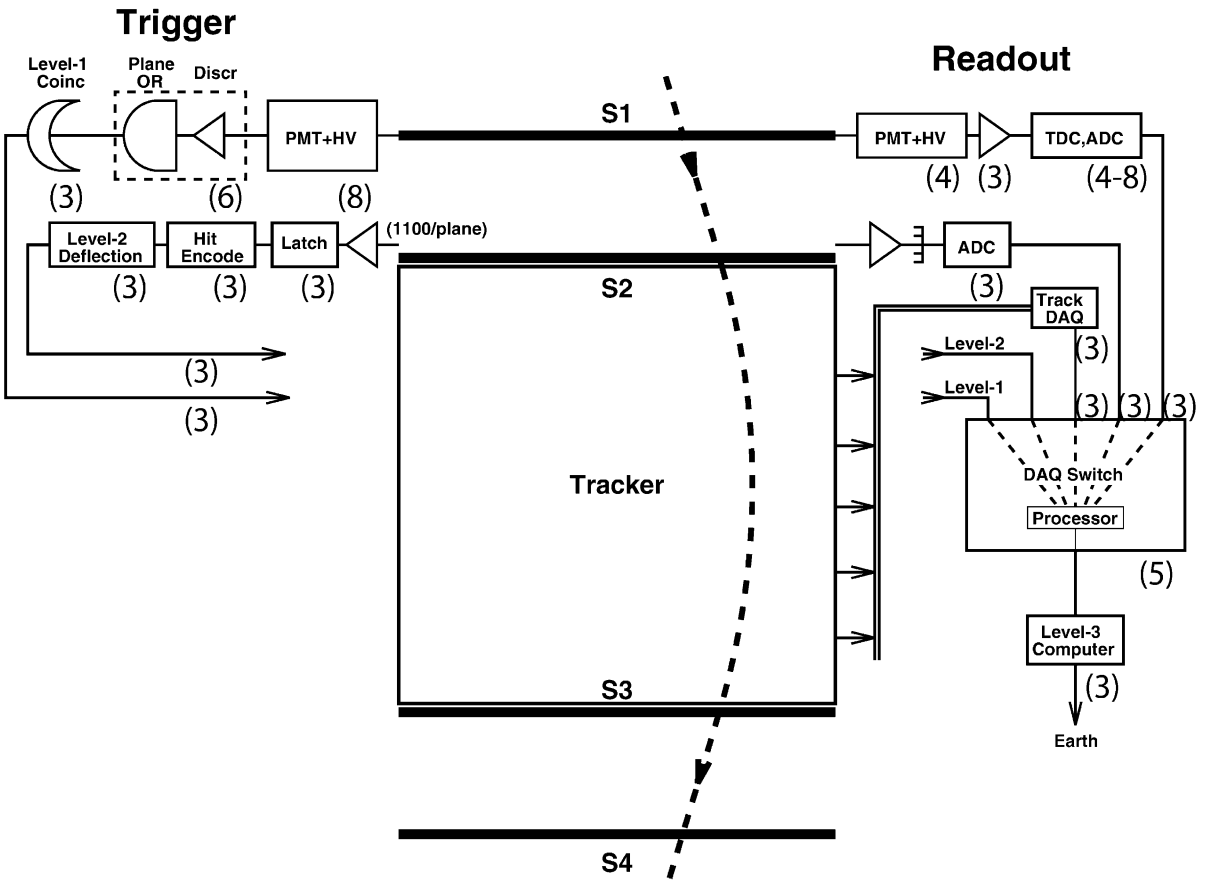

Fig. 2.19. AMS electronics. The numbers of redundant elements are given in parenthesis.

2.5. *Electronics, trigger and data taking*

AMS is a particle physics detector. Much care and attention are necessary to ensure the particle physics electronics can be applied in space. There are 70,000 channels of tracker signals which provide a coordinate accuracy of 10 μm. There are four layers of Time of Flight hodoscopes providing a time resolution of ∼100 ps. Both the Silicon Tracker and Time of Flight counters also provide independent dE/dx measurements to identify particle charge. Because of power and weight restrictions, all the electronics were specially designed, manufactured and space qualified by AMS institutions and aerospace industries in Europe and Asia. In particular the Chung-Shan Institute of Science and Technology in Lung-Tan, Taiwan made the most important contribution in the manufacturing of most of the AMS electronics.

Fig. 2.19 shows the principal AMS electronics design which is based on redundancy to safeguard against the loss of data in space. To space qualify the electronics, the system went through extensive

Table 2.2
Beam characteristics used for AMS radiation tests at Dubna

Beam	Energy (MeV)
Ne	270
Au	460
Kr	430

tests which included:

(a) vibration,
(b) temperature,
(c) thermal vacuum,
(d) radiation and
(e) electromagnetic compatibility.

The radiation tests were specially carried out at Dubna in August 1997 and these tests were particularly important to ensure there would be no single event latch up in space. Table 2.2 shows the beam and energy used in these tests.

Other space qualification tests (vibration, temperature,...) were carried out at the Max Plank Institute for Extraterrestrial Physics in Germany and at Chung-Shan Institute of Science and Technology in Taiwan.

The primary AMS trigger was a 4-fold coincidence of at least one counter in each hodoscope. Next, combinations of the paddles incompatible with the tracker geometry or triggers with signals in the veto counters were excluded. The overall acceptance with the trigger constraints was 0.42 m^2 sr. The trigger rate varied from about 100 up to 1600 Hz depending on the position of the detector with respect to the magnetic poles. The total readout dead time was ≈ 85 μs resulting in losses of $\sim$13% at the highest counting rates. In the South Atlantic Anomaly (SAA) region the rate precluded effective data taking.

The orbital inclination was 51.7° and the geodetic altitude ranged from 320 to 390 km. Data taking started on 3 June 1998 and the data was collected in three periods:

(a) 25 h before docking with the MIR space station, during which the shuttle attitude was constrained to keep the AMS longitudinal (z-axis) pointing within 45° of the zenith.
(b) Four days while docked to MIR. The AMS z-axis pointing varied between 40° and 145° of the zenith.
(c) After MIR undocking. Within a degree, the pointing was kept within 0°, 20° and 45° of the zenith for 19, 25 and 20 h. Before descending, the shuttle was turned over for approximately 9 h and the pointing was toward the nadir (180° pointing).

2.6. Detector calibration

The high precision momentum measurement provided by the silicon tracker as well as the good timing properties of the TOF system can only be realized through proper calibration. The

Table 2.3
Tracker composition

Layer #	Number of sensors	Number of ladders
1	120	8
2	141	12
3	108	9
4	120	10
5	138	12
6	90	6
Total	717	57

calibrations are mostly based on the flight data. The beam measurements are complementary and used to cross-check and rectify the calibrations obtained using the flight data. The beam tests with particles of fixed momenta are vital for the tracker alignment.

2.6.1. Tracker alignment

A track coordinate in a given tracker sensor can be measured to the accuracy of 10 (30) μm in the bending (non-bending) plane. To make use of this accuracy in the actual measurement of particle rigidity one has to know the absolute position in space of each sensor with adequate precision. The assembly technique provided better than 5 μm precision for the relative alignment of the sensors within the individual ladders. During the detector assembly a special measurement of the position of the tracker planes in the AMS coordinate system was performed. During the flight the tracker geometry was constantly monitored with the help of an incorporated laser system. Six laser beams were periodically passed through the tracker perpendicular to the silicon sensor planes. Signals of the laser spots on the planes were recorded.

The final tracker alignment was performed with the test beam data taken at the CERN proton synchrotron (PS). Measurements were performed in a monochromatic beam of positive particles of momenta in the range 2–14 GeV/c. In total 10^8 events were analysed.

In the alignment procedure a ladder was considered to be a rigid body and it was aligned relative to the other ladders by considering 6 degrees of freedom: 3 translations and 3 rotations. The procedure was to fit the measured coordinates to the trajectories of known high momentum particles, and then to minimize the summed χ^2 by varying the ladder positions and rotations. The fitting algorithm is based on the method of Ref. [14], modified for fixed momentum. The tracker composition is given in Table 2.3. There are many combinations of ladders each corresponding to different parameters (angles, momenta) of the trajectories. These different combinations have different sensitivity with respect to the ladder alignment parameters and have different angular acceptance. To simulate as many combinations as possible the detector was exposed to about 3000 different beam incident angles and positions. To align the tracker 3×10^7 14 GeV π^- events were used. Tight selection criteria on the coordinate measurements as well as on the resulting particle direction and momentum were applied to reject possible background or scattered events. Only 2–3% of the events passed this selection. Due to the large number ($57 \times 6 = 342$)

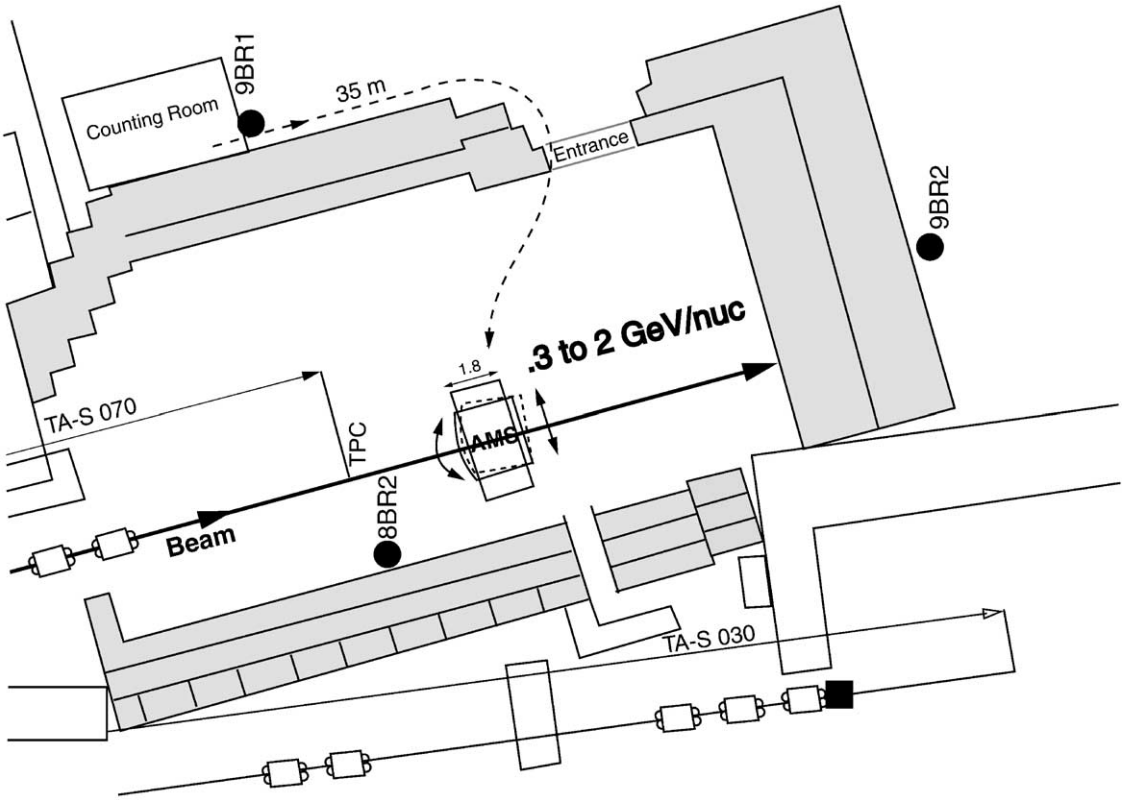

Fig. 2.20. Ion beam test layout. Data taken at 600 different angular detector positions.

of parameters to fit, it is important to find a good initial approximation of ladder coordinates and angles. This approximation was provided by the tracker metrology and its precision was better than 100 μm. The result of the procedure was that the residual misalignment achieved was below 10 μm.

2.6.2. Charge measurement calibration

The charge measurements obtained from the flight data were calibrated in the helium and carbon beams of GSI in Darmstadt. The layout of the GSI test is shown in Fig. 2.20. The detector was exposed to ion beams in the energy range 0.2–2 GeV/nucleus. To simulate the different angles of incidence of cosmic nuclei during the flight, the data were taken at 600 different angular detector positions. The GSI data also served to cross-check the parameters of the TOF system. Fig. 2.21 shows the GSI test beam composition and illustrates the accuracy of charge determination obtained from the scintillators. Fig. 2.22 shows the rigidity resolution of the He ions obtained after completion of the tracker alignment and charge measurement calibration.

Fig. 2.23 shows the calibrated energy loss measurement (flight data) used for the particle charge measurements.

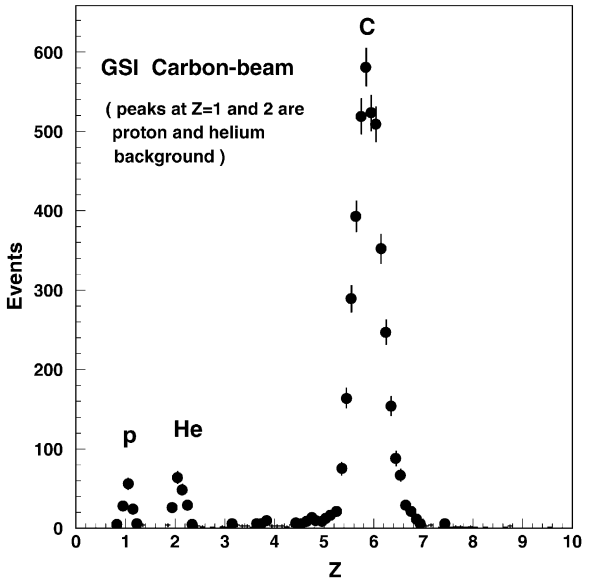

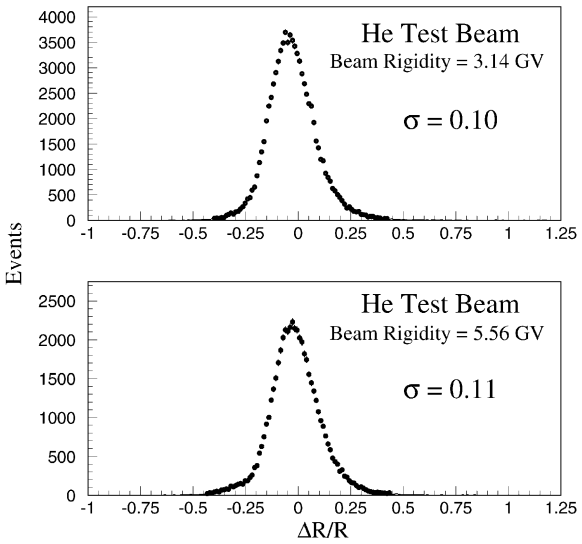

Fig. 2.21. Charge of beam particles determined in the scintillation hodoscopes.

Fig. 2.22. GSI helium test beam results. Rigidity resolution for 3.14 and 5.56 GV.

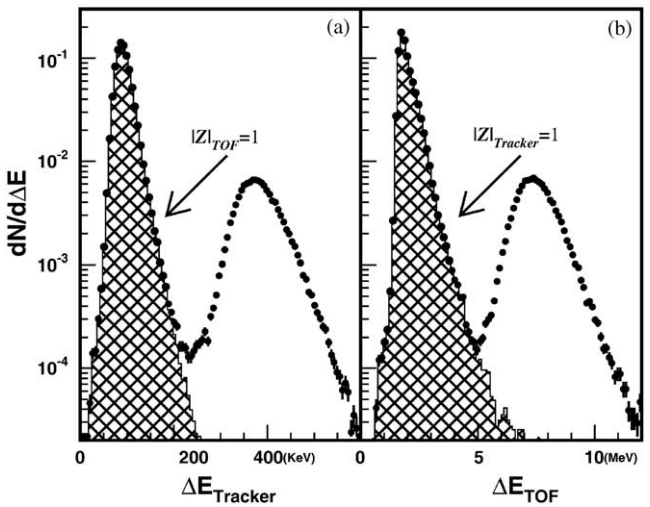

Fig. 2.23. Energy loss measurements (points) made independently with the tracker (a) and TOF (b) for $|Z| \leqslant 2$ events. The cross-hatched histograms show which events were assigned to be $|Z| = 1$ by the other detector.

3. Search for antihelium

Since one of the main objectives of the long duration AMS ISS flight is the search for antimatter, the precursor flight was to provide vital information about the real background conditions in space

and to ensure that the technique planned to be used by AMS is adequate. Therefore a search for antihelium nuclei using the data collected during this precursor flight was performed by AMS [15].

3.1. Data analysis

The procedure to search for antihelium began with event reconstruction, which included:

- Measurement of the particle rigidity, R, from the deflection of the trajectory measured by the tracker in the magnetic field. To ensure that the particle was well measured, hits in at least four tracker planes were required and the fitting was performed with two different algorithms, the results of which were required to agree.
- Measurement of the particle velocity, β, and direction, $\hat{z} = \pm 1$, from the TOF, where $\hat{z} = -1$ signifies a downward going particle in Fig. 2.1.
- Determination of the magnitude of the particle charge, $|Z|$, from the measurements of energy losses in the TOF counters and tracker planes (corrected for β).

From this reconstruction the sign of the particle charge was derived from the deflection in the rigidity fit and the direction. The particle mass was derived from the unsigned momentum, $|Z|Re/c$, and velocity, β.

The major backgrounds to the antihelium ($Z = -2$) search are the abundant amount of protons and electrons ($|Z| = 1$) and helium ($Z = +2$).

Key points in the selection for $\overline{\mathrm{He}}$ events and the rejection of background were:

To select events with $|Z| = 2$: This was to ensure no contamination from $|Z| = 1$ events with a wrongly measured charge magnitude which would mimic $|Z| > 1$ events. Fig. 2.23 shows the energy deposition and the assigned charge magnitude as measured independently by the TOF and the tracker. The probability of the wrong charge magnitude being assigned by the combined TOF and tracker measurements was estimated to be less than 10^{-7}.

To determine the sign of $|Z| = 2$ *events*: This was to distinguish He from $\overline{\mathrm{He}}$. This was done with the following method:

(i) *Identify the particle direction*: Measurement of the particle direction leads to the correct assignment of the sign of the charge. Fig. 3.1 shows the particle direction, $\hat{z}/\beta$, distribution. No events were observed between the $\hat{z} = +1$ and -1 populations which indicates there was no leakage of particles from one population to the other and the direction was always correctly assigned.

(ii) *Identify large angle nuclear scattering events*: Events in which a single nuclear scattering in one of the inner tracker planes, T2–T5, introduced a large angle kink in the track and might cause an incorrect measurement of the charge sign. This background was suppressed by a cut on the estimated rigidity error. Additional suppression was achieved by requiring agreement for the rigidity and charge sign measured using all the hits in the tracker and separately in the first three hits and the last three hits along the track. Fig. 3.2 shows the asymmetry, $A_{12} = (R_1 - R_2)/(R_1 + R_2)$, of the rigidity measured with the first and last three hits along the track, R_1 and R_2, and the cuts applied. From Fig. 3.2 we see that whereas these cuts reject much of the large angle scattering events (Fig. 3.2a), the cuts do not reject the genuine signal (Fig. 3.2b).

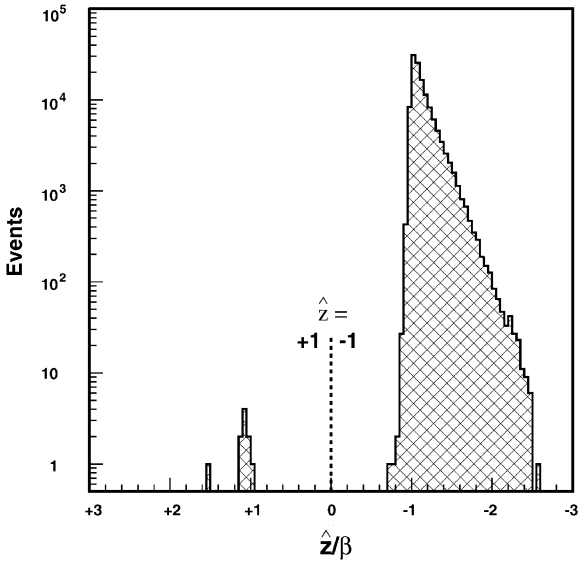

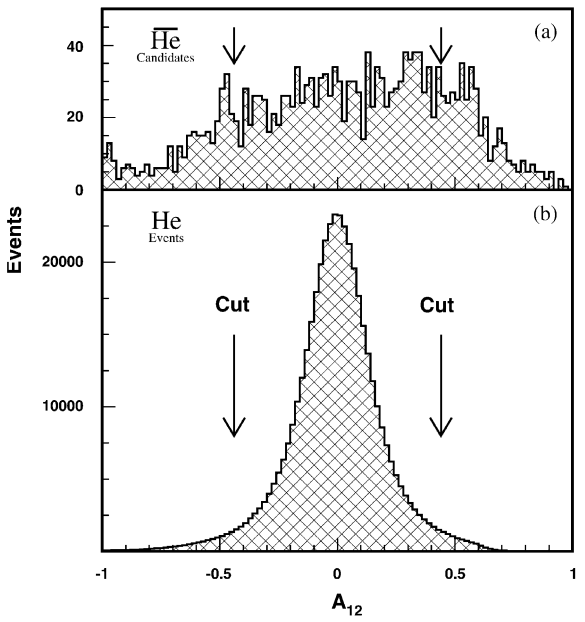

Fig. 3.1. A typical direction, $\hat{z}/\beta$, distribution for $|Z|=2$ events. As seen, the $\hat{z}=+1$ (or upward) and -1 (or downward) populations are clearly separated.

Fig. 3.2. The asymmetry, $A_{12}=(R_1-R_2)/(R_1+R_2)$, of the rigidity measurements using the first, R_1, and last, R_2, three hits along the track for $|Z|=2$ events. Also shown are the cuts used. As seen the A_{12} cuts reject much of the large angle scattering events (a). The cuts do not reject the genuine signal (b).

(iii) *Identify events with collinear delta rays*: Events with collinear debris, e.g. delta rays, from an interaction of the primary particle in the tracker material which may shift a measured point from the trajectory, leading to an incorrectly measured rigidity and charge sign. This background was efficiently rejected by an isolation cut which rejected events with an excess of energy observed within 5 mm of the track.

A probabilistic function was then constructed from measurements of the velocity, rigidity and energy loss which described the compatibility of these measurements with the passage of a helium or antihelium nucleus of mass $A=3$ or 4. Fig. 3.3 shows the compatibility distribution for the antihelium candidates (Fig. 3.3a) and helium samples together with Monte Carlo predictions for the helium event distribution (Fig. 3.3b). As seen, the compatibility cut enables us to reject the small remaining background and keep nearly all of the helium sample.

The results of our search are summarized in Fig. 3.4. We obtain a total of 2.86×10^6 He events up to a rigidity of 140 GV. We found no antihelium event at any rigidity.

3.2. Results and interpretation

Since no antihelium nuclei were observed, we can only establish an upper limit on their flux. Here three upper limits on this flux relative to the observed flux of helium nuclei are calculated which differ in the assumptions used for the antihelium rigidity spectrum. In the first it is assumed

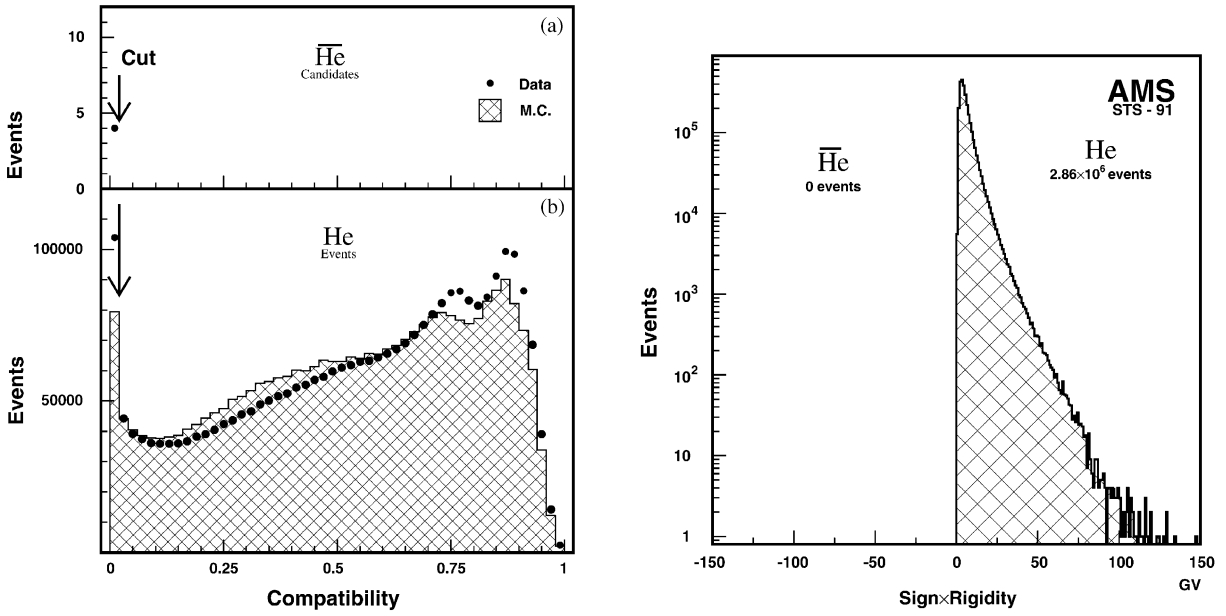

Fig. 3.3. (a) Compatibility of the measured event parameters, β, R and $|Z|$, to be an $\overline{\text{He}}$ nucleus. (b) Compatibility to be a He nucleus. The hatched histogram is the Monte Carlo prediction for He nuclei.

Fig. 3.4. Measured rigidity times the charge sign for selected $|Z| = 2$ events.

to have the same shape as the helium rigidity spectrum. In the second this spectrum is assumed to be uniform. Finally a conservative estimate is made independent of the antihelium rigidity spectrum.

All of these methods require the measured rigidity spectrum to be corrected for the detector resolution and efficiency as a function of the measured, R_m, and incident, R, rigidity. The detection efficiency including the rigidity resolution function, $f(R, R_m)$, was evaluated through complete Monte Carlo simulation using the GEANT Monte Carlo package [16]. The incident rigidity spectrum, $\mathrm{d}N'/\mathrm{d}R$ was extracted from the measured spectrum, $\mathrm{d}N'/\mathrm{d}R_m$, by numerical deconvolution of $\mathrm{d}N'/\mathrm{d}R_m = \int(\mathrm{d}N'/\mathrm{d}R) \times f(R, R_m)\,\mathrm{d}R$. To obtain the detector efficiency for antihelium, $\varepsilon_{\overline{\text{He}}}(R)$, a small correction was applied to the efficiency for helium nuclei, $\varepsilon_{\text{He}}(R)$, based on the estimated [17] difference in absorption cross sections.

Letting $N_{\text{He}}(R_i)$ be the number of incident helium nuclei in the rigidity bin $(R_i, R_i + \Delta R)$ and $N'_{\text{He}}(R_i)$ be the number of measured He in the same rigidity bin after correction for the detector resolution, then $N'_{\text{He}}(R_i) = \varepsilon_{\text{He}}(R_i) N_{\text{He}}(R_i)$, where $\varepsilon_{\text{He}}(R_i)$ is the detection efficiency in this bin, and similarly for antihelium. Over the rigidity interval studied no $\overline{\text{He}}$ were found, $N'_{\overline{\text{He}}}(R_i) = 0$ for each i. At the 95% confidence level this is taken to be less than 3 and the differential upper limit for the flux ratio is given by

$$\frac{N_{\overline{\text{He}}}(R_i)}{N_{\text{He}}(R_i)} < \frac{3/\varepsilon_{\overline{\text{He}}}(R_i)}{N'_{\text{He}}(R_i)/\varepsilon_{\text{He}}(R_i)}\ . \tag{3.1}$$

The difference between $\varepsilon_{\overline{\text{He}}}(R_i)$ and $\varepsilon_{\text{He}}(R_i)$ is small, so these terms practically cancel and the results below are essentially independent of the detection efficiency.

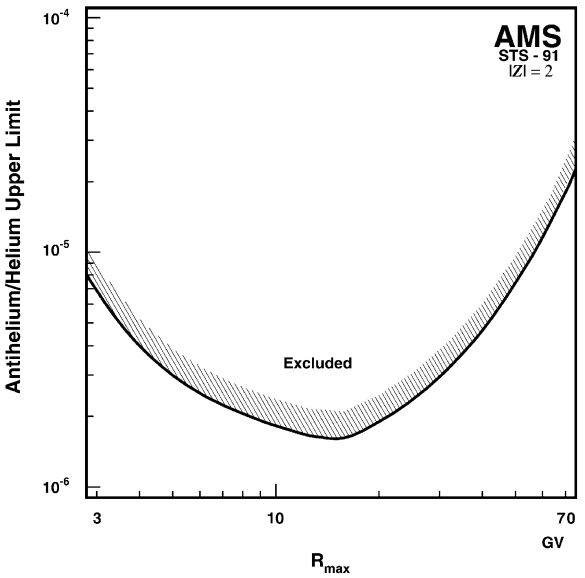

Fig. 3.5. Upper limits on the relative flux of antihelium to helium, at the 95% confidence level, as a function of the rigidity interval $R = 1.6$ GV to $R_{\max}$. These results are independent of the incident antihelium spectra.

(i) If the incident $\overline{\mathrm{He}}$ spectrum is assumed to have the same shape as the He spectrum over the range $1 < R < 140$ GV, then summing Eq. (3.1) yields a limit of:

$$\frac{N_{\overline{\mathrm{He}}}}{N_{\mathrm{He}}} < 1.1 \times 10^{-6} .$$

(ii) Assuming a uniform $\overline{\mathrm{He}}$ rigidity spectrum, and using a mean $\overline{\mathrm{He}}$ inverse detection efficiency, $\langle 1/\varepsilon_{\overline{\mathrm{He}}} \rangle = \sum (1/\varepsilon_{\overline{\mathrm{He}}}(R_i))/n$, and noting that $N'_{\overline{\mathrm{He}}} = \sum N'_{\overline{\mathrm{He}}}(R_i) = 0$ which is also taken to be less than 3 at the 95% C.L., summing Eq. (3.1) yields a limit of

$$\frac{N_{\overline{\mathrm{He}}}}{N_{\mathrm{He}}} = \frac{\sum N_{\overline{\mathrm{He}}}(R_i)}{\sum N_{\mathrm{He}}(R_i)} < \frac{3\langle 1/\varepsilon_{\overline{\mathrm{He}}} \rangle}{\sum N'_{\mathrm{He}}(R_i)/\varepsilon_{\mathrm{He}}(R_i)} , \tag{3.2}$$

$$\text{which evaluates to } \frac{N_{\overline{\mathrm{He}}}}{N_{\mathrm{He}}} < 1.8 \times 10^{-6} \text{ for } R = 1.6\text{–}40 \text{ GV}$$

$$\text{and } \frac{N_{\overline{\mathrm{He}}}}{N_{\mathrm{He}}} < 3.9 \times 10^{-6} \text{ for } R = 1.6\text{–}100 \text{ GV} .$$

(iii) For a conservative upper limit, which does not depend on the antihelium spectrum, Eq. (3.1) is summed from $R_{\min} = 1.6$ GV up to a variable $R_{\max}$ and instead of the mean value $\langle 1/\varepsilon_{\overline{\mathrm{He}}} \rangle$ the minimum value of this efficiency in the $(R_{\min}, R_{\max})$ interval is taken, yielding

$$\frac{\sum N_{\overline{\mathrm{He}}}(R_i)}{\sum N_{\mathrm{He}}(R_i)} < \frac{3/\varepsilon^{\min}_{\overline{\mathrm{He}}}(R_{\min}, R_{\max})}{\sum N'_{\mathrm{He}}(R_i)/\varepsilon_{\mathrm{He}}(R_i)}, \text{ where } R_i = (R_{\min}, R_{\max}) . \tag{3.3}$$

These results are shown in Fig. 3.5 as a function of $R_{\max}$.

In conclusion, we found no antihelium nuclei at any rigidity. Up to rigidities of 140 GV, 2.86×10^6 helium nuclei were measured. Assuming the antihelium rigidity spectrum to have the same shape as the helium spectrum, an upper limit at the 95% confidence level on the relative flux of antihelium to helium of 1.1×10^{-6} was obtained. This result is an improvement in both sensitivity and rigidity range over previous measurements [3]. This flight has shown that the completed AMS on the International Space Station will provide many orders of magnitude of improvement in the sensitivity to search for antihelium.

4. Cosmic ray spectrum measurements

4.1. Introduction

The study of cosmic ray charge particle spectra improves the understanding of the interstellar propagation and acceleration of cosmic rays. Recently, accurate knowledge of the cosmic ray spectra has become important to reliably evaluate the atmospheric neutrino spectrum in view of the studies of neutrino oscillation phenomenon.

There are three distinct regions in space where charge particles have been studied by different means:

- The altitudes of 30–40 km above the Earth's surface. This region has been studied with balloon mounted detectors for several decades. Balloon experiments have made important contributions to the understanding of the primary cosmic ray spectrum of charged particles and the behavior of atmospheric secondary particles in the upper layer of the atmosphere.
- The inner and outer radiation belts, which extend from altitudes of about 1000 km up to the boundary of the magnetosphere. Small size detectors on satellites have been sufficient to study the high intensities in the radiation belts.
- A region intermediate between the top of the atmosphere and the inner radiation belt. The radiation levels are normally not very high, so satellite-based detectors used so far, i.e. before AMS, have not been sensitive enough to systematically study the spectrum in this region over a broad energy range. The exception is a small area known as the South Atlantic Anomaly where, due to a strong distortion of the Earth's magnetic field, the inner belt extends downwards causing anomalously high proton rates.

Refs. [18–24] include some of the previous studies. A few pioneering satellite experiments [25] have reported data on low energy electrons and positrons. The primary feature in the charge particle spectrum observed near Earth is a low energy drop off in the flux, known as the geomagnetic cutoff. This cutoff occurs at kinetic energies ranging from $\sim$ 10 MeV to $\sim$ 10 GeV depending on the latitude and longitude.

Above cutoff, $\gtrsim$10 GeV, numerous measurements indicate the spectrum falls off according to a power law.

Helium nuclei are the second most abundant element in cosmic rays. Helium rigidity spectrum measurements carried out over the past several decades (see [24] and references therein) have yielded insight into the origin of cosmic rays [26]. Since no difference in the rigidity spectra of protons

and helium has been detected the same sources and propagation histories were inferred for both species [27]. However recent and more accurate measurements [21,28] suggest protons and helium may have different spectral indices in the range 10–100 GeV. The most accurate experiments to date were balloon based [21–23], however even $\sim 5 g/\mathrm{cm}^2$ of residual atmosphere was an important source of systematic errors. Above $\sim$1000 GeV emulsion experiments [29,30] have indicated a more pronounced difference.

Accurate measurements of primary cosmic ray spectra, particularly of protons, are important for atmospheric neutrino studies and studies of neutrino oscillation phenomena [31].

The high energy lepton ($e^{\pm}$) spectra in cosmic rays are dominated by an electron component. High energy electrons are believed to originate from primary acceleration sites, specifically from supernova explosions. High energy electron–positron pairs are thought to be produced from the collisions of cosmic ray hadrons and gamma rays with interstellar gas, and the expected positron to electron ratio in cosmic rays arriving at Earth is roughly 10% and it decreases with energy. This picture is based on the experimental data collected over 35 years [19,32–34] by balloon experiments as well as phenomenological model descriptions developed over the same period [20,35,36].

In this report we present the data collected during the flight to study the cosmic ray proton spectrum from kinetic energies of 0.1–200 GeV [37,38], the helium spectrum over the kinetic energy range 0.1–100 GeV/nucleon [39] and the spectra of electrons and positrons over the respective kinetic energy ranges of 0.2–30 GeV and 0.2–3 GeV [40], the latter range being limited by the proton background. Antiproton and deuteron spectra were measured from 0.2 to 4 GeV and from 0.09 to 0.85 GeV/nucleon. Data taken while orbiting in or near the South Atlantic Anomaly were excluded.

The high statistics, $\sim 10^7$ protons and $\sim 10^5$ electrons, available allow the variation of the spectrum with position to be measured both above and below the geomagnetic cutoff. Because the incident particle direction and momentum were accurately measured in AMS, it is possible to investigate the origin of charged particles below cutoff by tracking them in the Earth's magnetic field.

4.2. Analysis

The response of the detector was simulated using the AMS detector simulation program, based on the GEANT package [16,41]. The effects of energy loss, multiple scattering, interactions, decays and the measured detector efficiency and resolution were included.

4.2.1. Event reconstruction and selection

Reconstruction of the incident particle type, energy and direction started with a track finding procedure which included cluster finding, cluster coordinate transformation and pattern recognition. The track was then fit using two independent algorithms [14,42]. For a track to be accepted the fit was required to include at least 4 hits in the bending plane and at least 3 hits in the non-bending plane.

The track was then extrapolated to each time of flight plane and matched with the nearest hit if it was within 60 mm. Matched hits were required in at least three of the four time of flight planes. The velocity, $\beta = v/c$, was then obtained using this time of flight information and the trajectory. For events which passed through the Čerenkov counter sensitive volume an independent velocity measurement, β_C, was also determined. To obtain the magnitude of the particle charge, $|Z|$, a set

of reference distributions of energy losses in both the time of flight and the tracker layers were derived from calibration measurements made at the CERN test beam interpolated via the Monte Carlo method. For each event these references were fit to the measured energy losses using a maximum likelihood method. The track parameters were then refit with the measured β and Z and the particle type determined from the resultant Z, β, β_C and rigidity, $R = pc/|Z|e$ (GV). Electron candidates were specifically selected by requiring the measured particle charge to be -1 and the particle velocity to be compatible with the speed of light. Positron candidates were selected by requiring the charge to be $+1$ and, as for electrons, the velocity be compatible with the speed of light and track quality cuts.

4.2.2. Background determination

As protons and helium nuclei are the dominant components in cosmic rays, after selecting events with $Z = +1$ the proton sample has only minor backgrounds which consist of charged pions and deuterons. The estimated fraction of charged pions, which are produced in the top part of AMS, with energy below 0.5 GeV is 1%. Above this energy the fraction decreases rapidly with increasing energy. The deuteron abundance in cosmic rays above the geomagnetic cutoff is about 2%. To remove low energy charged pions and deuterons the measured mass was required to be within 3 standard deviations of the proton mass. This rejected about 3% of the events while reducing the background contamination to negligible levels over all energies.

The main potential source of background to the helium sample were protons wrongly reconstructed as $|Z| = 2$ particles. Using the independent measurement of the charge magnitude obtained from the time of flight counters, this background was estimated to be less than 10^{-4} over all energies.

Backgrounds in the electron sample arose from protons with wrongly measured momentum and from secondary pions produced in the detector materials. The two most important cuts used to remove these backgrounds were on the χ^2 value obtained in fitting the particle trajectory, which removed tracks with large single or multiple scattering, and on the number of hits near the reconstructed trajectory in both the tracker and time of flight scintillators. After the above cuts were applied, the overall probability of a proton event to be accepted as an electron, estimated from Monte Carlo simulations and confirmed in the CERN test beam, was $O(10^{-4})$ with an electron selection efficiency of 75%. To further reduce the pion background only events whose track passed through the active Čerenkov counter area and, therefore, had an independent velocity measurement were accepted.

In contrast to electrons, the main background for the positron sample came from proton events with poorly measured velocity. The rejection power against this background decreased rapidly with increasing proton momentum, therefore tighter quality cuts on the velocity measurements were applied. Above 1 GeV/c protons were rejected by requiring two independent velocity measurements from the two separate Čerenkov counter layers to be compatible with the velocity of a positron. Lower energy protons were rejected by requiring the energy loss measurements in four layers of time of flight counters and six double layers of silicon tracker to be compatible with a positron. These cuts yielded an additional background rejection factor of 5 at the expense of lower positron selection efficiency. A convolution of the background rejection function with the measured proton spectra provided an energy dependent background estimation. Fig. 4.1 shows the measured electron and positron spectra together with the estimated background for the geomagnetic polar regions, where the background conditions were most severe.

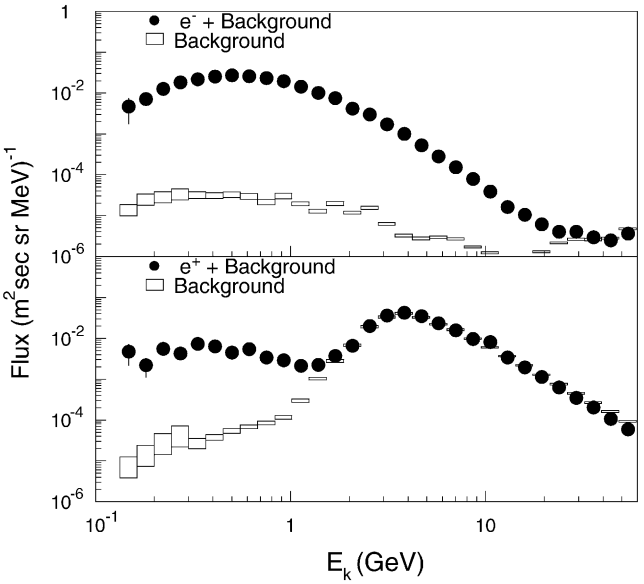

Fig. 4.1. The primary $e^{\pm}$ fluxes and background in the geomagnetic polar region ($|\Theta_M| > 0.9$).

4.2.3. *Differential fluxes*

To determine the differential fluxes from the measured counting rates requires the acceptance to be known as a function of the incident momentum and direction. Particles with different momenta and directions were generated via the Monte Carlo method, passed through the AMS detector simulation program and accepted if the trigger and reconstruction requirements were satisfied as for the data. The acceptance for protons was found to be 0.15 m^2 sr on average, varying from 0.3 to 0.03 m^2 sr with incident angle and location and only weakly momentum dependent. These acceptances were then corrected following an analysis of unbiased trigger events. The corrections to the central value are shown in Table 4.1 together with their contribution to the total systematic error of 5%.

The average electron acceptance was found to rise from about 0.01 m^2 sr at 0.15 GeV and level off at 0.1 m^2 sr above 0.7 GeV. Table 4.2 summarizes the estimated electron and positron efficiencies.

The differential helium flux was determined by correcting the measured rates for the detector acceptance as a function of the momentum and the direction of the particles. The acceptance function was determined via the Monte Carlo method using simulated helium event samples which were required to pass through a trigger simulation and the above reconstruction and selection chain as for data. The average acceptance was determined to be 0.10 m^2 sr for rigidities above 20 GV, increasing at lower energies up to 0.16 m^2 sr. Corrections to the acceptance were studied with a sample of events collected with an unbiased trigger and by comparing data and Monte Carlo samples. The average contributions to the uncertainty in these corrections were 4% from the trigger, 3% from the track reconstruction, and 2% each from the modeling of particle interactions and from the selection leading to an overall systematic error of 6%.

To obtain the incident differential spectrum from the measured spectrum, the effect of the detector resolution was unfolded using resolution functions obtained from the simulation. These functions were checked at several energy points by test beam measurements. The data were unfolded using

Table 4.1
Proton acceptance corrections and their systematic uncertainties, in percent

Correction	Amount	Uncertainty
Trigger		
4-Fold coincidence	−3	1.5
Time of flight pattern	−4	2
Tracker hits	−2	1
Anticoincidence	0	1
Analysis		
Track and velocity fit	−2	1.5
Particle interactions	+1	1.5
Proton selection	−2	2
Monte Carlo statistics	0	2
Differential acceptance binning	0	2
Total	−12	5

Table 4.2
Percentage $e^{\pm}$ selection efficiencies and uncertainties

Cut	Efficiency (%)
Tracking quality cuts	75 ± 3
Common $e^{\pm}$ velocity cuts	52 ± 1
Additional e^{+} velocity cuts	72 ± 1.5
Total electrons	39 ± 1.7
Total positrons	28 ± 1.3

a method based on Bayes' theorem [43–45], which used an iterative procedure (and not a "regularized unfolding") to overcome instability of the matrix inversion due to negative terms. As an example, Fig. 4.2 compares the proton differential proton spectrum before and after unfolding in the geomagnetic equatorial region.

The observed primary proton spectrum was verified to be isotropic as seen in Fig. 4.3a where the spectra in kinetic energy, E_K, scaled by $E_K^{2.75}$ are compared for two intervals of incident angle to the detector, θ, and in Fig. 4.3b, where the average fluxes are shown as functions of the incident angle. In the measured angular range, both are in agreement with an isotropic distribution. Therefore the three data collection periods, corresponding to 0°, 20° and 45° shuttle attitude, are combined to obtain a data set having a total of 5.6 million primary protons.

Given the resulting small statistical errors, further detailed studies of the systematic effects were performed.

The first source of systematic error, ε_{sys1}, was due to trigger efficiency variations and event reconstruction accuracy variations, both of which are related to the background rates and detector temperatures at different times and at different shuttle locations and orientations and to the energy deposited by the proton in each detector layer. Above $\sim$20 GeV this systematic error is nearly

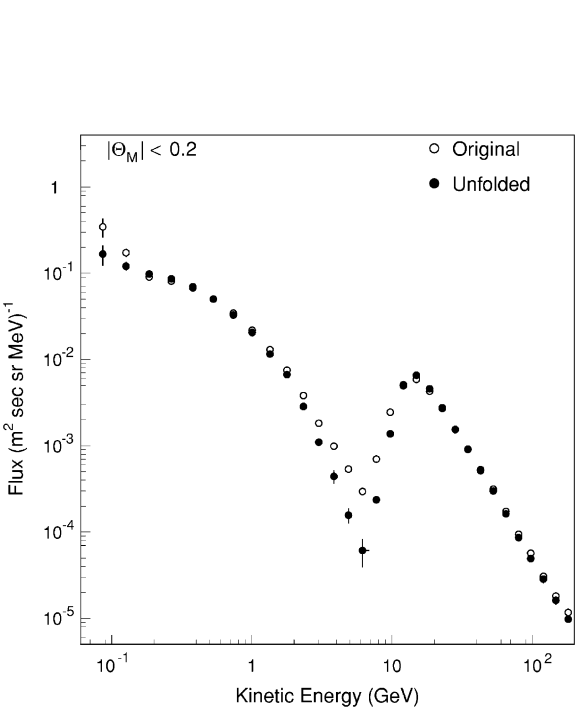

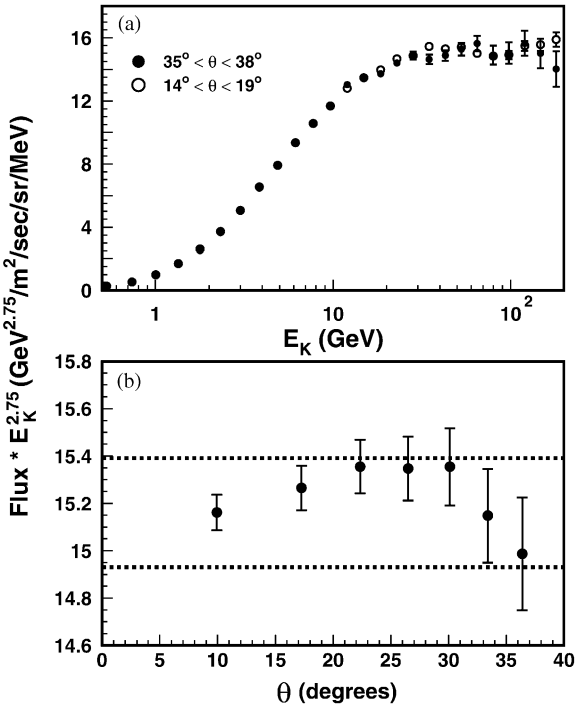

Fig. 4.2. The proton differential flux in the equatorial region. Open circles show the measured distribution, filled circles are the data after unfolding.

Fig. 4.3. Isotropy: (a) comparison of the energy spectra for two angular acceptance ranges. (b) Fluxes averaged above 20 GeV as a function of the incident particle angle. Error bars show statistical errors. The dashed lines in (b) indicate the estimated range of systematic errors for this case. As seen, the data are independent of θ.

Table 4.3
Average systematics of the trigger and reconstruction, ε_{sys1}

Source	Error (%)
Fast trigger	1.5
Anti trigger	1
Level3 TOF	2
Level3 tracker	1.5
Track and velocity fit	1.5
Total	3.5

energy independent. The calculated average contributions are shown in Table 4.3, the total error from this origin is 3.5%.

A second source of systematic effects, ε_{sys2}, arose from Monte Carlo corrections. These errors are energy dependent but uncorrelated between energy bins. The calculated average contributions are

Table 4.4
Systematics of the Monte Carlo corrections leading to the energy dependent ε_{sys2}

Source	Error (%)
Particle interactions	1.5
Monte Carlo statistics	1.5
Proton selection	2
Geomagnetic cutoff	0.5
Total	3.0

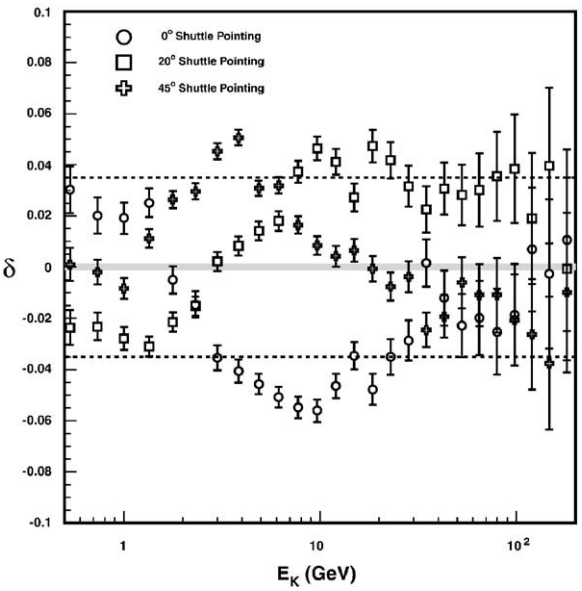

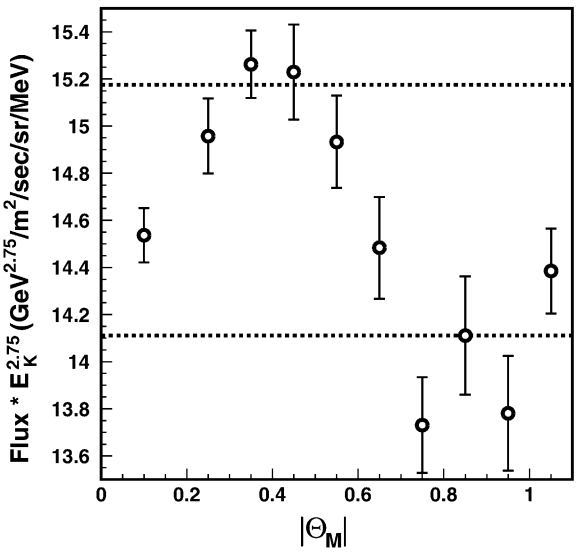

Fig. 4.4. Systematic error verification: flux variation, δ, as a function of proton energy for different shuttle orientations. Errors shown are statistical. The dashed lines show the range of systematic error calculated for this case.

Fig. 4.5. Systematic error verification: fluxes averaged above 20 GeV scaled by $E_K^{2.75}$ as a function of magnetic latitude. Errors shown are statistical. The dashed lines show the range of the systematic error calculated for this case.

shown in Table 4.4 and total to 3%. The contributions of ε_{sys1} and ε_{sys2} versus energy are detailed in Table 4.8.

A third source of systematics, ε_{sys3}, is from the unfolding used to obtain the incident differential spectrum from the measured spectrum based on resolution functions obtained by simulation. These errors are bin to bin correlated. As detailed in Table 4.8, they are typically 1% below $\sim$20 GeV and reach 5% at $\sim$100 GeV.

A careful experimental verification of the calculated systematic errors was performed. The calculated error took into account the propagation of the statistical and three systematic errors.

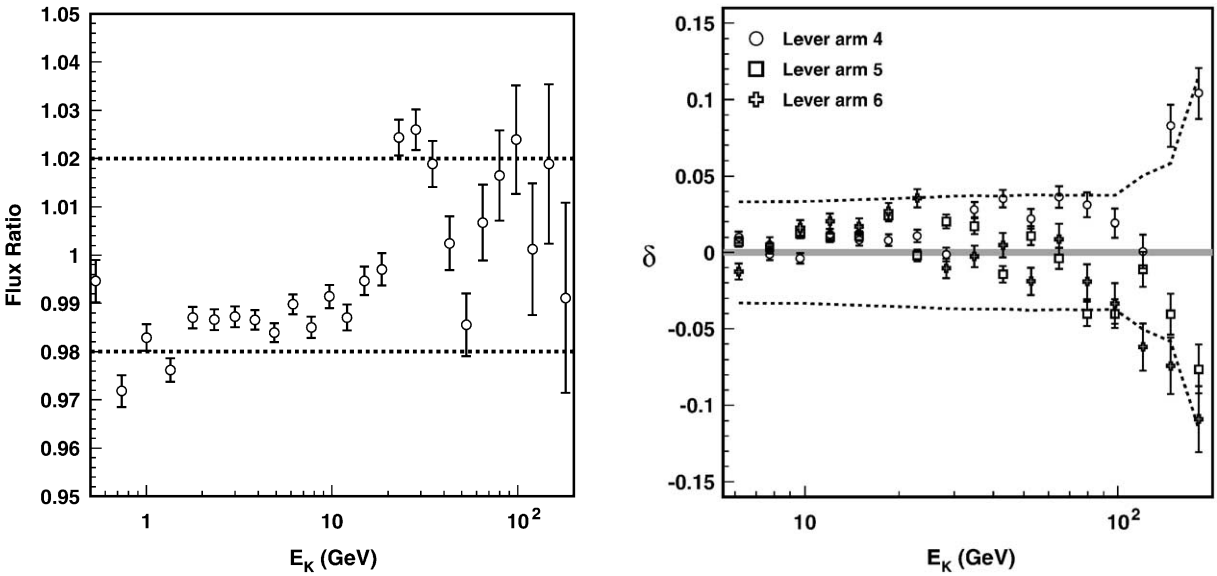

Fig. 4.6. Verification of systematics: ratio of the fluxes computed with and without proton selection quality cuts. The dashed lines show the range of the average systematic error calculated for this case.

Fig. 4.7. Verification of systematics: flux variation, δ, for events with lever arms in the tracker which correspond to 4, 5 or 6 planes. The dashed lines show the range of the calculated systematic errors.

We present 6 examples:

(1) Fig. 4.4 shows the flux variation, $\delta \equiv (\text{flux}/\text{average flux}) - 1$ as a function of energy, for the three data collection periods, corresponding to the three different shuttle orientations, compared with the systematic error calculated for this case.
(2) Fig. 4.5 shows the flux averaged above 20 GeV versus different intervals of the corrected geomagnetic latitude [46], Θ_{M}, at which the protons were detected compared with the systematic error calculated for this case.
(3) Fig. 4.6 shows the ratio of the flux with and without proton selection quality cuts. As seen, the variation is within the systematic error for this case.
(4) Fig. 4.7 shows the variation of the flux, δ, for events which had different lever arms in the tracker, corresponding to the number of tracker planes used in the fit. Again, the variation is within the range of the systematic errors for this case.
(5) The systematic error assigned to the unfolding was checked at several energies using the test beam measurements. Fig. 4.8a shows how the spectrum changes if the unfolding matrix is artificially varied by smearing the alignment between different tracker ladders by an additional 10 μm. At $\sim$100 GeV this corresponds to varying the momentum resolution by 15%.
(6) Fig. 4.8b gives an estimate of the accuracy of the unfolding method by comparing two completely different deconvolution techniques [43–45,47]:

A: The solution of an overdetermined system of linear equations by a method of converged weights [37].

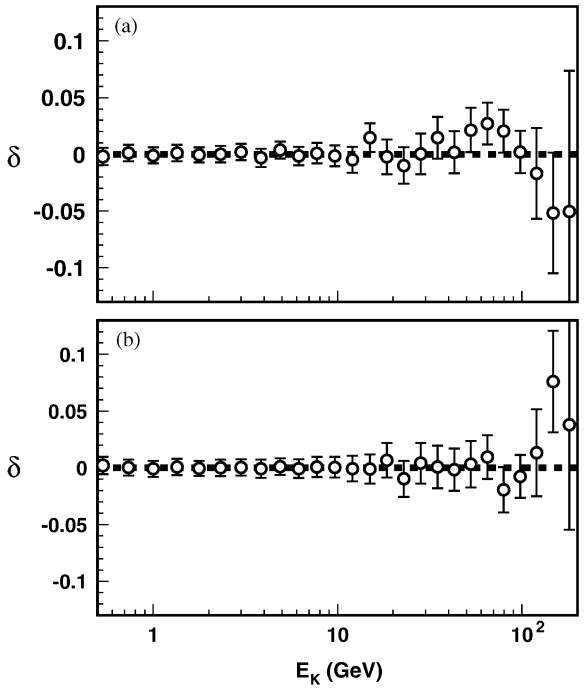

Fig. 4.8. Verification of systematics: (a) variation of the flux, δ, computed with a resolution matrix including an artificial smearing of the alignment by an additional 10 μm. (b) Variation of the flux, δ, calculated with two different unfolding methods.

B: "Classical" unfolding by regularization, namely minimization of the function [47]:

$$\left(\frac{\int f(x')K(x,x')\,\mathrm{d}x' - g(x)}{\epsilon(x)}\right)^2 + \alpha\left(\frac{\mathrm{d}^2 f}{\mathrm{d}x^2}\right)^2 ,$$

where $g(x)$ is the measurement, $\epsilon(x)$ its error, $K(k,x')$ is the resolution matrix, $f(x)$ is the solution and α is a regularization parameter. This method tends to give a smoother solution, since the searched function is a priori assumed to be a "smooth" one, with the most probable "smoothness" estimated from Bayes' theorem.

Up to $\sim$100 GeV the two methods agree within 2–3%. As the unfolding systematics were understood for both methods, the average of the two procedures was used. The input errors for both procedures were the corresponding statistical errors and the systematics of the resolution matrix used. [11]

In these examples, and in all other cases, the assigned systematic errors were found to be correct.

[11] In our previous publication [37] the flux dependence on energy and latitude was presented. These fluxes cannot be combined as such since the errors are correlated through the systematics of the resolution matrix.

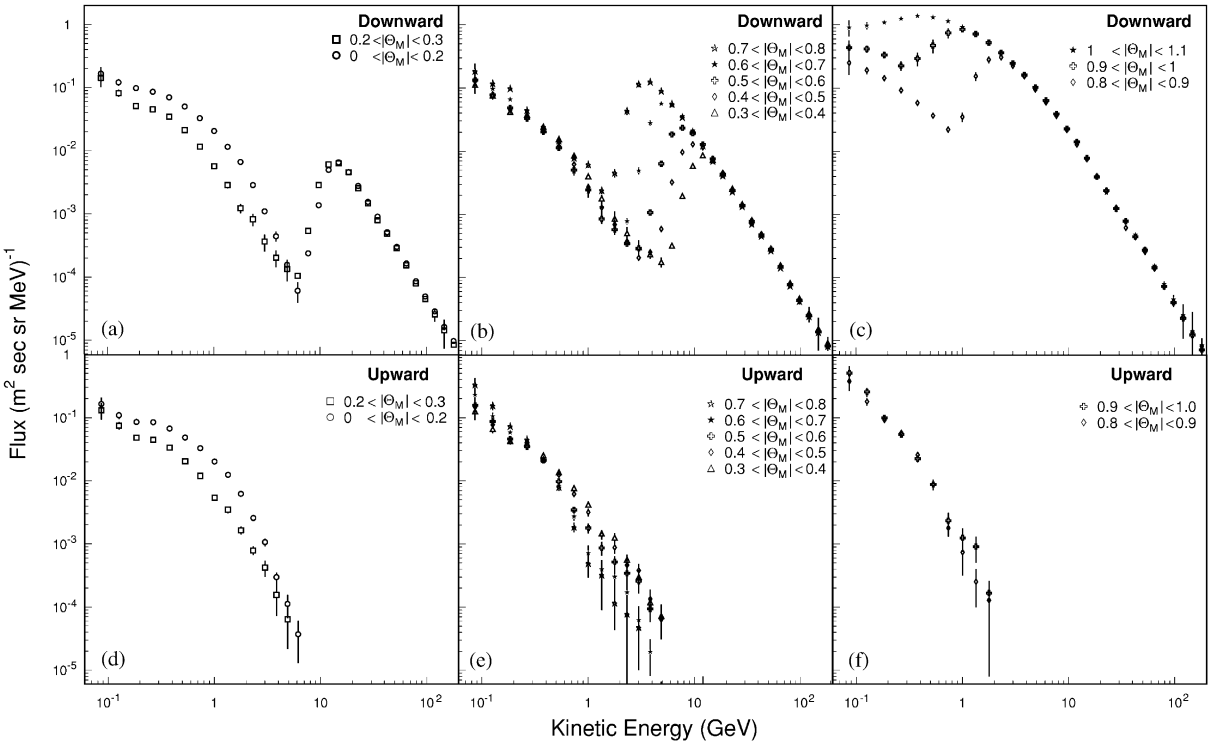

Fig. 4.9. Flux spectra for (a–c) downward and (d–f) upward going protons separated according to the geomagnetic latitude, Θ_M, at which they were detected.

4.3. Results and interpretation

The differential spectra in terms of kinetic energy for downward and upward going protons integrated over incident angles within 32° of the AMS z-axis, which was within 1° of the zenith or nadir, are presented in Fig. 4.9 and Tables 4.5–4.7. Fig. 4.10 presents the downward lepton spectra integrated over incident angles within 25° of the AMS z-axis, which was within 1° of the zenith. The measurements have been binned according to the absolute value of the corrected geomagnetic latitude [46], $|\Theta_M|$ (radians), at which they were detected. The effect of the geomagnetic cutoff and the decrease in this cutoff with increasing $|\Theta_M|$ is particularly visible in the downward spectra. We observe two spectra: a primary one, i.e. above geomagnetic cutoff, and a *second spectrum* below the cutoff. As we shall see these two spectra substantially differ and we analyse them separately. To understand the difference the particle trajectories were traced [48] back from their measured incident angle, location and momentum, through the geomagnetic field [49]. This was continued until the trajectory was traced to outside the Earth's magnetosphere or until it crossed the top of the atmosphere at an altitude of 40 km. The spectra from particles which were traced to originate far away from Earth are classified as "primary" and those from particles which originate in the atmosphere as "second" spectra. In practice particles below the cutoff are from the second spectra, however the tracing provides a cleaner separation in the transition region.

Table 4.5
Differential downward proton flux spectra for lower latitudes

E_K (GeV)	Downward proton flux $(m^2\ s\ sr\ MeV)^{-1}$ Geomagnetic latitude range				
	$\lvert\Theta_M\rvert < 0.2$	$0.2 \leqslant \lvert\Theta_M\rvert < 0.3$	$0.3 \leqslant \lvert\Theta_M\rvert < 0.4$	$0.4 \leqslant \lvert\Theta_M\rvert < 0.5$	$0.5 \leqslant \lvert\Theta_M\rvert < 0.6$
0.07–0.10	$(16.7 \pm 4.4) \times 10^{-2}$	$(14.2 \pm 4.0) \times 10^{-2}$	$(11.2 \pm 3.1) \times 10^{-2}$	$(13.6 \pm 3.8) \times 10^{-2}$	$(13.4 \pm 3.6) \times 10^{-2}$
0.10–0.15	$(12.1 \pm 1.4) \times 10^{-2}$	$(8.2 \pm 1.0) \times 10^{-2}$	$(7.6 \pm 1.0) \times 10^{-2}$	$(7.6 \pm 1.0) \times 10^{-2}$	$(7.7 \pm 1.0) \times 10^{-2}$
0.15–0.22	$(97.9 \pm 4.6) \times 10^{-3}$	$(51.2 \pm 3.2) \times 10^{-3}$	$(41.9 \pm 2.6) \times 10^{-3}$	$(44.6 \pm 3.0) \times 10^{-3}$	$(48.4 \pm 3.3) \times 10^{-3}$
0.22–0.31	$(86.2 \pm 2.8) \times 10^{-3}$	$(45.6 \pm 1.8) \times 10^{-3}$	$(37.9 \pm 1.7) \times 10^{-3}$	$(34.4 \pm 1.5) \times 10^{-3}$	$(32.7 \pm 1.6) \times 10^{-3}$
0.31–0.44	$(70.1 \pm 3.2) \times 10^{-3}$	$(34.6 \pm 1.5) \times 10^{-3}$	$(24.4 \pm 1.1) \times 10^{-3}$	$(21.1 \pm 1.2) \times 10^{-3}$	$(20.2 \pm 1.2) \times 10^{-3}$
0.44–0.62	$(50.4 \pm 2.7) \times 10^{-3}$	$(21.2 \pm 1.2) \times 10^{-3}$	$(155.0 \pm 9.3) \times 10^{-4}$	$(121.0 \pm 9.3) \times 10^{-4}$	$(113.0 \pm 9.0) \times 10^{-4}$
0.62–0.85	$(32.8 \pm 1.9) \times 10^{-3}$	$(116.0 \pm 6.8) \times 10^{-4}$	$(84.9 \pm 6.5) \times 10^{-4}$	$(61.5 \pm 5.6) \times 10^{-4}$	$(50.0 \pm 6.4) \times 10^{-4}$
0.85–1.15	$(20.6 \pm 1.2) \times 10^{-3}$	$(57.2 \pm 4.7) \times 10^{-4}$	$(40.0 \pm 3.8) \times 10^{-4}$	$(26.9 \pm 3.4) \times 10^{-4}$	$(24.2 \pm 4.2) \times 10^{-4}$
1.15–1.54	$(116.0 \pm 6.9) \times 10^{-4}$	$(28.6 \pm 3.3) \times 10^{-4}$	$(17.7 \pm 2.5) \times 10^{-4}$	$(12.7 \pm 2.9) \times 10^{-4}$	$(8.5 \pm 1.4) \times 10^{-4}$
1.54–2.02	$(66.9 \pm 4.2) \times 10^{-4}$	$(12.2 \pm 2.1) \times 10^{-4}$	$(8.5 \pm 2.6) \times 10^{-4}$	$(6.9 \pm 1.4) \times 10^{-4}$	$(5.7 \pm 1.0) \times 10^{-4}$
2.02–2.62	$(28.6 \pm 1.9) \times 10^{-4}$	$(8.2 \pm 1.8) \times 10^{-4}$	$(5.0 \pm 1.3) \times 10^{-4}$	$(37.3 \pm 3.3) \times 10^{-5}$	$(34.2 \pm 1.5) \times 10^{-5}$
2.62–3.38	$(110.0 \pm 9.6) \times 10^{-5}$	$(3.6 \pm 1.1) \times 10^{-4}$	$(30.0 \pm 8.6) \times 10^{-5}$	$(204.0 \pm 7.4) \times 10^{-6}$	$(29.0 \pm 1.4) \times 10^{-5}$
3.38–4.31	$(44.3 \pm 7.9) \times 10^{-5}$	$(20.3 \pm 6.0) \times 10^{-5}$	$(23.2 \pm 3.6) \times 10^{-5}$	$(25.0 \pm 1.3) \times 10^{-5}$	$(10.7 \pm 1.1) \times 10^{-4}$
4.31–5.45	$(15.7 \pm 3.1) \times 10^{-5}$	$(13.4 \pm 4.8) \times 10^{-5}$	$(17.6 \pm 3.2) \times 10^{-5}$	$(58.5 \pm 5.9) \times 10^{-5}$	$(62.9 \pm 6.4) \times 10^{-4}$
5.45–6.86	$(6.1 \pm 2.2) \times 10^{-5}$	$(105.0 \pm 8.7) \times 10^{-6}$	$(31.9 \pm 2.3) \times 10^{-5}$	$(32.1 \pm 3.0) \times 10^{-4}$	$(18.4 \pm 1.4) \times 10^{-3}$
6.86–8.60	$(23.7 \pm 2.1) \times 10^{-5}$	$(53.8 \pm 2.7) \times 10^{-5}$	$(19.5 \pm 1.5) \times 10^{-4}$	$(96.2 \pm 6.4) \times 10^{-4}$	$(23.3 \pm 1.2) \times 10^{-3}$
8.60–10.73	$(138.0 \pm 6.8) \times 10^{-5}$	$(28.6 \pm 1.7) \times 10^{-4}$	$(58.5 \pm 3.3) \times 10^{-4}$	$(128.0 \pm 5.4) \times 10^{-4}$	$(193.0 \pm 5.1) \times 10^{-4}$
10.73–13.34	$(49.5 \pm 1.8) \times 10^{-4}$	$(60.9 \pm 2.4) \times 10^{-4}$	$(85.7 \pm 3.1) \times 10^{-4}$	$(115.0 \pm 2.8) \times 10^{-4}$	$(128.0 \pm 3.7) \times 10^{-4}$
13.34–16.55	$(65.7 \pm 2.1) \times 10^{-4}$	$(63.4 \pm 1.8) \times 10^{-4}$	$(72.1 \pm 2.1) \times 10^{-4}$	$(75.6 \pm 2.5) \times 10^{-4}$	$(75.6 \pm 2.7) \times 10^{-4}$
16.55–20.48	$(45.7 \pm 1.7) \times 10^{-4}$	$(45.5 \pm 1.7) \times 10^{-4}$	$(44.4 \pm 1.5) \times 10^{-4}$	$(45.2 \pm 1.8) \times 10^{-4}$	$(43.3 \pm 1.2) \times 10^{-4}$
20.48–25.29	$(27.7 \pm 1.0) \times 10^{-4}$	$(25.5 \pm 1.0) \times 10^{-4}$	$(255.0 \pm 9.8) \times 10^{-5}$	$(248.0 \pm 9.6) \times 10^{-5}$	$(24.0 \pm 1.0) \times 10^{-4}$
25.29–31.20	$(155.0 \pm 5.9) \times 10^{-5}$	$(147.0 \pm 7.1) \times 10^{-5}$	$(144.0 \pm 6.8) \times 10^{-5}$	$(142.0 \pm 6.7) \times 10^{-5}$	$(138.0 \pm 5.6) \times 10^{-5}$
31.20–38.43	$(90.5 \pm 4.1) \times 10^{-5}$	$(79.2 \pm 4.7) \times 10^{-5}$	$(80.5 \pm 4.5) \times 10^{-5}$	$(80.0 \pm 4.3) \times 10^{-5}$	$(77.1 \pm 4.3) \times 10^{-5}$
38.43–47.30	$(51.4 \pm 2.2) \times 10^{-5}$	$(48.9 \pm 3.0) \times 10^{-5}$	$(48.2 \pm 2.5) \times 10^{-5}$	$(48.2 \pm 3.0) \times 10^{-5}$	$(47.1 \pm 2.7) \times 10^{-5}$
47.30–58.16	$(30.0 \pm 1.7) \times 10^{-5}$	$(28.6 \pm 2.0) \times 10^{-5}$	$(28.7 \pm 1.8) \times 10^{-5}$	$(28.4 \pm 1.8) \times 10^{-5}$	$(27.7 \pm 1.8) \times 10^{-5}$
58.16–71.48	$(164.0 \pm 8.8) \times 10^{-6}$	$(15.4 \pm 1.2) \times 10^{-5}$	$(15.6 \pm 1.2) \times 10^{-5}$	$(154.0 \pm 8.8) \times 10^{-6}$	$(149.0 \pm 9.9) \times 10^{-6}$
71.48–87.79	$(86.1 \pm 3.9) \times 10^{-6}$	$(79.6 \pm 4.7) \times 10^{-6}$	$(81.5 \pm 6.4) \times 10^{-6}$	$(80.2 \pm 5.9) \times 10^{-6}$	$(76.7 \pm 5.1) \times 10^{-6}$
87.79–107.78	$(49.4 \pm 2.9) \times 10^{-6}$	$(45.0 \pm 4.6) \times 10^{-6}$	$(46.6 \pm 4.8) \times 10^{-6}$	$(45.8 \pm 2.8) \times 10^{-6}$	$(43.4 \pm 2.6) \times 10^{-6}$
107.78–132.27	$(28.6 \pm 3.1) \times 10^{-6}$	$(25.7 \pm 6.1) \times 10^{-6}$	$(26.9 \pm 7.3) \times 10^{-6}$	$(26.4 \pm 6.2) \times 10^{-6}$	$(24.8 \pm 4.6) \times 10^{-6}$
132.27–162.29	$(16.2 \pm 1.8) \times 10^{-6}$	$(14.3 \pm 7.0) \times 10^{-6}$	$(15.2 \pm 5.2) \times 10^{-6}$	$(14.9 \pm 7.9) \times 10^{-6}$	$(13.8 \pm 6.3) \times 10^{-6}$
162.29–199.06	$(97.2 \pm 5.1) \times 10^{-7}$	$(84.8 \pm 6.7) \times 10^{-7}$	$(9.1 \pm 2.3) \times 10^{-6}$	$(8.9 \pm 1.8) \times 10^{-6}$	$(82.1 \pm 6.2) \times 10^{-7}$

Table 4.6
Differential downward proton flux spectra for higher latitudes

E_K (GeV)	Downward proton flux $(m^2\ s\ sr\ MeV)^{-1}$ Geomagnetic latitude range				
	$0.6 \leqslant \lvert\Theta_M\rvert < 0.7$	$0.7 \leqslant \lvert\Theta_M\rvert < 0.8$	$0.8 \leqslant \lvert\Theta_M\rvert < 0.9$	$0.9 \leqslant \lvert\Theta_M\rvert < 1.0$	$1.0 \leqslant \lvert\Theta_M\rvert$
0.07–0.10	$(12.2 \pm 3.5) \times 10^{-2}$	$(18.5 \pm 5.9) \times 10^{-2}$	$(25.1 \pm 8.9) \times 10^{-2}$	$(4.3 \pm 1.3) \times 10^{-1}$	$(9.2 \pm 2.6) \times 10^{-1}$
0.10–0.15	$(9.7 \pm 1.3) \times 10^{-2}$	$(11.8 \pm 1.6) \times 10^{-2}$	$(19.1 \pm 2.6) \times 10^{-2}$	$(41.8 \pm 5.6) \times 10^{-2}$	$(9.8 \pm 1.2) \times 10^{-1}$
0.15–0.22	$(66.0 \pm 3.7) \times 10^{-3}$	$(97.3 \pm 5.9) \times 10^{-3}$	$(144.0 \pm 8.9) \times 10^{-3}$	$(33.6 \pm 3.3) \times 10^{-2}$	$(109.0 \pm 6.7) \times 10^{-2}$
0.22–0.31	$(44.4 \pm 1.6) \times 10^{-3}$	$(44.2 \pm 2.0) \times 10^{-3}$	$(92.4 \pm 6.9) \times 10^{-3}$	$(22.6 \pm 3.9) \times 10^{-2}$	$(126.0 \pm 5.3) \times 10^{-2}$
0.31–0.44	$(24.1 \pm 1.7) \times 10^{-3}$	$(23.8 \pm 1.3) \times 10^{-3}$	$(58.3 \pm 4.8) \times 10^{-3}$	$(29.3 \pm 7.1) \times 10^{-2}$	$(139.0 \pm 4.1) \times 10^{-2}$
0.44–0.62	$(108.0 \pm 8.8) \times 10^{-4}$	$(14.4 \pm 1.0) \times 10^{-3}$	$(36.6 \pm 3.5) \times 10^{-3}$	$(4.7 \pm 1.1) \times 10^{-1}$	$(132.0 \pm 4.8) \times 10^{-2}$
0.62–0.85	$(47.8 \pm 6.7) \times 10^{-4}$	$(77.2 \pm 6.9) \times 10^{-4}$	$(22.0 \pm 2.5) \times 10^{-3}$	$(7.5 \pm 1.3) \times 10^{-1}$	$(114.0 \pm 4.2) \times 10^{-2}$
0.85–1.15	$(23.1 \pm 4.9) \times 10^{-4}$	$(60.9 \pm 6.5) \times 10^{-4}$	$(34.9 \pm 5.8) \times 10^{-3}$	$(85.3 \pm 7.5) \times 10^{-2}$	$(92.8 \pm 3.2) \times 10^{-2}$
1.15–1.54	$(13.1 \pm 2.2) \times 10^{-4}$	$(23.7 \pm 2.9) \times 10^{-4}$	$(15.4 \pm 2.4) \times 10^{-2}$	$(71.7 \pm 4.5) \times 10^{-2}$	$(72.4 \pm 2.4) \times 10^{-2}$
1.54–2.02	$(7.7 \pm 1.2) \times 10^{-4}$	$(44.8 \pm 6.7) \times 10^{-4}$	$(28.1 \pm 3.3) \times 10^{-2}$	$(52.4 \pm 4.5) \times 10^{-2}$	$(51.1 \pm 1.4) \times 10^{-2}$
2.02–2.62	$(77.7 \pm 8.3) \times 10^{-5}$	$(43.1 \pm 5.8) \times 10^{-3}$	$(30.9 \pm 1.8) \times 10^{-2}$	$(36.2 \pm 2.9) \times 10^{-2}$	$(37.0 \pm 1.1) \times 10^{-2}$
2.62–3.38	$(49.1 \pm 5.9) \times 10^{-4}$	$(11.4 \pm 1.1) \times 10^{-2}$	$(22.6 \pm 1.4) \times 10^{-2}$	$(24.8 \pm 2.1) \times 10^{-2}$	$(241.0 \pm 6.4) \times 10^{-3}$
3.38–4.31	$(27.9 \pm 2.9) \times 10^{-3}$	$(124.0 \pm 4.6) \times 10^{-3}$	$(15.4 \pm 1.1) \times 10^{-2}$	$(16.2 \pm 1.1) \times 10^{-2}$	$(163.0 \pm 3.1) \times 10^{-3}$
4.31–5.45	$(56.4 \pm 4.0) \times 10^{-3}$	$(88.4 \pm 4.3) \times 10^{-3}$	$(95.3 \pm 5.9) \times 10^{-3}$	$(103.0 \pm 7.7) \times 10^{-3}$	$(102.0 \pm 2.9) \times 10^{-3}$
5.45–6.86	$(52.6 \pm 1.7) \times 10^{-3}$	$(55.6 \pm 3.2) \times 10^{-3}$	$(59.3 \pm 3.5) \times 10^{-3}$	$(63.8 \pm 5.0) \times 10^{-3}$	$(61.4 \pm 1.3) \times 10^{-3}$
6.86–8.60	$(35.6 \pm 1.2) \times 10^{-3}$	$(34.0 \pm 1.8) \times 10^{-3}$	$(36.3 \pm 2.6) \times 10^{-3}$	$(39.0 \pm 2.8) \times 10^{-3}$	$(390.0 \pm 8.2) \times 10^{-4}$
8.60–10.73	$(212.0 \pm 9.0) \times 10^{-4}$	$(20.2 \pm 1.1) \times 10^{-3}$	$(21.8 \pm 1.6) \times 10^{-3}$	$(22.5 \pm 1.6) \times 10^{-3}$	$(223.0 \pm 6.5) \times 10^{-4}$
10.73–13.34	$(129.0 \pm 5.3) \times 10^{-4}$	$(121.0 \pm 6.4) \times 10^{-4}$	$(128.0 \pm 8.0) \times 10^{-4}$	$(14.1 \pm 1.3) \times 10^{-3}$	$(136.0 \pm 4.5) \times 10^{-4}$
13.34–16.55	$(75.8 \pm 3.3) \times 10^{-4}$	$(69.0 \pm 3.8) \times 10^{-4}$	$(75.2 \pm 4.3) \times 10^{-4}$	$(78.0 \pm 5.7) \times 10^{-4}$	$(76.2 \pm 2.7) \times 10^{-4}$
16.55–20.48	$(41.7 \pm 1.5) \times 10^{-4}$	$(40.5 \pm 2.1) \times 10^{-4}$	$(40.2 \pm 3.0) \times 10^{-4}$	$(39.3 \pm 3.3) \times 10^{-4}$	$(39.6 \pm 1.3) \times 10^{-4}$
20.48–25.29	$(24.9 \pm 1.1) \times 10^{-4}$	$(22.7 \pm 1.3) \times 10^{-4}$	$(237.0 \pm 8.0) \times 10^{-5}$	$(23.8 \pm 2.0) \times 10^{-4}$	$(22.0 \pm 1.3) \times 10^{-4}$
25.29–31.20	$(134.0 \pm 5.6) \times 10^{-5}$	$(132.0 \pm 8.7) \times 10^{-5}$	$(127.0 \pm 6.4) \times 10^{-5}$	$(12.3 \pm 1.4) \times 10^{-4}$	$(118.0 \pm 7.9) \times 10^{-5}$
31.20–38.43	$(75.1 \pm 4.0) \times 10^{-5}$	$(69.2 \pm 4.5) \times 10^{-5}$	$(61.5 \pm 5.7) \times 10^{-5}$	$(78.0 \pm 8.8) \times 10^{-5}$	$(76.7 \pm 6.5) \times 10^{-5}$
38.43–47.30	$(46.0 \pm 2.7) \times 10^{-5}$	$(44.7 \pm 2.8) \times 10^{-5}$	$(44.0 \pm 3.5) \times 10^{-5}$	$(44.1 \pm 4.6) \times 10^{-5}$	$(47.7 \pm 3.7) \times 10^{-5}$
47.30–58.16	$(27.0 \pm 1.8) \times 10^{-5}$	$(26.3 \pm 1.9) \times 10^{-5}$	$(25.7 \pm 2.8) \times 10^{-5}$	$(27.0 \pm 2.6) \times 10^{-5}$	$(28.5 \pm 2.6) \times 10^{-5}$
58.16–71.48	$(14.6 \pm 1.2) \times 10^{-5}$	$(142.0 \pm 9.9) \times 10^{-6}$	$(13.9 \pm 1.3) \times 10^{-5}$	$(14.3 \pm 1.5) \times 10^{-5}$	$(154.0 \pm 9.8) \times 10^{-6}$
71.48–87.79	$(76.0 \pm 4.6) \times 10^{-6}$	$(72.9 \pm 4.5) \times 10^{-6}$	$(71.7 \pm 6.4) \times 10^{-6}$	$(72.5 \pm 6.5) \times 10^{-6}$	$(79.3 \pm 8.7) \times 10^{-6}$
87.79–107.78	$(43.5 \pm 5.8) \times 10^{-6}$	$(41.5 \pm 3.0) \times 10^{-6}$	$(41.1 \pm 4.1) \times 10^{-6}$	$(40.3 \pm 6.3) \times 10^{-6}$	$(44.8 \pm 7.9) \times 10^{-6}$
107.78–132.27	$(25.2 \pm 4.5) \times 10^{-6}$	$(23.9 \pm 4.4) \times 10^{-6}$	$(23.9 \pm 4.4) \times 10^{-6}$	$(2.3 \pm 1.2) \times 10^{-5}$	$(2.6 \pm 1.2) \times 10^{-5}$
132.27–162.29	$(14.3 \pm 3.9) \times 10^{-6}$	$(13.4 \pm 4.7) \times 10^{-6}$	$(13.6 \pm 6.5) \times 10^{-6}$	$(12.3 \pm 8.9) \times 10^{-6}$	$(1.4 \pm 1.4) \times 10^{-5}$
162.29–199.06	$(8.6 \pm 1.5) \times 10^{-6}$	$(80.6 \pm 4.3) \times 10^{-7}$	$(8.2 \pm 1.3) \times 10^{-6}$	$(7.2 \pm 3.7) \times 10^{-6}$	$(8.5 \pm 2.4) \times 10^{-6}$

Table 4.7
Differential upward proton flux spectra

E_K (GeV)	Upward proton flux $(m^2\ s\ sr\ MeV)^{-1}$ Geomagnetic latitude range				
	$\lvert\Theta_M\rvert < 0.2$	$0.2 \leqslant \lvert\Theta_M\rvert < 0.3$	$0.3 \leqslant \lvert\Theta_M\rvert < 0.4$	$0.4 \leqslant \lvert\Theta_M\rvert < 0.5$	$0.5 \leqslant \lvert\Theta_M\rvert < 0.6$
0.07–0.10	$(16.4 \pm 4.4) \times 10^{-2}$	$(13.1 \pm 3.9) \times 10^{-2}$	$(12.6 \pm 3.5) \times 10^{-2}$	$(14.7 \pm 4.1) \times 10^{-2}$	$(15.8 \pm 4.7) \times 10^{-2}$
0.10–0.15	$(10.9 \pm 1.4) \times 10^{-2}$	$(7.5 \pm 1.0) \times 10^{-2}$	$(66.0 \pm 9.2) \times 10^{-3}$	$(7.7 \pm 1.1) \times 10^{-2}$	$(8.7 \pm 1.2) \times 10^{-2}$
0.15–0.22	$(85.3 \pm 4.9) \times 10^{-3}$	$(48.1 \pm 3.5) \times 10^{-3}$	$(42.7 \pm 2.8) \times 10^{-3}$	$(42.2 \pm 2.8) \times 10^{-3}$	$(46.3 \pm 2.8) \times 10^{-3}$
0.22–0.31	$(84.8 \pm 3.8) \times 10^{-3}$	$(44.5 \pm 2.1) \times 10^{-3}$	$(39.3 \pm 1.9) \times 10^{-3}$	$(35.5 \pm 1.8) \times 10^{-3}$	$(34.6 \pm 1.5) \times 10^{-3}$
0.31–0.44	$(66.8 \pm 3.4) \times 10^{-3}$	$(33.6 \pm 1.7) \times 10^{-3}$	$(25.4 \pm 1.1) \times 10^{-3}$	$(21.4 \pm 1.1) \times 10^{-3}$	$(21.0 \pm 1.1) \times 10^{-3}$
0.44–0.62	$(48.4 \pm 2.7) \times 10^{-3}$	$(20.3 \pm 1.2) \times 10^{-3}$	$(136.0 \pm 8.3) \times 10^{-4}$	$(124.0 \pm 9.2) \times 10^{-4}$	$(97.6 \pm 8.1) \times 10^{-4}$
0.62–0.85	$(32.7 \pm 2.0) \times 10^{-3}$	$(120.0 \pm 8.6) \times 10^{-4}$	$(76.4 \pm 5.6) \times 10^{-4}$	$(61.9 \pm 6.1) \times 10^{-4}$	$(34.8 \pm 4.3) \times 10^{-4}$
0.85–1.15	$(20.2 \pm 1.1) \times 10^{-3}$	$(53.9 \pm 4.6) \times 10^{-4}$	$(42.0 \pm 4.5) \times 10^{-4}$	$(31.9 \pm 4.6) \times 10^{-4}$	$(17.9 \pm 3.3) \times 10^{-4}$
1.15–1.54	$(124.0 \pm 7.1) \times 10^{-4}$	$(34.8 \pm 4.4) \times 10^{-4}$	$(14.7 \pm 1.8) \times 10^{-4}$	$(14.0 \pm 2.3) \times 10^{-4}$	$(8.6 \pm 2.1) \times 10^{-4}$
1.54–2.02	$(62.0 \pm 4.2) \times 10^{-4}$	$(16.4 \pm 2.3) \times 10^{-4}$	$(12.5 \pm 2.3) \times 10^{-4}$	$(8.8 \pm 1.8) \times 10^{-4}$	$(5.2 \pm 1.2) \times 10^{-4}$
2.02–2.62	$(25.9 \pm 1.8) \times 10^{-4}$	$(7.9 \pm 1.3) \times 10^{-4}$	$(5.6 \pm 1.1) \times 10^{-4}$	$(4.6 \pm 1.2) \times 10^{-4}$	$(3.4 \pm 1.1) \times 10^{-4}$
2.62–3.38	$(10.7 \pm 1.5) \times 10^{-4}$	$(4.2 \pm 1.2) \times 10^{-4}$	$(29.9 \pm 8.7) \times 10^{-5}$	$(38.3 \pm 10.) \times 10^{-5}$	$(25.9 \pm 9.6) \times 10^{-5}$
3.38–4.31	$(29.7 \pm 5.7) \times 10^{-5}$	$(15.6 \pm 8.3) \times 10^{-5}$	$(11.9 \pm 4.9) \times 10^{-5}$	$(13.4 \pm 5.7) \times 10^{-5}$	$(9.4 \pm 3.7) \times 10^{-5}$
4.31–5.45	$(11.2 \pm 4.6) \times 10^{-5}$	$(6.4 \pm 4.2) \times 10^{-5}$	$(7.2 \pm 3.8) \times 10^{-5}$	$(6.4 \pm 3.3) \times 10^{-5}$	
5.45–6.86	$(3.7 \pm 2.4) \times 10^{-5}$				

E_K (GeV)	Geomagnetic latitude range			
	$0.6 \leqslant \lvert\Theta_M\rvert < 0.7$	$0.7 \leqslant \lvert\Theta_M\rvert < 0.8$	$0.8 \leqslant \lvert\Theta_M\rvert < 0.9$	$0.9 \leqslant \lvert\Theta_M\rvert < 1.0$
0.07–0.10	$(23.1 \pm 6.8) \times 10^{-2}$	$(32.9 \pm 9.5) \times 10^{-2}$	$(3.8 \pm 1.1) \times 10^{-1}$	$(5.1 \pm 1.5) \times 10^{-1}$
0.10–0.15	$(10.5 \pm 1.5) \times 10^{-2}$	$(15.4 \pm 2.3) \times 10^{-2}$	$(18.0 \pm 2.4) \times 10^{-2}$	$(25.5 \pm 4.1) \times 10^{-2}$
0.15–0.22	$(58.1 \pm 3.8) \times 10^{-3}$	$(72.5 \pm 5.4) \times 10^{-3}$	$(91.9 \pm 6.2) \times 10^{-3}$	$(99.8 \pm 8.4) \times 10^{-3}$
0.22–0.31	$(43.0 \pm 2.1) \times 10^{-3}$	$(44.8 \pm 3.4) \times 10^{-3}$	$(57.4 \pm 3.3) \times 10^{-3}$	$(54.0 \pm 4.9) \times 10^{-3}$
0.31–0.44	$(20.7 \pm 1.1) \times 10^{-3}$	$(21.7 \pm 1.9) \times 10^{-3}$	$(25.7 \pm 2.6) \times 10^{-3}$	$(22.5 \pm 2.9) \times 10^{-3}$
0.44–0.62	$(83.4 \pm 8.0) \times 10^{-4}$	$(78.6 \pm 9.3) \times 10^{-4}$	$(8.8 \pm 1.2) \times 10^{-3}$	$(8.8 \pm 1.7) \times 10^{-3}$
0.62–0.85	$(27.3 \pm 4.0) \times 10^{-4}$	$(18.4 \pm 3.2) \times 10^{-4}$	$(17.9 \pm 4.8) \times 10^{-4}$	$(23.4 \pm 8.0) \times 10^{-4}$
0.85–1.15	$(7.2 \pm 2.3) \times 10^{-4}$	$(4.9 \pm 1.9) \times 10^{-4}$	$(7.4 \pm 4.2) \times 10^{-4}$	$(12.6 \pm 5.1) \times 10^{-4}$
1.15–1.54	$(4.0 \pm 1.3) \times 10^{-4}$	$(3.2 \pm 2.3) \times 10^{-4}$	$(2.5 \pm 1.5) \times 10^{-4}$	$(9.1 \pm 4.0) \times 10^{-4}$
1.54–2.02	$(3.0 \pm 1.4) \times 10^{-4}$	$(11.6 \pm 7.2) \times 10^{-5}$	$(1.3 \pm 1.2) \times 10^{-4}$	$(16.8 \pm 9.3) \times 10^{-5}$
2.02–2.62	$(1.7 \pm 1.2) \times 10^{-4}$	$(7.7 \pm 7.4) \times 10^{-5}$		
2.62–3.38	$(6.3 \pm 4.1) \times 10^{-5}$	$(4.8 \pm 3.8) \times 10^{-5}$		
3.38–4.31	$(2.0 \pm 1.1) \times 10^{-5}$			

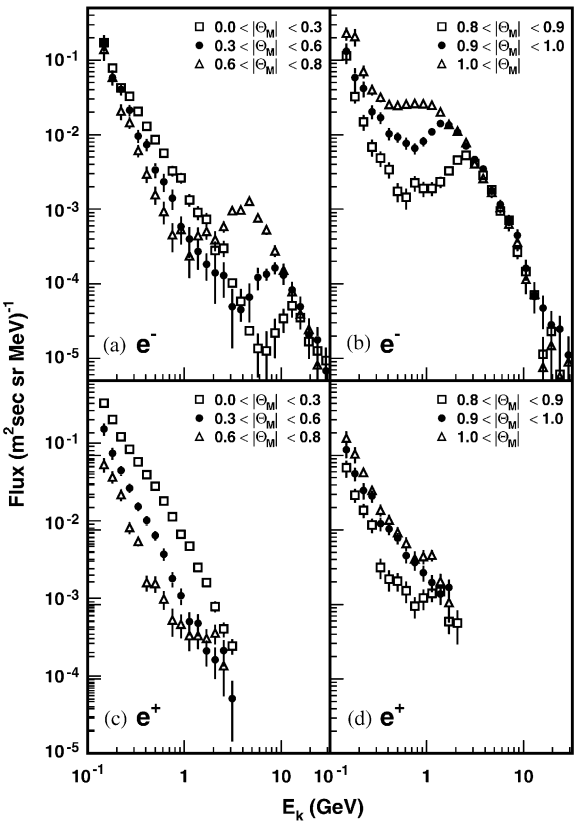

Fig. 4.10. (a,b) Flux spectra for downward going electrons and (c, d) positrons, separated according to the geomagnetic latitude at which they were detected.

The differential helium spectra as a function of the incident rigidity for the zenith pointing data is presented in Fig. 4.11. The results have been averaged within three ranges of the absolute value of the corrected geomagnetic latitude [46], $|\Theta_M|$, at which they were observed.

The figure shows the effect of the geomagnetic cutoff which decreases with increasing $|\Theta_M|$. In addition to the above cutoff, or primary, spectrum, Fig. 4.11 also shows the presence of a second spectrum below cutoff for $|\Theta_M| < 0.8$ rad, which is much less pronounced for He compared to the proton, e^+ or e^- data. Since the spectra above cutoff are identical, the data above cutoff from the three attitudes were combined together.

The primary proton spectrum together with the statistical and three systematic errors is presented in Table 4.8 and with the errors combined in quadrature in Fig. 4.12.

4.3.1. Primary spectrum

The primary spectrum is the interstellar spectrum distorted at low energies by the solar modulation, i.e. by the magnetic field of the Sun, which is directly related to the level of solar activity. Current theoretical models of the cosmic ray origin and propagation predict a power law spectrum and can approximately describe the existing experimental data [26,36,50–52]. The primary proton spectrum

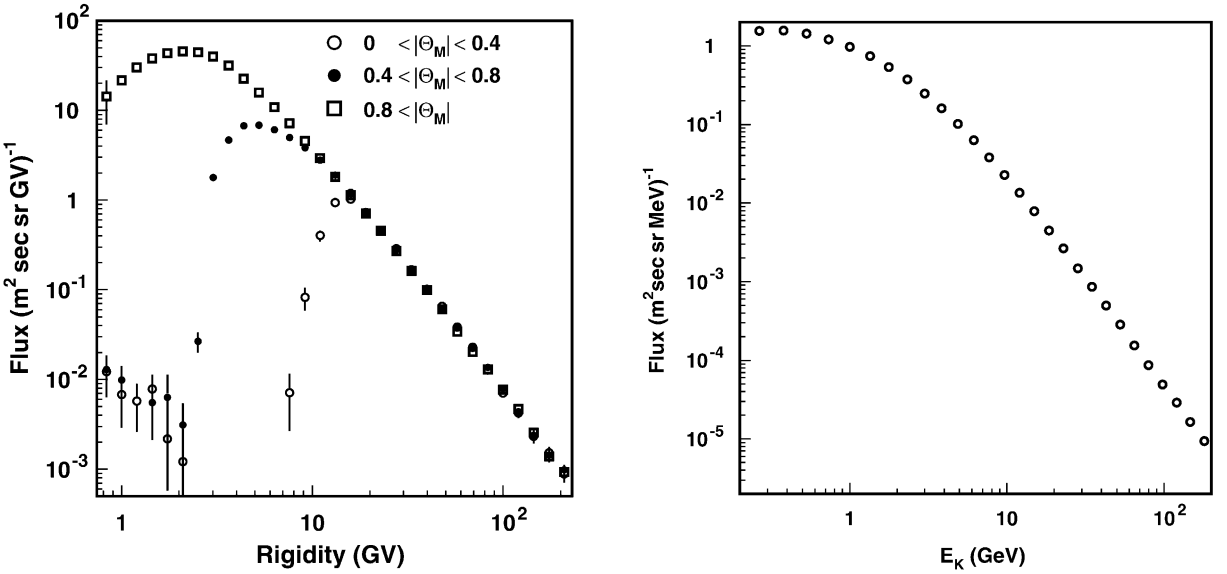

Fig. 4.11. Helium flux spectra for the zenith pointing data separated according to the geomagnetic latitude, Θ_M, at which they were detected.

Fig. 4.12. The primary proton flux. Fitting this spectrum to a power law in rigidity, $\Phi = \Phi_0 R^{-\gamma}$, over the range $10 < R < 200$ GV yields $\gamma = 2.78 \pm 0.009(\text{fit}) \pm 0.019(\text{sys})$ and $\Phi_0 = 17.1 \pm 0.15(\text{fit}) \pm 1.3(\text{sys}) \pm 1.5(\gamma)$ GV$^{2.78}$/(m^2 s sr MV).

has been parameterized by a power law in rigidity, $\Phi_0 \times R^{-\gamma}$. Fitting [45] the measured spectrum over the rigidity range $10 < R < 200$ GV, i.e. well above cutoff, yields:

$$\gamma = 2.78 \pm 0.009(\text{fit}) \pm 0.019(\text{sys}) ,$$

$$\Phi_0 = 17.1 \pm 0.15(\text{fit}) \pm 1.3(\text{sys}) \pm 1.5(\gamma) \frac{\text{GV}^{2.78}}{\text{m}^2 \text{ s sr MV}} .$$

The systematic uncertainty in γ was estimated from the uncertainty in the acceptance (0.006), the dependence of the resolution function on the particle direction and track length within one sigma (0.015), variation of the tracker bending coordinate resolution by ± 4 μm (0.005) and variation of the selection criteria (0.010). The third uncertainty quoted for Φ_0 reflects the systematic uncertainty in γ.

For comparision with balloon measurements [21,23,53,54] the data has been scaled by $E_K^{2.5}$ as shown in Fig. 4.13. The flux scaled by $E_K^{2.75}$ is shown in Fig. 4.14. As seen from Fig. 4.14, our data is a smooth function which is flat above 20 GeV [55]. Fig. 4.14 also shows the proton spectrum assumed to calculate the spectrum of atmospheric neutrinos [31]. One observes a substantial deviation from the AMS measurement.

The differential primary helium spectrum is presented in Fig. 4.15 and Table 4.9. As seen from Fig. 4.15 our data are only marginally in agreement with the spectrum used to calculate atmospheric neutrino spectra [31]. Our results are compared to recent balloon experiment results [23,28,53,54] in Fig. 4.16.[12] The spectrum has been fit [45] over the rigidity range $20 < R < 200$ GV. To avoid

[12] A ^{3}He fraction of 0.15 ± 0.05 was assumed.

Table 4.8
Primary proton spectrum

Kinetic energy	Flux $\pm \varepsilon_{stat} \pm \varepsilon_{sys1} \pm \varepsilon_{sys2} \pm \varepsilon_{sys3}$
0.22–0.31	$(154.0 \pm 1.6 \pm 5.9 \pm 4.0 \pm 1.9) \times 10^{-2}$
0.31–0.44	$(156.0 \pm 0.99 \pm 6.0 \pm 3.8 \pm 1.3) \times 10^{-2}$
0.44–0.62	$(143.0 \pm 0.59 \pm 6.0 \pm 3.6 \pm 1.0) \times 10^{-2}$
0.62–0.85	$(120.0 \pm 0.39 \pm 4.6 \pm 3.1 \pm 0.82) \times 10^{-2}$
0.85–1.15	$(966.0 \pm 2.6 \pm 37.0 \pm 24.0 \pm 6.7) \times 10^{-3}$
1.15–1.54	$(738.0 \pm 1.8 \pm 28.0 \pm 18.0 \pm 5.1) \times 10^{-3}$
1.54–2.02	$(533.0 \pm 1.2 \pm 20.0 \pm 13.0 \pm 3.4) \times 10^{-3}$
2.02–2.62	$(372.0 \pm 0.80 \pm 14.0 \pm 8.9 \pm 2.7) \times 10^{-3}$
2.62–3.38	$(247.0 \pm 0.53 \pm 9.5 \pm 5.8 \pm 1.8) \times 10^{-3}$
3.38–4.31	$(161.0 \pm 0.33 \pm 6.2 \pm 3.7 \pm 1.3) \times 10^{-3}$
4.31–5.45	$(101.0 \pm 0.20 \pm 3.9 \pm 2.3 \pm 0.74) \times 10^{-3}$
5.45–6.86	$(630.0 \pm 1.3 \pm 24.0 \pm 14.0 \pm 5.2) \times 10^{-4}$
6.86–8.60	$(37.8 \pm 0.84 \pm 14.0 \pm 8.6 \pm 3.3) \times 10^{-4}$
8.60–10.7	$(226.0 \pm 0.54 \pm 8.7 \pm 5.2 \pm 2.0) \times 10^{-4}$
10.7–13.3	$(135.0 \pm 0.36 \pm 5.2 \pm 3.1 \pm 1.5) \times 10^{-4}$
13.3–16.5	$(786.0 \pm 2.3 \pm 30.0 \pm 18.0 \pm 10.0) \times 10^{-5}$
16.5–20.5	$(449.0 \pm 1.5 \pm 17.0 \pm 11.0 \pm 6.6) \times 10^{-5}$
20.5–25.3	$(266.0 \pm 0.98 \pm 10.0 \pm 6.4 \pm 4.3) \times 10^{-5}$
25.3–31.2	$(148.0 \pm 0.61 \pm 5.7 \pm 3.7 \pm 2.7) \times 10^{-5}$
31.2–38.4	$(856.0 \pm 4.0 \pm 33.0 \pm 22.0 \pm 16.0) \times 10^{-6}$
38.4–47.3	$(496.0 \pm 2.7 \pm 19.0 \pm 13.0 \pm 9.2) \times 10^{-6}$
47.3–58.2	$(284.0 \pm 1.8 \pm 11.0 \pm 7.9 \pm 5.7) \times 10^{-6}$
58.2–71.5	$(154.0 \pm 1.2 \pm 5.9 \pm 4.4 \pm 3.0) \times 10^{-6}$
71.5–87.8	$(86.2 \pm 0.80 \pm 3.3 \pm 2.4 \pm 1.7) \times 10^{-6}$
87.8–108.0	$(49.4 \pm 0.55 \pm 1.9 \pm 1.3 \pm 0.94) \times 10^{-6}$
108.0–132.0	$(29.0 \pm 0.40 \pm 1.1 \pm 0.78 \pm 1.1) \times 10^{-6}$
132.0–162.0	$(16.4 \pm 0.27 \pm 0.63 \pm 0.44 \pm 0.80) \times 10^{-6}$
162.0–199.0	$(9.39 \pm 0.18 \pm 0.36 \pm 0.25 \pm 1.0) \times 10^{-6}$

Data collected during the three periods with different zenith pointing criteria are combined. Kinetic energy is in GeV, flux in $(m^2\ sr\ s\ MeV)^{-1}$, ε_{stat} stands for the statistical error and $\varepsilon_{sys1,2,3}$ for the systematic errors.

cutoff effects, data collected in equatorial regions where the cutoff is high were excluded from the fit. The results obtained on the three different attitude samples were the same within the errors. The combined fit yields:

$$\gamma = 2.740 \pm 0.010(\text{stat}) \pm 0.016(\text{sys})\ ,$$

$$\Phi_0 = 2.52 \pm 0.09(\text{stat}) \pm 0.13(\text{sys}) \pm 0.14(\gamma)\ \frac{\text{GV}^{2.74}}{\text{m}^2\ \text{s sr MV}}\ .$$

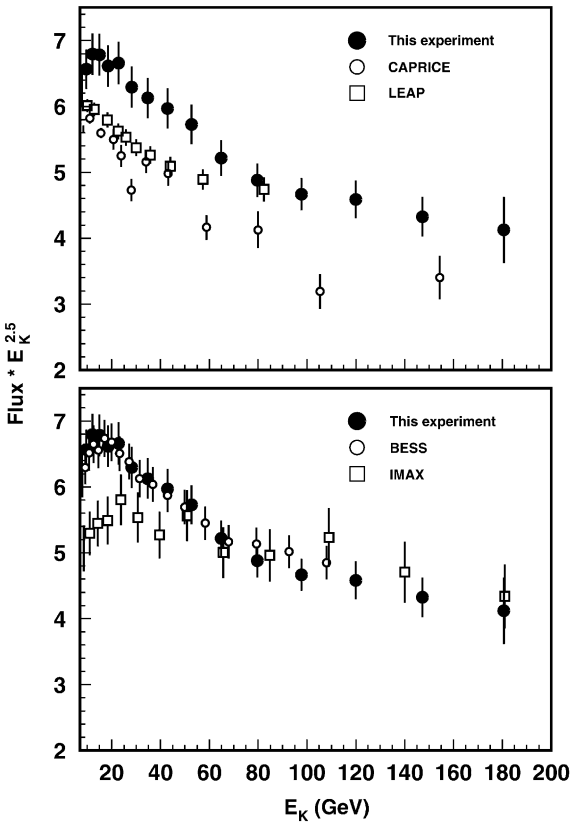

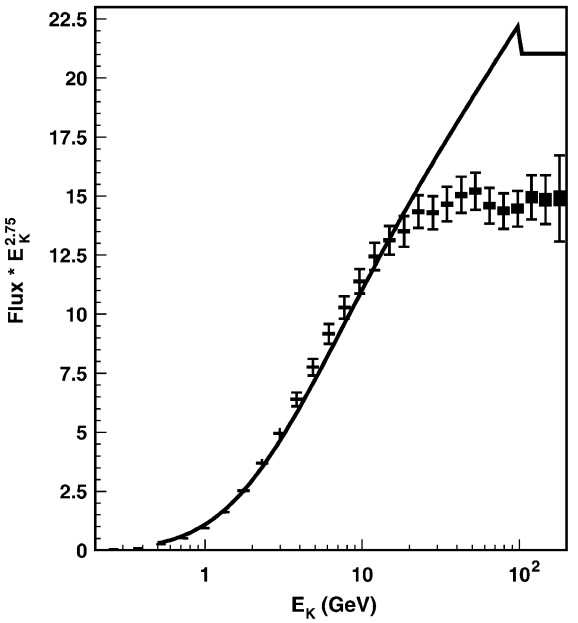

Fig. 4.13. The primary proton spectrum multiplied by $E_K^{2.5}$ in units of $GeV^{2.5}/(m^2\ s\ sr\ MeV)$ as measured by this experiment (total errors shown) in comparison with some recent balloon based measurements: CAPRICE [23], LEAP [21], BESS [53], IMAX [54].

Fig. 4.14. The primary proton flux multiplied by $E_K^{2.75}$ in units of $GeV^{2.75}/(m^2\ s\ sr\ MeV)$. The solid rectangles indicate the statistical errors, the error bars indicate the total error. The solid line is the flux used to calculate atmospheric neutrinos [31].

The systematic uncertainty in γ was estimated from the uncertainty in the track resolution (0.013) and the variation of the selection criteria (0.008). The third uncertainty quoted for Φ_0 reflects the systematic uncertainty in γ.

Fig. 4.17a shows the primary lepton spectra. Fig. 4.17b shows the energy dependence of the positron fraction, which exhibits the predominance of electrons over positrons in primary cosmic rays, as expected. Also shown are some recent previous measurements [33] in comparison with a model description [36]. The spectra are in reasonable agreement with previous measurements [33] as seen from Fig. 4.18, the difference below 10 GeV may be due to different solar modulation conditions.

4.4. Second spectrum

As shown in Figs. 4.9a–f, 4.10, 4.19 and 4.20, substantial second spectra are observed for downward and upward going protons and leptons at all geomagnetic latitudes below the geomagnetic

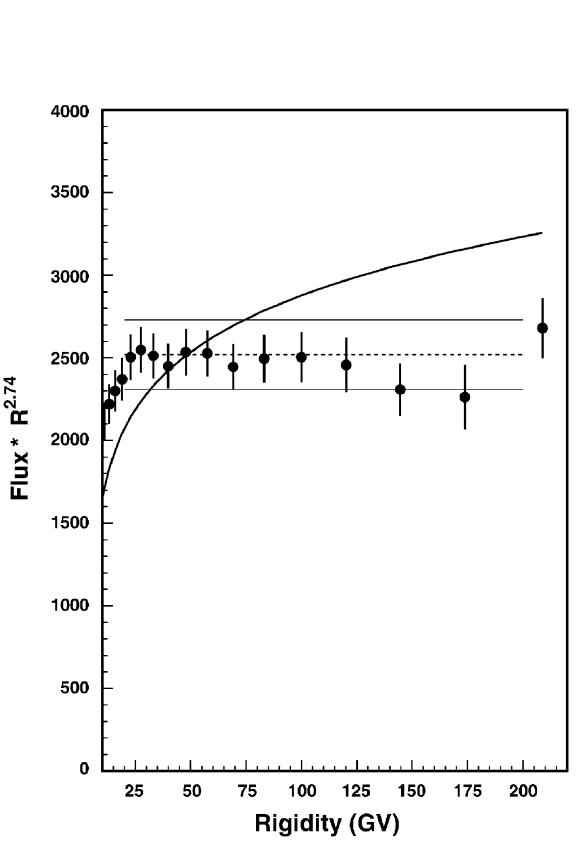

Fig. 4.15. Primary helium flux spectrum multiplied by $R^{2.74}$ in units of $m^{-2}\ s^{-1}\ sr^{-1}(GeV/A)^{1.74}$. The smooth line shows the spectrum used for atmospheric neutrino spectrum calculations [31].

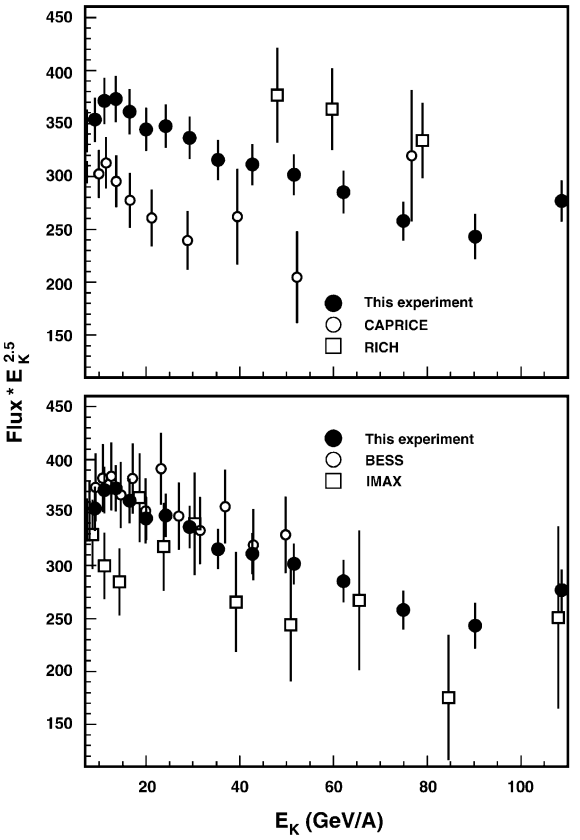

Fig. 4.16. The primary helium flux spectrum multiplied by $E_K^{2.5}$ in units of $m^{-2}\ s^{-1}\ sr^{-1}(GeV/A)^{1.5}$ in comparison with recent measurements: CAPRICE [23], RICH [28], BESS [53], IMAX [54].

cutoff. These spectra have the following properties:

(i) At geomagnetic equatorial latitudes, $|\Theta_M| < 0.2$, the proton spectrum extends from the lowest measured energy, 0.1 GeV, to ~ 6 GeV with a proton flux $\sim 70(m^2\ s\ sr)^{-1}$.

(ii) As seen in Figs. 4.9a and d, the second spectrum has a distinct structure near the geomagnetic equator: a change in geomagnetic latitude from 0 to 0.3 causes the proton flux to drop by a factor of 2–3 depending on the energy. Over the much wider interval $0.3 < |\Theta_M| < 0.8$, shown in Figs. 4.9b and e, the proton flux is nearly constant.

(iii) In the range $0 \leqslant |\Theta_M| < 0.8$, detailed comparison in different latitude bands (Figs. 4.19 and 4.20) indicates that the upward and downward fluxes of both protons and leptons are nearly identical, agreeing to within 1%.

(iv) At polar latitudes, $|\Theta_M| > 1.0$, the downward second spectrum of protons and electrons (Figs. 4.9c and 4.20) is gradually obscured by the primary spectrum, whereas the second spectrum of upward going protons and electrons (Figs. 4.9f and 4.20) is clearly observed.

Table 4.9
Differential primary helium flux in units of $(m^2\ s\ sr\ GV)^{-1}$ versus rigidity, R, in GV

R	Flux	R	Flux
0.76–0.91	(32 ± 16)	12.02–14.45	$(18.9 \pm 1.0) \times 10^{-1}$
0.91–1.10	48.9 ± 2.9	14.45–17.38	$(119.0 \pm 6.4) \times 10^{-2}$
1.10–1.32	58.4 ± 3.2	17.38–20.89	$(73.7 \pm 4.0) \times 10^{-2}$
1.32–1.58	62.8 ± 3.4	20.89–25.12	$(47.0 \pm 2.6) \times 10^{-2}$
1.58–1.91	63.9 ± 3.5	25.12–30.20	$(28.9 \pm 1.6) \times 10^{-2}$
1.91–2.29	58.2 ± 3.2	30.20–36.31	$(172.0 \pm 9.4) \times 10^{-3}$
2.29–2.75	49.4 ± 2.7	36.31–43.65	$(101.0 \pm 5.6) \times 10^{-3}$
2.75–3.31	39.6 ± 2.1	43.65–52.48	$(63.2 \pm 3.5) \times 10^{-3}$
3.31–3.98	30.8 ± 1.7	52.48–63.10	$(38.0 \pm 2.1) \times 10^{-3}$
3.98–4.79	22.6 ± 1.2	63.10–75.86	$(22.2 \pm 1.2) \times 10^{-3}$
4.79–5.75	$(159.0 \pm 8.6) \times 10^{-1}$	75.86–91.20	$(137.0 \pm 8.0) \times 10^{-4}$
5.75–6.92	$(110.0 \pm 5.9) \times 10^{-1}$	91.20–109.65	$(82.9 \pm 5.0) \times 10^{-4}$
6.92–8.32	$(72.8 \pm 3.9) \times 10^{-1}$	109.65–131.83	$(49.1 \pm 3.3) \times 10^{-4}$
8.32–10.00	$(47.1 \pm 2.5) \times 10^{-1}$	131.83–158.49	$(27.8 \pm 1.9) \times 10^{-4}$
10.00–12.02	$(29.9 \pm 1.6) \times 10^{-1}$	158.49–190.55	$(16.5 \pm 1.4) \times 10^{-4}$
		190.55–229.09	$(118.0 \pm 8.0) \times 10^{-5}$

The errors quoted are the combination in quadrature of the statistical and systematic errors.

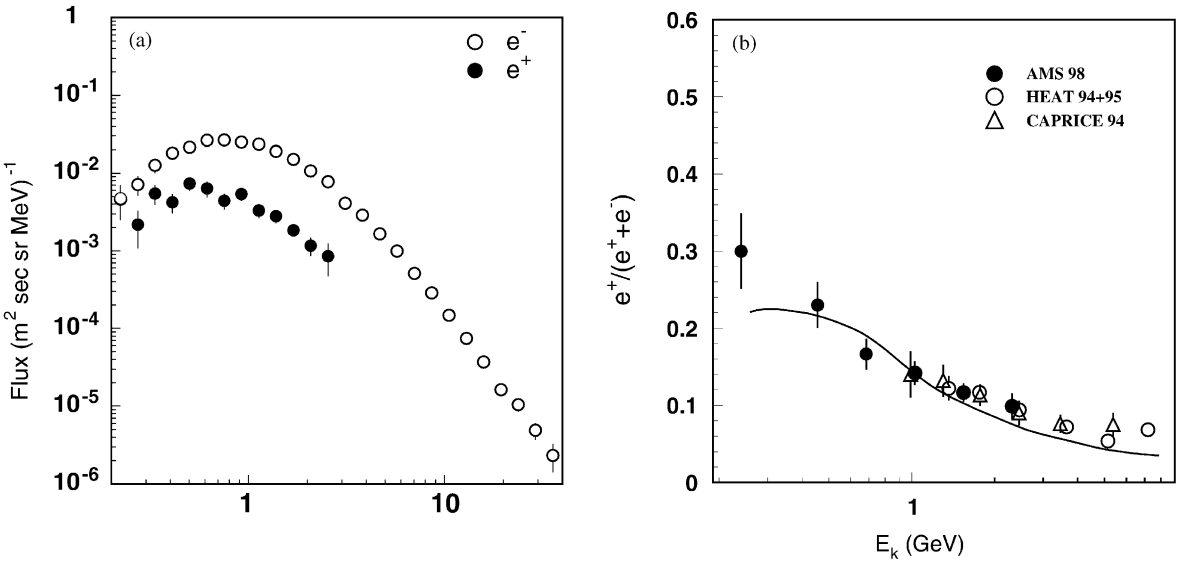

Fig. 4.17. (a) Flux spectra for primary leptons. Particle direction within 25° of zenith. (b) Positron fraction for primary leptons versus energy. AMS data are compared with balloon experiments [33] and with a model description [36] (solid line).

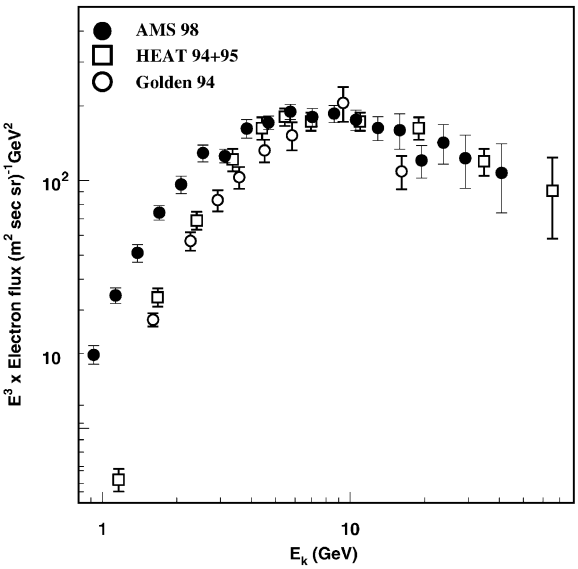

Fig. 4.18. AMS electron primary spectrum data in comparison with the earlier measurements.

(v) As seen from Fig. 4.21 the lepton fluxes also reach a maximum at the geomagnetic equator. With increasing latitude the positron flux drops off faster than the electron flux.

As was mentioned in the introduction the under-cutoff particles were earlier detected by balloon experiments. Balloon-based measurements were performed at ~ 40 km from the Earth's surface, i.e. under $\sim 5g/\mathrm{cm}^2$. This environment lead to a specific terminology adapted to those observations [56]:

- A large fraction of downward going particles produced in the air above the detector was called *atmospheric secondaries*. This was actually the main background source with a particular altitude dependence.
- Upward going particles were called *splash albedo*. Their intensity is only weakly altitude dependent.
- The fraction of splash albedo leaving the Earth and then leading back to the Earth at the opposite hemisphere was called *return albedo*.

Satellite experiments discovered *trapped* radiation or *radiation belts* above $\sim$1000 km. The term *trapped radiation* had been introduced much earlier [57].

For the under-cutoff particles observed by AMS we use the term *second spectrum*[13] to distinguish from:

- *Atmospheric secondaries*, which are not produced without atmosphere;
- *Splash albedo*, since AMS is too far from the atmosphere to observe them;

[13] Some authors [58] propose to use the term "cosmic ray albedo" instead. However it is too general, for example, the radiation belts also fall into this category since they seem to originate from neutron albedo.

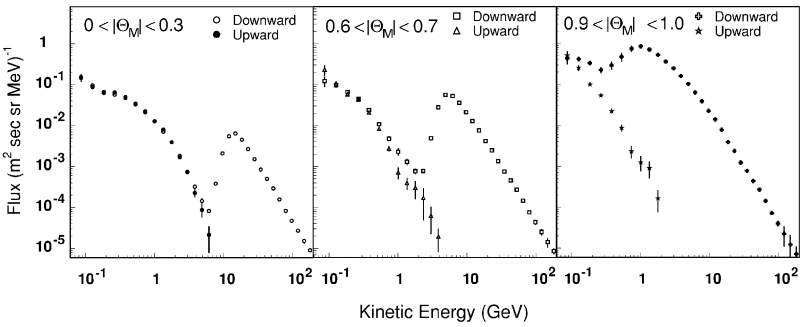

Fig. 4.19. Comparison of upward and downward second spectrum protons at different geomagnetic latitudes. As seen, below cutoff, the upward and downward fluxes agree in the range $0 \leqslant |\Theta_M| < 0.8$ (see also Figs. 4.9b and e).

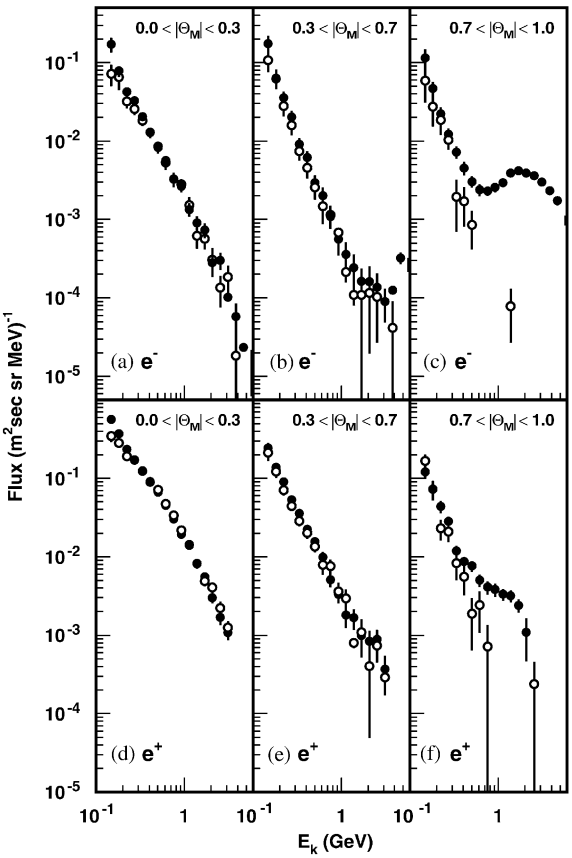

Fig. 4.20. (a–c) Flux spectra for downward (full circles) and upward (open circles) going electrons and (d–f) positrons, separated according to the geomagnetic latitude, Θ_M, at which they were detected.

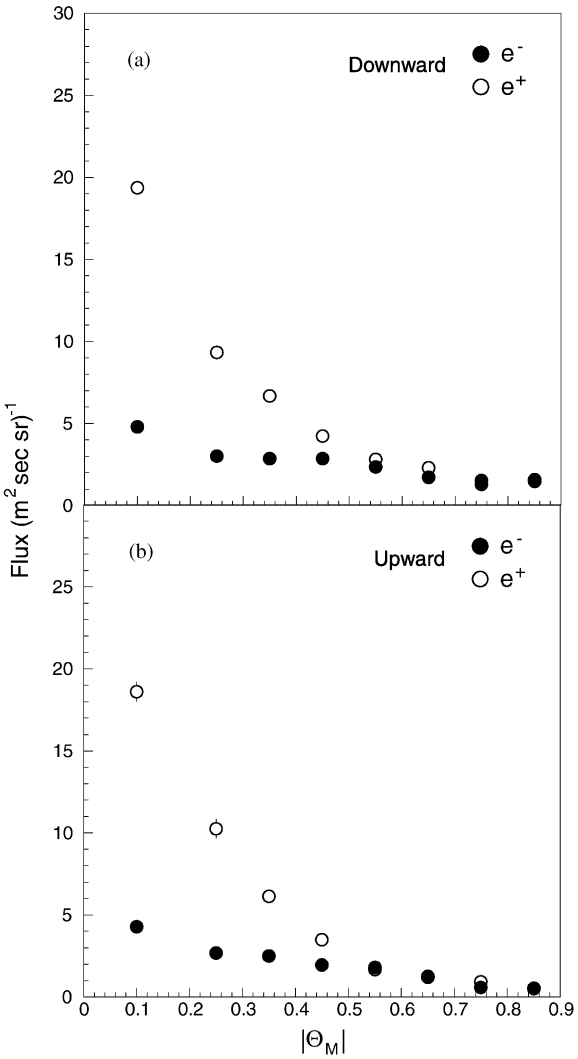

Fig. 4.21. Properties of second lepton spectra flux: (a) downward and (b) upward going electrons and positrons as functions of the geomagnetic latitude, Θ_M, at which they were detected integrated over the range 0.2–2.5 GeV.

- *Return albedo*, since it may only be a small fraction of the second spectrum flux as will be seen in what follows;
- *Trapped* particles, since AMS was flying below the radiation belts.

In Fig. 4.22 we compare the AMS lepton (electron plus positron) flux with the best data on "reentrant and splash albedo" available from various balloon flights [19,34,59].

In addition to the backward tracing mentioned above the leptons were also traced forward until their trajectory would have either escaped or crossed the top of the atmosphere, the location of which was taken as the particle sink. All second spectrum particles were found to originate in and

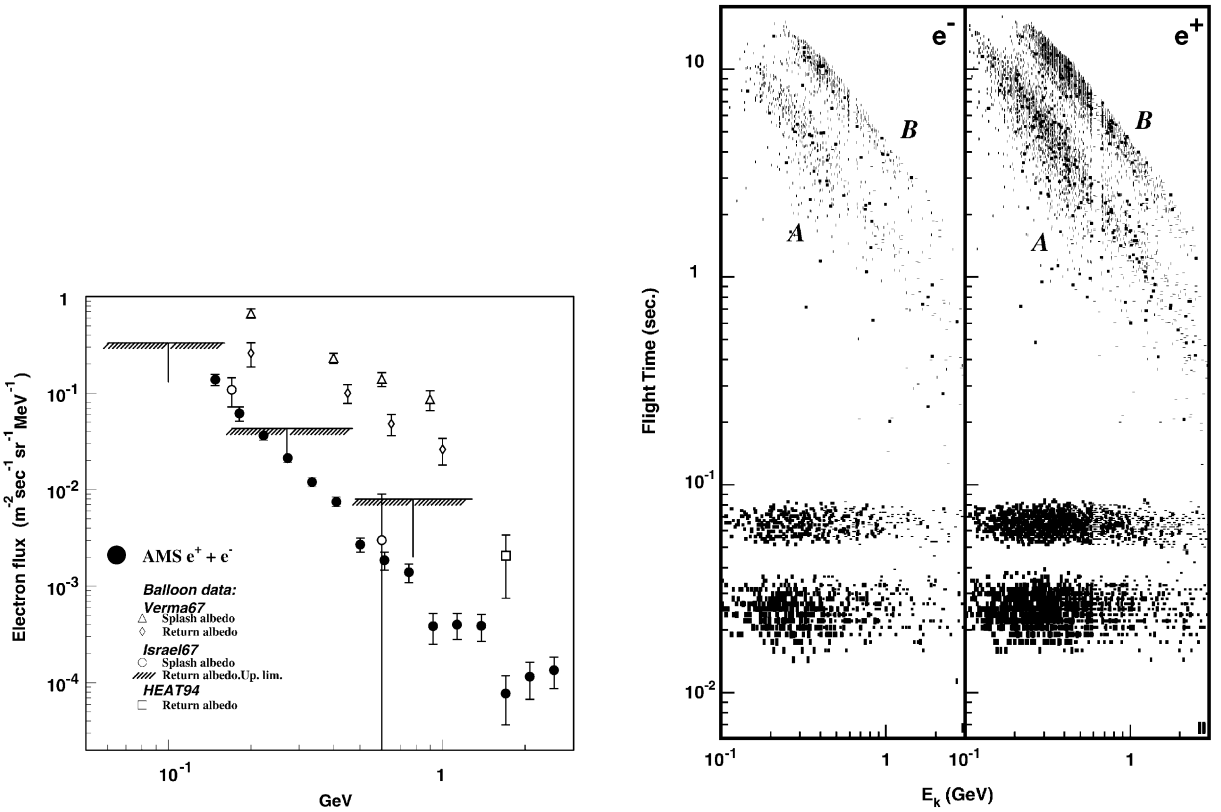

Fig. 4.22. AMS second spectrum. $e^+ + e^-$ combined data at $0.6 < |\Theta_M| < 0.7$ in comparison with the reentrant and splash albedo measurements by balloons: Verma67 [19], Israel67 [59], HEAT94 [34].

Fig. 4.23. The flight time versus energy from the tracing of leptons detected in the region $|\Theta_M| < 0.7$. From the flight time distribution there are two distinct types of trajectories: For "short-lived", flight times < 0.2 s, the flight time is independent of lepton energy. For "long-lived", flight times $\geqslant 0.2$ s, there are two bands A and B. In both A and B the flight time depends on energy: it decreases with increasing energy.

eventually re-enter the atmosphere, except for a few percent of the protons detected near the South Atlantic Anomaly (SAA). These had closed trajectories and hence may have been circulating for a very long time and it was difficult to trace back to their origin. This type of trajectory was only observed near the SAA, clearly influenced by the inner radiation belt (this was one of the reasons why data taken in the SAA region were excluded). Defining the flight time as the sum of forward and backward tracing times, that is the interval between origin and sink, Fig. 4.23 shows the distribution of energy versus flight time for electrons and positrons. Both e^+ and e^- exhibit two distinct types of trajectories:

- The horizontal bands with flight times < 0.2 s, defined as "short-lived".
- The diagonal bands with flight times $\geqslant 0.2$ s defined as "long-lived".

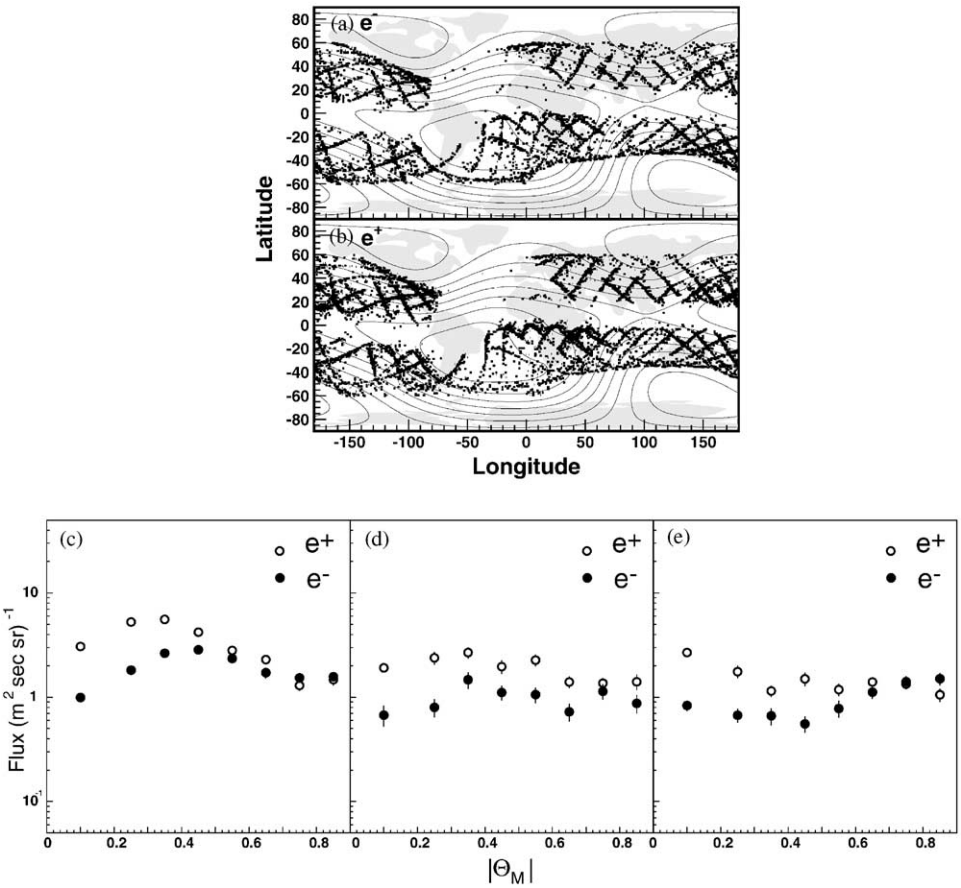

Fig. 4.24. Properties of short-lived second spectra leptons (< 3 GeV): (a) The geographic origin of electrons and (b) positrons. Note that the point of origin shows no longitudinal dependence and that the short-lived leptons do not originate from the region $|\Theta_M| < 0.4$. The lines indicate the geomagnetic field contours at 380 km. (c) The e^- (full circles) and e^+ (open circles) fluxes integrated over the range 0.2–2.5 GeV as a function of magnetic latitude for zenith, (d) 20° and (e) 25° shuttle attitude.

For $|\Theta_M| < 0.3$, most (75% of e^+, 65% of e^-) leptons are long-lived. The same two types of trajectories are also observed for protons and 70% of the second spectrum protons are long-lived.

4.4.1. Distinct properties of the second spectra for short-lived particles

The trajectory tracing shows that particles travel in cycles across the equator where the trajectories reach maximal altitude and they are reflected at the lowest points at the mid and polar latitudes. For short-lived particles:

- From Fig. 4.23 one sees that the flight time is independent of particle energy. For protons this is the total trajectory length which is independent of particle energy.

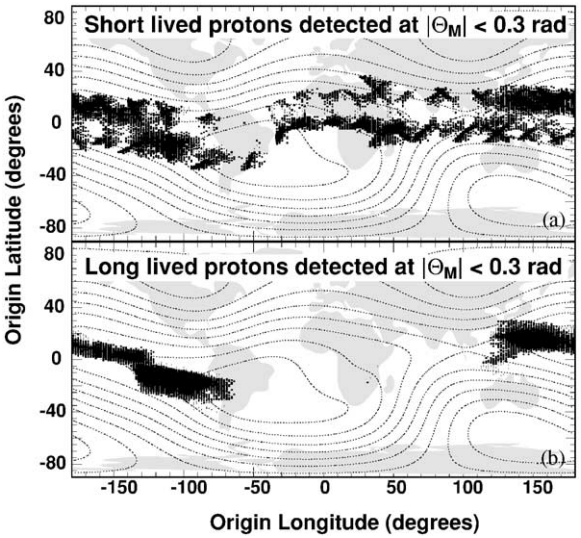

Fig. 4.25. The geographical origin of (a) short-lived and (b) long-lived protons with $p < 3\ \mathrm{GeV}/c$. The dashed lines indicate the geomagnetic field contours at 380 km.

- The point of origin shows no longitude dependence. They do not originate from near to the geomagnetic equator, $|\Theta_M| < 0.4$ (see Figs. 4.24a, b and 4.25a), the apparent structure reflecting the orbits of the space shuttle.
- The particle flux is independent of the shuttle attitude and is approximately isotropic (see Figs. 4.24c–e).

4.4.2. Distinct properties of the second spectra for long-lived particles

- As shown in Figs. 4.25b and 4.26 long-lived e^-, e^+ and protons originate from well defined, complementary geographic regions. Tracing also shows that the regions of origin for positrons coincide with regions of sink for electrons and vice versa.
- Figs. 4.27 and 4.28 show the strongly peaked distributions of the point of origin of the long-lived particles in geomagnetic coordinates. Within the regions indicated the distributions are strongly peaked and the two diagonal bands (A, B) seen in Fig. 4.23 for the long-lived leptons correspond to the two regions of origin (A, B) marked in Figs. 4.26 and 4.27.
- The long-lived particles are reflected across the equator hundreds of times. The number of cycles they can make before being absorbed in the atmosphere decreases with increasing energy.
- As shown in Fig. 4.26c–e, the long-lived lepton flux reaches a maximum in the equatorial region where they are produced and absorbed.
- At zenith shuttle orientation, 99% of the long-lived leptons are actually detected at $|\Theta_M| < 0.4$, indicating a strongly anisotropic angular distribution.

Though data is presented only for particles detected at $|\Theta_M| < 0.3$, these general features hold true up to $|\Theta_M| \sim 0.7$.

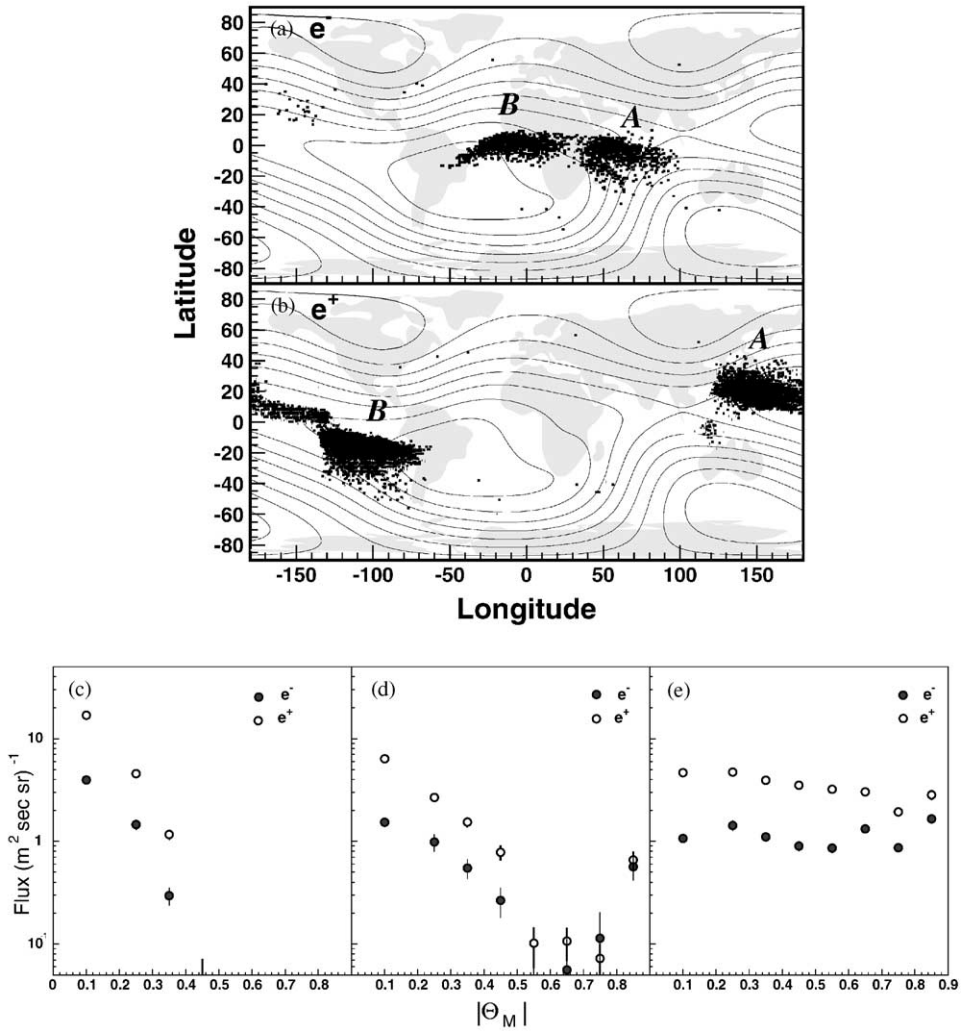

Fig. 4.26. Properties of long-lived second spectra leptons (< 3 GeV): (a) the geographical origin of electrons and (b) positrons. The lines indicate the geomagnetic field contours at 380 km. The regions *A* and *B* correspond to the bands *A* and *B* marked in Fig. 4.23. (c) The e^- (full circles) and e^+ (open circles) fluxes integrated over the range 0.2–2.5 GeV as a function of magnetic latitude for zenith, (d) 20° and (e) 45° shuttle attitude.

Fig. 4.29 shows the distribution of the number of geomagnetic equator crossings for long-lived and short-lived protons. About 15% of all the second spectrum protons were detected on their first bounce over the geomagnetic equator.

4.4.3. Lepton charge ratio

An interesting feature of the observed second lepton spectra is the predominance of positrons over electrons. In Table 4.10 the e^+/e^- ratios grouped according to magnetic latitude region and shuttle attitude (0°, 20°, 45°, 180°) are given separately for long-lived and short-lived leptons.

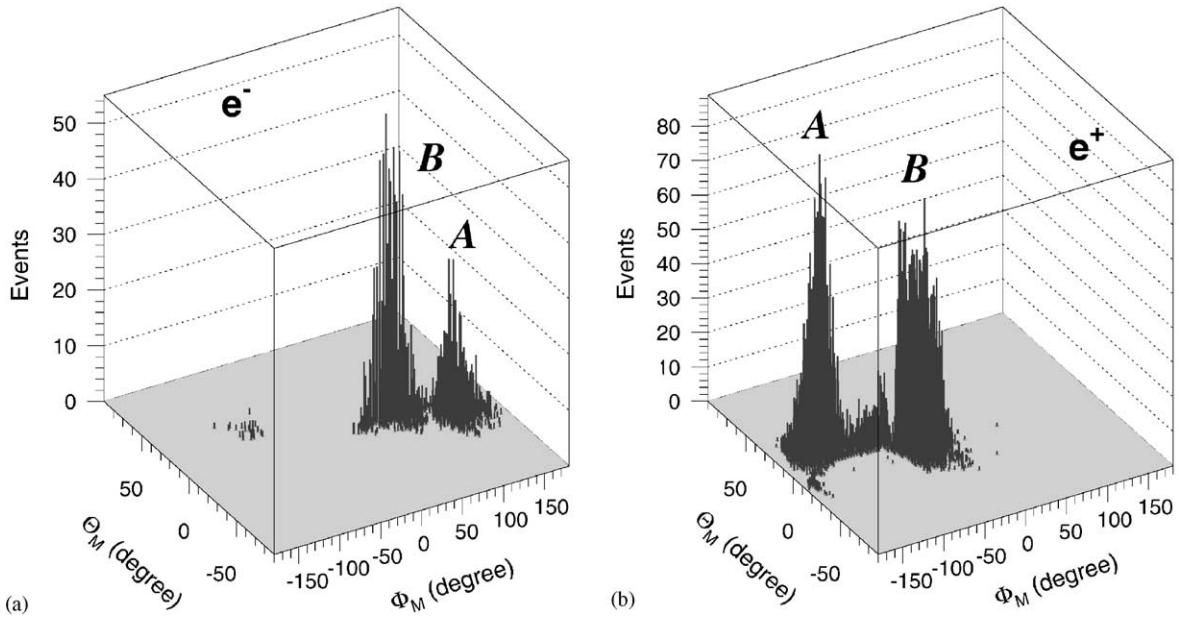

Fig. 4.27. Property of second spectra: the point of origin of long-lived leptons with energies < 3 GeV and $|\Theta_M| < 0.7$ in geomagnetic coordinates. The regions A and B correspond to those in Fig. 4.26 and the bands marked A and B in Fig. 4.23.

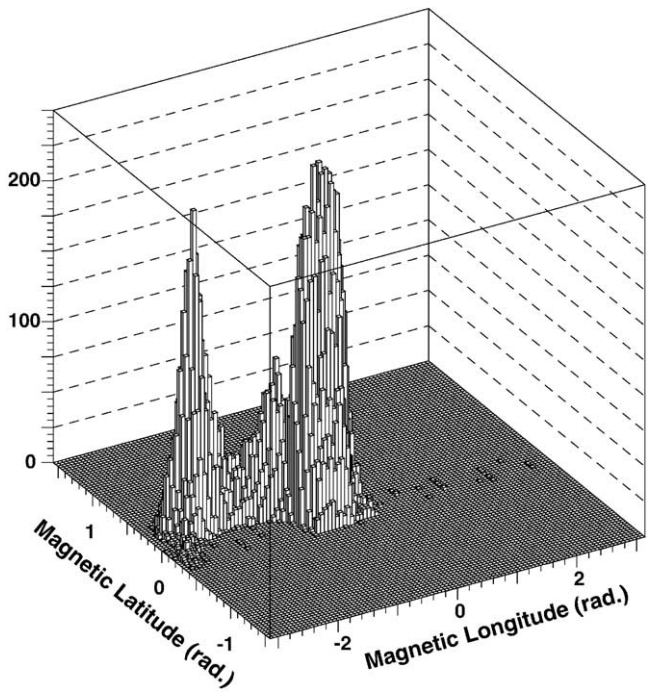

Fig. 4.28. The point of origin of long-lived protons ($|\Theta_M| < 0.3$, $p < 3$ GeV/c) in geomagnetic coordinates.

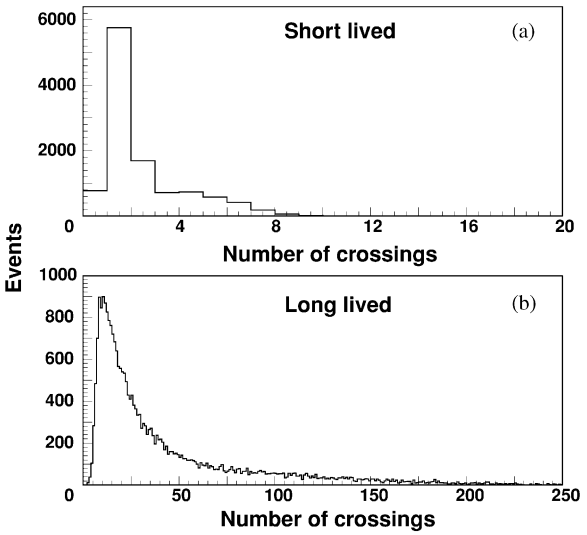

Fig. 4.29. Number of times the back traced trajectory crosses the geomagnetic equator for (a) short-lived and (b) long-lived protons ($|\Theta_M| < 0.3$, $p < 3$ GeV/c).

As seen from Table 4.10:

- The ratio depends at most weakly on the shuttle orientation.
- The ratios for short- and long-lived leptons behave differently. For short-lived leptons the e^+/e^- ratio is maximal at the magnetic equator where it reaches a value of ~ 3 whereas for long-lived leptons the ratio is higher, $\gtrsim 4$ at the magnetic equator, and less dependent on latitude.
- The energy dependence of the e^+/e^- ratio for 0° attitude and $|\Theta_M| < 0.3$ is shown in Fig. 4.30. As seen, short-lived and long-lived leptons behave differently. For short-lived leptons the ratio does not depend on the particle energy in the range 0.2–3 GeV but for long-lived leptons the ratio does depend on the lepton energy, reaching a maximum value of ~ 5.

The combined (short- and long-lived, all attitudes) dependence on $|\Theta_M|$ of the ratio for all second spectra particles is shown in Fig. 4.31.

4.4.4. Analysis of the helium second spectrum

As shown in Fig. 4.11, a second spectrum is observed for $|\Theta_M| < 0.8$. This spectrum extends from the lowest measured rigidity, 0.8 GV, up to 3 GV with an integrated flux of $\sim 10^{-3}(m^2\ s\ sr)^{-1}$.

To ensure these events are not due to resolution effects at low energies or to contamination from single scattering inside the detector, more stringent reconstruction criteria were applied in the examination of the second spectrum. $|Z| = 1$ events with a wrongly reconstructed charge magnitude were reduced by an additional factor 10^{-2} by requiring both the time of flight and tracker charge magnitude determinations to be $|Z| = 2$. Tails in the velocity reconstruction were reduced by requiring at least three matched hits in the four time of flight planes. In this energy range, the accuracy of the velocity measurement is 2.4%. Any large angle scattering in a tracker plane was identified

Table 4.10
Lepton charge ratio versus magnetic latitude for the shuttle attitudes 0°, 20°, 45° and 180° for long-lived and short-lived particles

e^+/e^-	Long-lived (flight time $\geqslant 0.2$ s)				
Attitude	$0.0 < \lvert\Theta_M\rvert < 0.2$	$0.2 < \lvert\Theta_M\rvert < 0.4$	$0.4 < \lvert\Theta_M\rvert < 0.6$	$0.6 < \lvert\Theta_M\rvert < 0.8$	$0.8 < \lvert\Theta_M\rvert < 1.0$
0°	4.27 ± 0.17	3.26 ± 0.37	1.65 ± 1.24		
20°	4.15 ± 0.39	2.75 ± 0.45	2.92 ± 1.00	1.05 ± 0.69	1.46 ± 0.42
45°	4.36 ± 0.40	3.41 ± 0.30	3.81 ± 0.33	2.27 ± 0.18	1.28 ± 0.16
180°	4.27 ± 0.25	4.25 ± 0.65			
e^+/e^-	Short-lived (flight time < 0.2 s)				
Attitude	$0.0 < \lvert\Theta_M\rvert < 0.2$	$0.2 < \lvert\Theta_M\rvert < 0.4$	$0.4 < \lvert\Theta_M\rvert < 0.6$	$0.6 < \lvert\Theta_M\rvert < 0.8$	$0.8 < \lvert\Theta_M\rvert < 1.0$
0°	3.08 ± 0.35	2.43 ± 0.19	1.35 ± 0.11	1.10 ± 0.11	0.83 ± 0.10
20°	2.83 ± 0.67	2.23 ± 0.37	1.95 ± 0.28	1.48 ± 0.22	0.94 ± 0.18
45°	3.22 ± 0.44	2.18 ± 0.32	2.01 ± 0.32	1.08 ± 0.12	0.93 ± 0.19
180°	4.84 ± 0.81	2.79 ± 0.28	1.45 ± 0.18	1.17 ± 0.21	0.68 ± 0.27

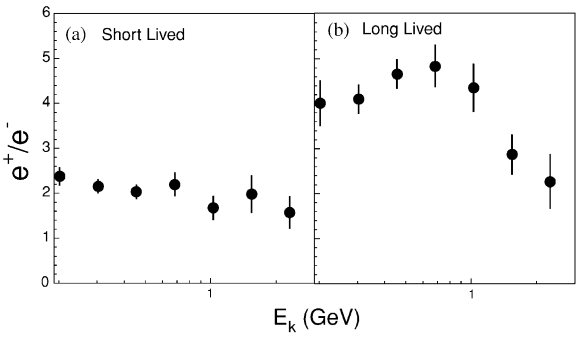

Fig. 4.30. Property of second spectra: the e^+/e^- ratio as a function of energy for (a) short-lived and (b) long-lived particles. Shuttle attitude 0° and $|\Theta_M| < 0.3$.

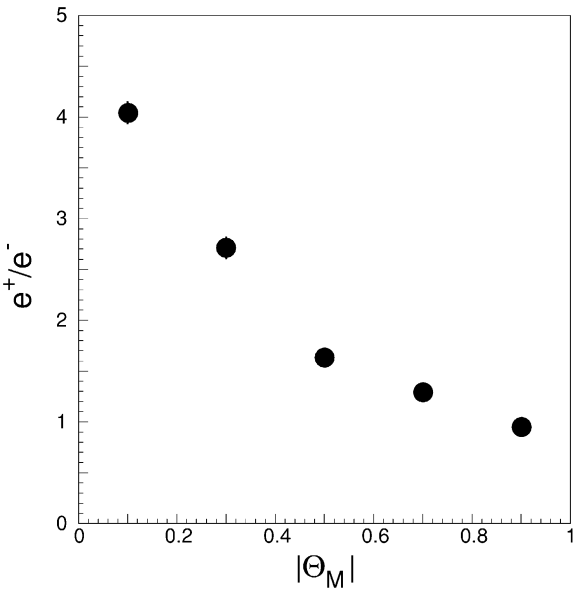

Fig. 4.31. Property of second spectra: the e^+/e^- ratio as a function of magnetic latitude integrated over the range 0.2–2.5 GeV and combined for short-lived and long-lived leptons independent of shuttle attitude.

and removed by demanding that the particle was also measured by the tracker in the non-bending projection and by requiring agreement between the rigidity measured with the first three hits along the track, with the last three hits and with all the hits. Events with collinear delta rays, which create additional energy depositions in the tracker planes along the trajectory of the particle, were identified

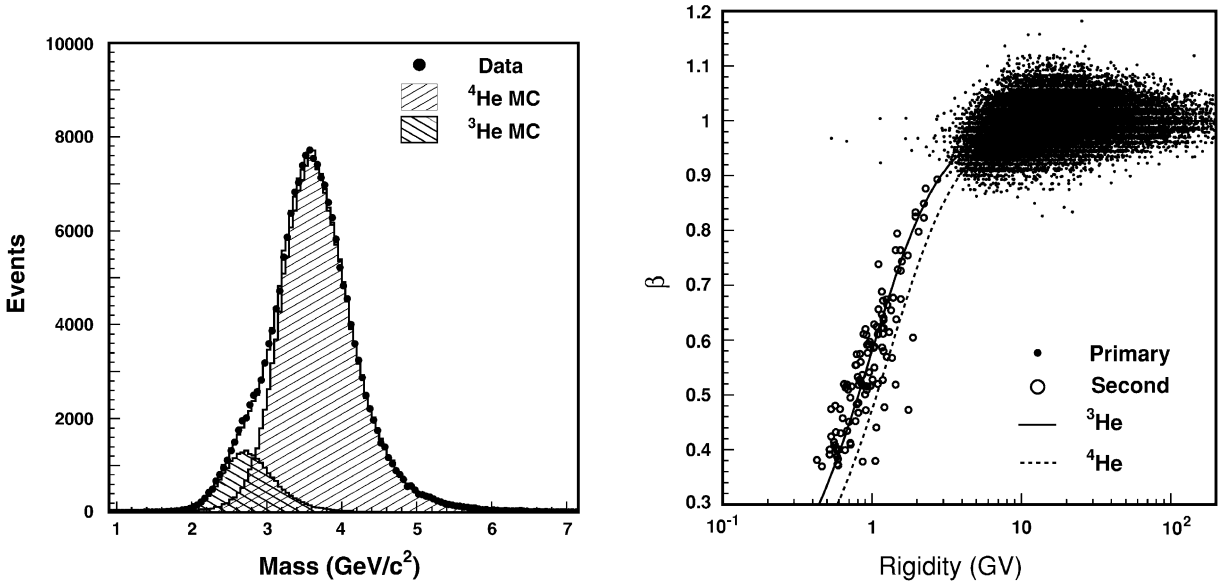

Fig. 4.32. Mass distribution for helium events above geomagnetic cutoff for $|\Theta_M| > 0.9$ and $\beta < 0.9$. Dots are data. Histogram is a Monte Carlo simulation with 11.5% ^{3}He.

Fig. 4.33. Correlation between rigidity and velocity for helium events detected at $|\Theta_M| < 0.6$. Dots denote events from the primary spectrum, and open circles those from under cutoff. Solid (dashed) line corresponds to the ^{3}He (^{4}He) mass hypothesis.

and rejected by an isolation criteria which demands a minimum amount of energy observed within 10 mm of the track. Finally, extrapolation of the fit track was required to match the locations of the scintillator hits within 60 mm.

These criteria were applied to the data samples from three data collection periods corresponding to 0°, 20° and 45° shuttle attitudes. Compared to the looser cuts used in the analysis of the differential rigidity spectrum, the selection efficiency is ~65% up to 3 GV. The average mass resolution for helium nuclei in the kinetic energy range 0.1–1.2 GeV/nucleon (i.e. $\beta < 0.9$) is ~12%. Fig. 4.32 shows the reconstructed mass distribution for events above cutoff at $|\Theta_M| > 0.9$ in this energy range. As shown, the data are in agreement with a Monte Carlo simulation which contains 11.5% ^{3}He.

Fig. 4.33 shows the correlation between rigidity, R, and velocity, β, for events with $|\Theta_M| < 0.6$, together with the expectations for ^{3}He and ^{4}He nuclei. Primary spectrum events are clustered at $\beta > 0.9$ with rigidities in the range of 3–200 GV. A population of 115 events with rigidities below the local geomagnetic cutoff are marked in the figure with open circles. As seen, this population follows the ^{3}He mass line. Fig. 4.34 shows the scatter of rigidity versus Θ_M for events with $\beta < 0.9$. The two symmetric clusters at $|\Theta_M| > 0.6$ correspond to nuclei from the primary helium spectrum. The same 115 events marked in Fig. 4.33 form a clear and isolated low energy band ($R < 3$ GV). This second population has the following properties:

- The reconstructed mass distribution is shown in Fig. 4.35. As seen, most of the events are consistent with ^{3}He. At the 90% confidence level the fraction of ^{3}He exceeds 0.9.

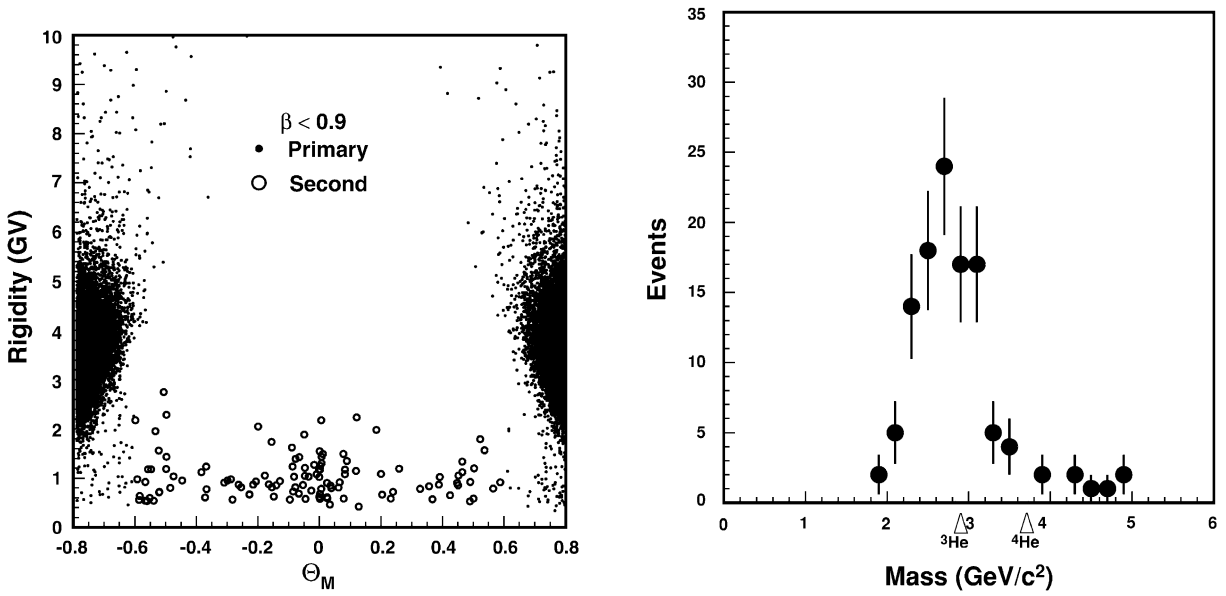

Fig. 4.34. Rigidity versus Θ_M for events with $\beta < 0.9$. Dots and open circles as in Fig. 4.33.

Fig. 4.35. Reconstructed mass distribution for the second spectrum helium for $|\Theta_M| < 0.6$ compared with the masses of ^{3}He and ^{4}He.

- As shown in Fig. 4.36, their spectrum extends from the lowest measured energy, 0.1 GeV/nucleon, up to ~1.2 GeV/nucleon, yielding an average flux of $(6.3 \pm 0.9) \times 10^{-3}(\mathrm{m}^2\ \mathrm{s\ sr})^{-1}$.
- As shown in Fig. 4.37, the flux reaches its maximum at the geomagnetic equator.
- Within statistics, there is no preferred direction and the fluxes measured separately with data from the three periods corresponding to 0°, 20° and 45° shuttle attitudes are equal.

To understand the origin of these events, the trajectories have been traced both backward and forward from their incident angle, location and momentum through the Earth's magnetic field, following the same procedure as described in [37,40]. All events were found to originate in the atmosphere. Analysis of the sum of their forward and backward flight times again yields two distinct classes: "short-lived" and "long-lived" for flight times below and above 0.3 s respectively.

The origin of the "short-lived" helium nuclei are distributed uniformly around the globe whereas the "long-lived" particles originate from a geographically restricted region as is shown in Fig. 4.38. This region matches that from which the second proton flux and second positron flux originate [37,40]. Within the statistics, ^{3}He is equally predominate in events from both the "short-" and "long-lived" classes. We recall that the abundance of ^{3}He at much lower energies, ~50 MeV, and far away from Earth (L shell above 6) was reported in Ref. [60]. Geomagnetically trapped low energy light isotopes have been studied with satellites [61].

4.4.5. Simulation analysis of the second spectrum

After the AMS data had become available, many physicists [62–67] have made detailed Monte Carlo simulations of the second spectrum phenomenon by means of several independent methods.

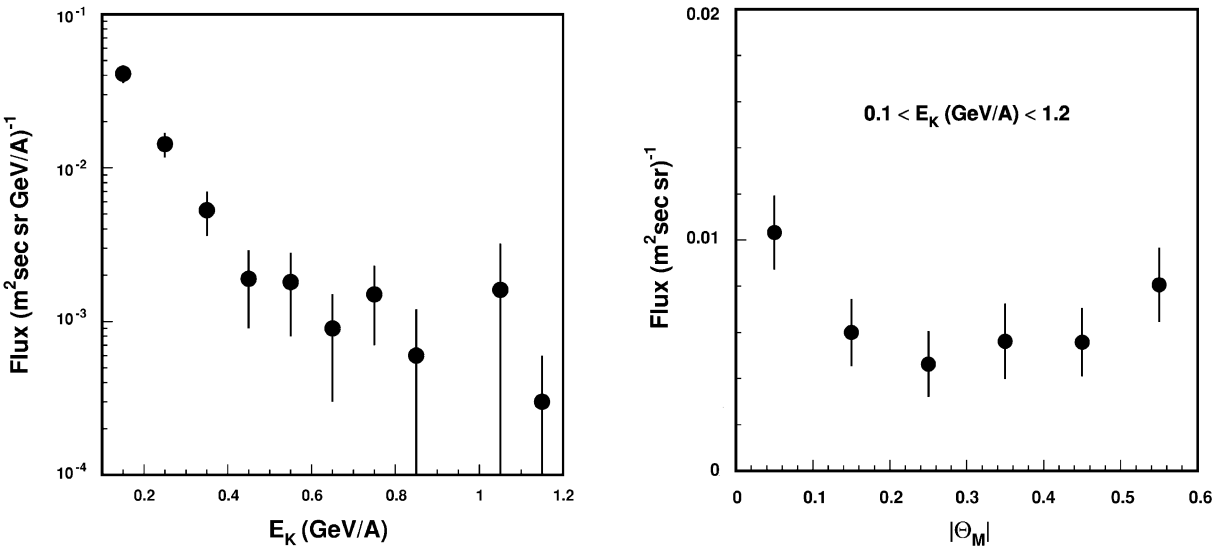

Fig. 4.36. Second helium flux spectra for $|\Theta_M| < 0.6$.

Fig. 4.37. Average flux of the second helium spectrum versus geomagnetic latitude.

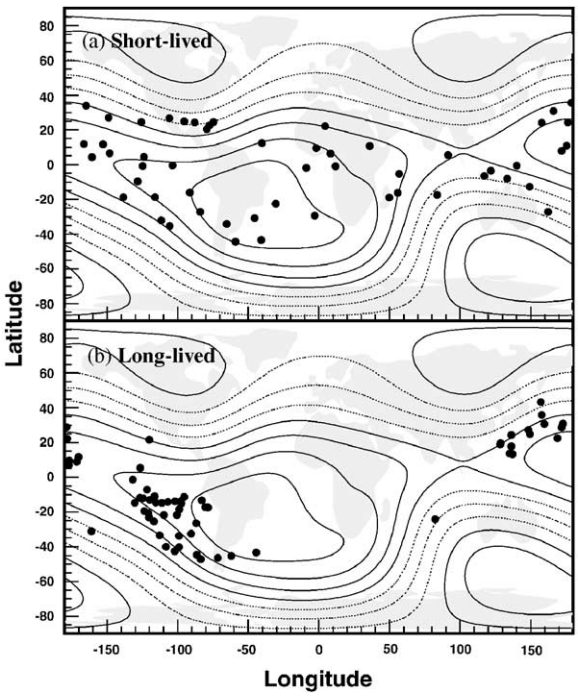

Fig. 4.38. Geographical origin of (a) "short-lived" and (b) "long-lived" helium in the second spectrum. The lines indicate the geomagnetic field contours at 380 km.

The methods included the primary proton and helium nucleon interactions in the atmosphere with tracing all trajectories in the Earth's magnetic field. The simulations have successfully described the AMS second spectrum data on protons, electrons and positrons [66] including the absolute flux values as well as latitude dependence and absolute value of the e^+/e^- ratio. Thus many features like the shape of the second spectrum and the geographic area of the long lived component origin were understood to be consequences of the cosmic ray interaction with the atmosphere [62,66] and manifestations of the Earth's magnetic field [65].

4.5. Antiproton analysis

The measurement of low energy, below 1 GeV, antiprotons was long considered to be a sensitive test for the presence of exotic antiproton sources in cosmic rays like dark matter neutralino annihilations [68]. Conventional sources predicted a relatively low flux of antiprotons below 1 GeV whereas the signal expected from neutralino annihilations was relatively high at these energies. However, as was recently demonstrated [4,69], the conventional sources contribute considerable antiproton flux at low energy if one takes into account proton–helium collisions, fermi motion effects and the so called "tertiary" antiproton component, i.e. the interactions of produced antiprotons. These effects turned out to be more important than previously assumed, and the consequence was that there had been little hope to isolate an "exotic" antiproton signal at low energies, since the uncertainty is dominated by the theoretical model describing conventional sources. Therefore, for the AMS precursor flight, the antiproton study has become to a great extent a test of the instrument to detect a small signal in the presence of a high background.

Antiproton candidates were selected by requiring the measured particle charge to be -1, particle velocity to be less than the speed of light and the particle measured momentum to be less than 5 GeV/c.

There were several identified backgrounds to the genuine antiproton signal:

(a) Proton events with the momentum measurement affected by a single or multiple scattering in the tracker. This background was suppressed by a cut on the χ^2 value obtained in fitting the particle trajectory and by requiring agreement for the rigidity and charge sign measured using all the hits in the tracker and separately in the first three hits and the last three hits along the track.
(b) Protons accompanied by secondary pions produced inside the AMS detector. To remove these events the "isolation" cut was applied, i.e. no additional hits both in either the tracker or scintillator counters should be found in the vicinity of the reconstructed trajectory.
(c) Electron events with the wrongly measured velocity. To suppress this background, only events with trajectory crossing the active Čerenkov area and therefore having an independent velocity measurement were accepted.

To ensure good quality of the mass measurements, only events with four independent time measurements in the scintillator counter and at least seven coordinate measurements, i.e. four in the bending and three in the non-bending plane, were accepted. After all cuts were applied the overall antiproton efficiency was 18%.

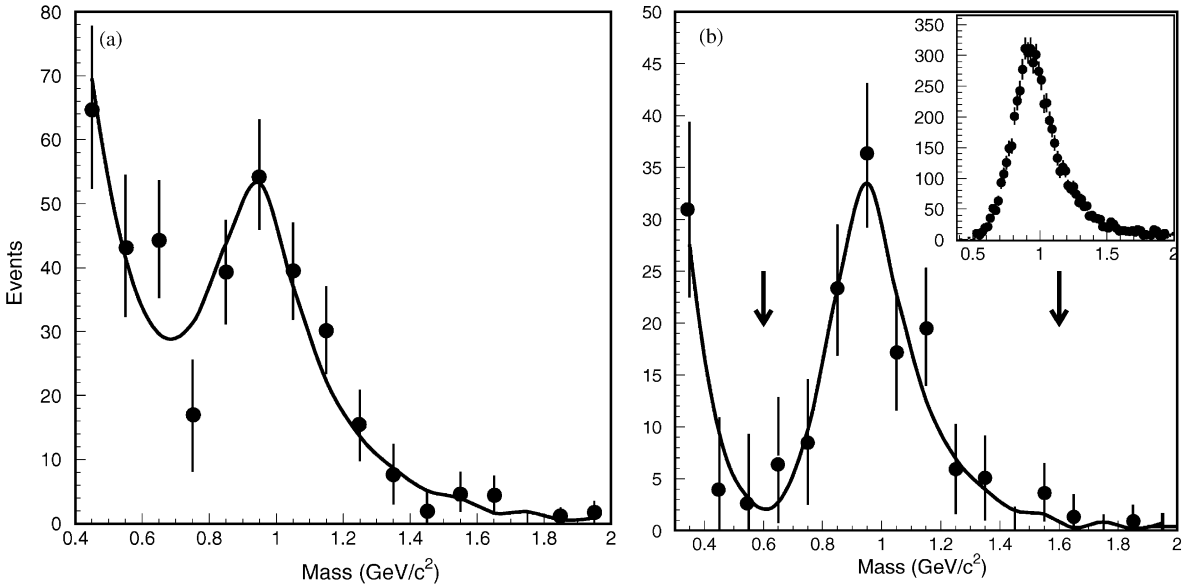

Fig. 4.39. The mass distribution of the antiproton candidates. Points are data, the line shows the fit to proton mass (insert) and polynomial background. (a) Total statistics 186 ± 28 events. (b) Primary antiprotons. The arrows indicate the cut values.

Fig. 4.39a shows the distribution of the reconstructed mass for these events. The antiproton peak is clearly seen to be well separated from the pion background which rises towards zero mass. After the background subtraction 186 ± 28 events were left.

For the antiproton primary spectrum the measured rigidity of the candidates was required to be higher than the local geomagnetic cutoff. The final mass distribution of the primary antiproton events is shown in Fig. 4.39b. Finally, the reconstructed particle mass was required to be compatible with the proton mass and the background was then reduced to less than 3 events.

Correcting the measured number of events for the AMS acceptance, selection efficiency, measurement time and unfolding the AMS energy resolution, the primary antiproton flux was obtained as function of kinetic energy. In Fig. 4.40 the flux is compared to the latest results of Ref. [70].

4.6. Deuteron spectrum measurement

Like antiprotons, the rare hydrogen isotopes in cosmic rays are of secondary origin, resulting mainly from the nuclear interactions of primary cosmic ray protons and ^{4}He with the interstellar medium. They provide important complementary information on the interstellar propagation of cosmic rays [71,72]. To date, deuterium spectrum measurements were made at energies $\leqslant 100$ MeV/nucleon [72–74], where solar modulation effects are still large and the anomalous He component complicates interpretation. There are also measurements at higher energy ($\geqslant 100$ MeV/nucleon) from balloon-borne experiments [75–78].

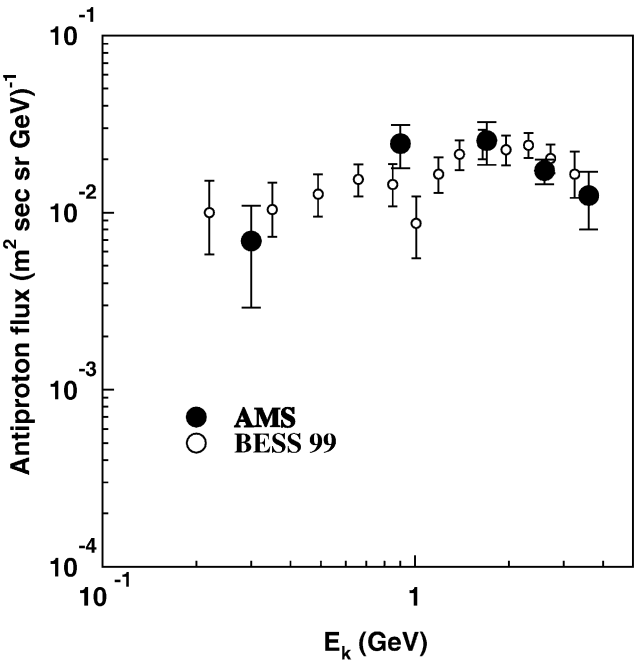

Fig. 4.40. The AMS antiproton flux measurement in comparison with BESS [70] data.

4.6.1. Data analysis

Deuteron candidates were specifically selected by requiring the measured particle charge to be $Z = 1$ and reconstructed mass compatible with the deuteron. The background to the deuteron signal originated mainly from two sources:

(i) $Z = 2$ particles with wrongly measured charge. In order to remove this background the consistency of the charge measurements was required from both the time of flight and the tracker. This source of background was consequently reduced to a negligible level ($< 10^{-5}$).

(ii) Proton events with wrongly reconstructed velocity and/or momentum. This background was reduced by applying the stringent selection criteria:

- At least three matched hits in the four time of flight planes were required thus reducing tails in the time of flight distribution.
- Tracks with single large scattering were removed through trajectory χ^2 cuts and by requiring the rigidity measurements with the first three hits along the track and with the last three hits to agree.

Fig. 4.41 shows the correlation between rigidity, R, and velocity, β, for the charge $Z = +1$ events selected with the criteria described above. The average selection efficiency was $\sim 53\%$. The remaining background was subtracted using the distribution of the inverse of the momentum, $1/p$, which is approximately Gaussian. Events in the deuteron momentum range $0.9 < p < 3.0$ GeV/c and corresponding β range 0.4–0.85 were divided into nine velocity intervals $(\beta_i, \beta_i + \Delta\beta)$ with $\Delta\beta$ comparable with the velocity resolution. The corresponding nine $1/p$ histograms were plotted. The

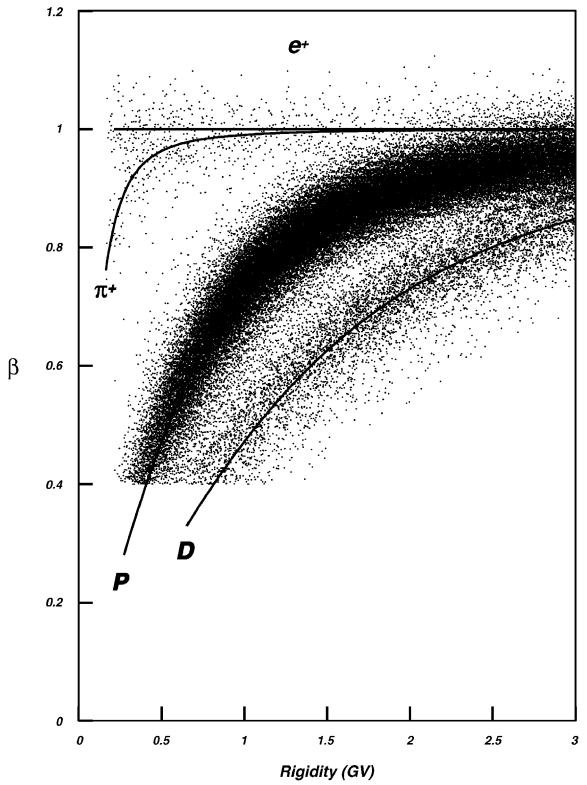

Fig. 4.41. Correlation between rigidity and velocity for selected $Z = +1$ particles. The deuteron selection was performed for rigidity < 3 GV.

proton and deuteron Monte Carlo simulations reproduced the $1/p$ histograms within 1–2%. A Gaussian fit to the $1/p$ data histograms was performed (Fig. 4.42). Finally the fitted proton background was subtracted from the data in each $1/p$ distribution. Fig. 4.43 shows the mass distribution for protons resulting from the Monte Carlo fit procedure and for deuterons after the proton background subtraction. The accepted deuterons are reconstructed in the mass range from 1.55 to 2.7 GeV/c^2 where the tail of subtracted protons was about $10 \pm 2\%$ at all energies, as seen from Fig. 4.44. After subtraction the residual background falls well below 1%.

4.6.2. Flux determination

The differential deuteron flux was determined by correcting the measured rates for the detector acceptance as a function of the momentum and the direction of the particles. The acceptance was restricted to events with an incident angle within 32° of the longitudinal AMS axis. Extensive simulations were performed in order to estimate the influence on the acceptance of deuteron nuclear interactions. The simulation of nuclear interactions took into account the following:

- The Glauber model [79] calculation of total and differential elastic scattering.
- Quasi-elastic scattering cross sections which were taken from the parameterization of the experimental data [80].

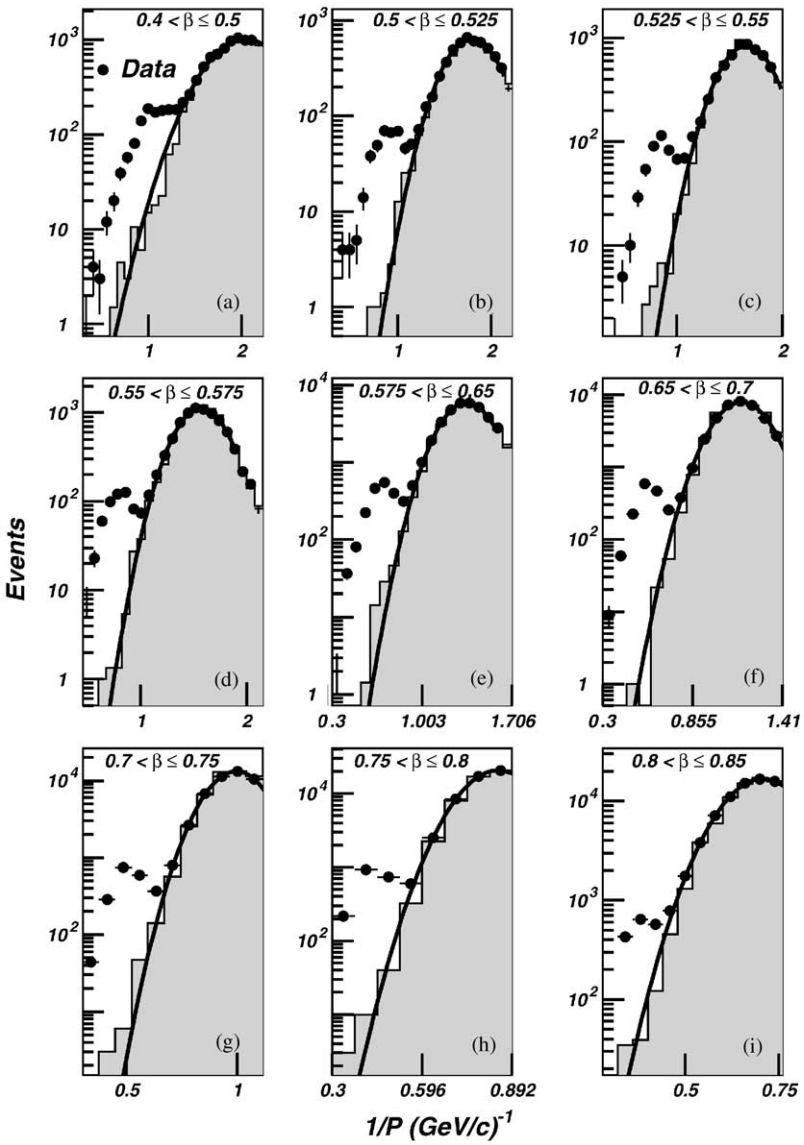

Fig. 4.42. $1/p$ histograms for nine β ranges: (a) $0.4 < \beta \leqslant 0.5$; (b) $0.5 < \beta \leqslant 0.525$; (c) $0.525 < \beta \leqslant 0.55$; (d) $0.55 < \beta \leqslant 0.575$; (e) $0.575 < \beta \leqslant 0.65$; (f) $0.65 < \beta \leqslant 0.7$; (g) $0.7 < \beta \leqslant 0.75$; (h) $0.75 < \beta \leqslant 0.8$; (i) $0.8 < \beta \leqslant 0.85$. Proton Monte Carlo (shaded histogram), Gaussian fit (line) and the data (full circles). The deuteron candidates appear on the left sides of the distributions.

- The inelastic scattering cross section which was calculated in the one-nucleon approximation, i.e. assuming that just one nucleon of the incident nucleus interacts with the target.

To simulate deuteron ionization losses and the secondaries produced by decay and fragmentation, the model [81] was interfaced with the AMS GEANT [16,41] simulation. The simulated deuteron

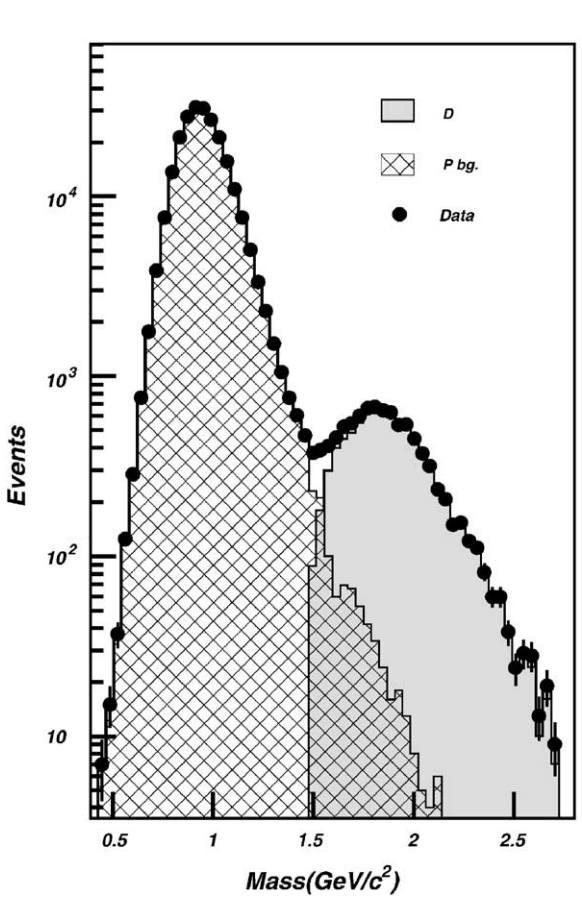

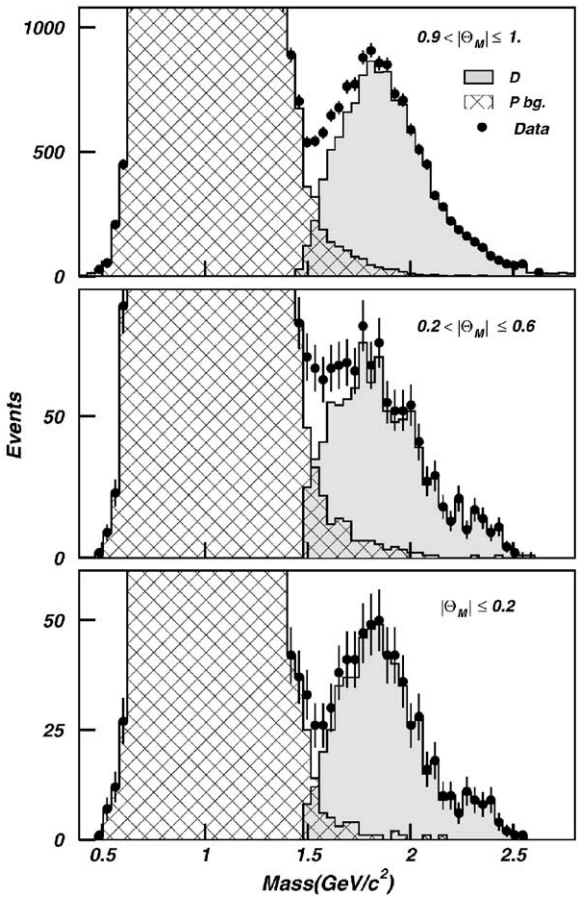

Fig. 4.43. Mass distribution for selected events ($|\Theta_{\mathrm{M}}| > 1$) for $\beta < 0.85$ and $R < 3$ GV. Full circles: total mass distribution before proton (P) and deuteron (D) separation; shaded histogram: deuterons; cross-hatched histogram: protons.

Fig. 4.44. Mass distribution for 0° attitude selected events for three different geomagnetic latitude samples. Full circles: total mass distribution before proton (P) and deuteron (D) separation; shaded histogram: deuterons; cross-hatched histogram: protons. The proton tail in deuteron mass region (mass $> 1.55\ \mathrm{GeV}/c^2$) is $\sim$9%, $\sim$13% and $\sim$10% of the total number of events, within respectively $0.8 < |\Theta_{\mathrm{M}}|$, $0.2 < |\Theta_{\mathrm{M}}| \leqslant 0.8$ and $|\Theta_{\mathrm{M}}| \leqslant 0.2$.

event samples were then required to pass through a trigger simulation and the reconstruction and selection chain as for data. The average acceptance was found to be $0.167\ \mathrm{m}^2$ sr in the energy range ($90 < E_{\mathrm{K}}/\mathrm{n} < 850\ \mathrm{MeV/n}$). Corrections to the acceptance due to trigger and selection criteria were found from unbiased events, and checked by comparing data and Monte Carlo samples. The overall correction due to deuteron interactions was found to be $11 \pm 3.5\%$.

The incident differential deuteron flux was obtained from the measured spectrum by unfolding detector resolution effects. The detector resolution function was obtained from the simulation and an unfolding procedure, based on Bayes' theorem [44], was used. The estimated average systematic errors are shown in Table 4.11.

Table 4.11
Average systematic uncertainties

Source	Error (%)
Full trigger and reconstruction	3.5
Particle interactions	3.5
Monte Carlo statistics	2
Selection and background subtraction	4
Unfolding	1
Overall	6.7

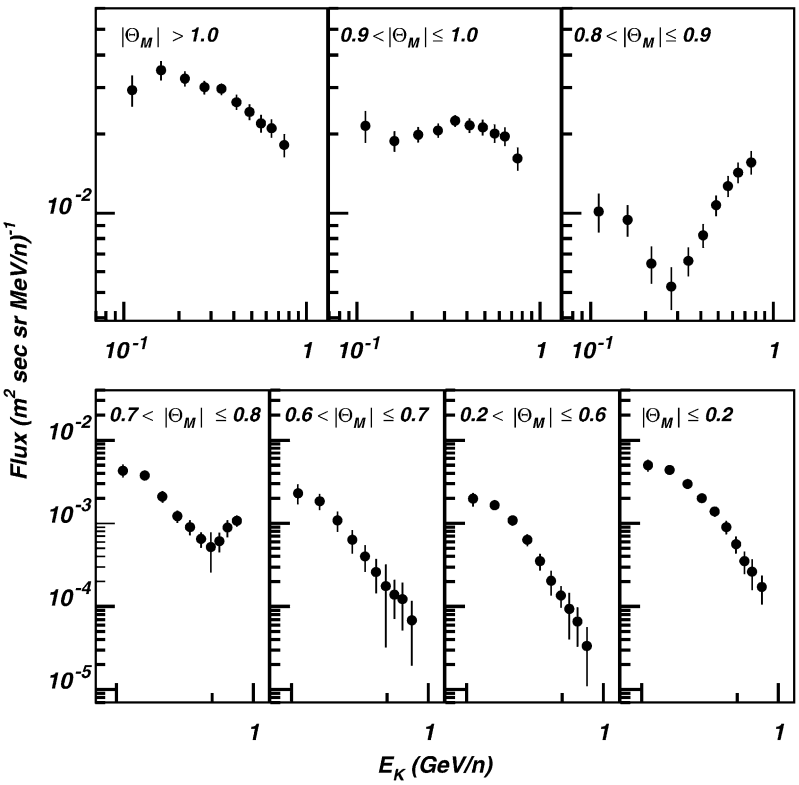

Fig. 4.45. Deuteron flux spectra separated by geomagnetic latitude Θ_{M}.

The differential deuteron spectra as a function of the incident kinetic energy per nucleon is presented in Fig. 4.45 for different geomagnetic latitude (Θ_{M}) ranges. The figure shows the presence of a primary (above cutoff) deuteron spectrum for $|\Theta_{\mathrm{M}}| > 1.0$; while for $|\Theta_{\mathrm{M}}| < 1.0$, the geomagnetic cutoff is clearly seen, and finally only a second (under cutoff) spectrum is left. The fluxes measured with the three shuttle orientations agree within the errors and were combined together. A total sample of $\sim 10^4$ deuterons above the geomagnetic cutoff for $|\Theta_{\mathrm{M}}| > 0.9$ was obtained, and the primary deuteron flux was determined as presented in Table 4.12.

Table 4.12
Differential primary deuteron flux in units of $(m^2\ s\ sr\ MeV)^{-1}$ versus kinetic energy per nucleon (E_K/n)

E_K/n (GeV/n)	Flux $\pm\ \varepsilon_{stat} \pm \varepsilon_{syst}$ $(m^2\ s\ sr\ MeV)^{-1}$
0.09–0.13	$(2.93 \pm 0.15 \pm 0.36) \times 10^{-2}$
0.13–0.19	$(3.49 \pm 0.17 \pm 0.24) \times 10^{-2}$
0.19–0.24	$(3.24 \pm 0.14 \pm 0.19) \times 10^{-2}$
0.24–0.31	$(3.00 \pm 0.13 \pm 0.15) \times 10^{-2}$
0.31–0.38	$(2.96 \pm 0.12 \pm 0.08) \times 10^{-2}$
0.38–0.45	$(2.64 \pm 0.12 \pm 0.12) \times 10^{-2}$
0.45–0.52	$(2.42 \pm 0.12 \pm 0.14) \times 10^{-2}$
0.52–0.60	$(2.19 \pm 0.08 \pm 0.15) \times 10^{-2}$
0.60–0.68	$(2.10 \pm 0.08 \pm 0.14) \times 10^{-2}$
0.68–0.85	$(1.81 \pm 0.05 \pm 0.17) \times 10^{-2}$

ε_{stat} stands for statistical error, ε_{syst} for energy dependent systematic error.

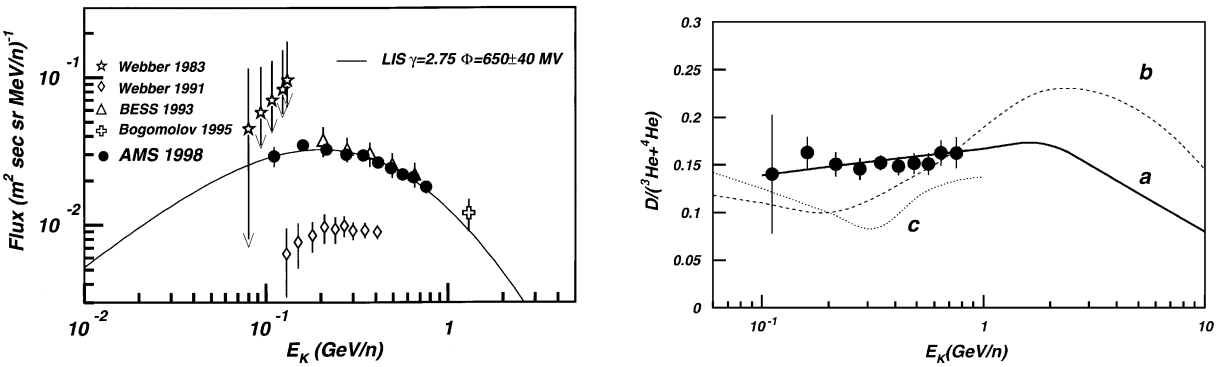

Fig. 4.46. Primary deuteron flux with previous measurements [73,76,78]. The solid curve represent the best fit of data with a LIS index of 2.75 and resulting in solar modulation parameter $\phi = 650 \pm 40$ MV. Data from [75] included for reference only.

Fig. 4.47. Deuteron-to-helium ratio as measured by AMS compared with three different model calculations: (a) From Stephens [55]; (b) Mewaldt [67]; (c) Seo et al. [56].

The primary deuteron spectrum is also shown in Fig. 4.46 together with previous measurements from balloon-borne experiments [73,76,78]. A power law in combination with the solar modulation equation suggested in [82] was fitted to the measured rigidity spectrum. The best fit was obtained when assuming a Local Interstellar Spectrum (LIS) with spectral index 2.75 and a modulation parameter $\phi = 650 \pm 40$ MV. The deuteron-to-helium ratio (Fig. 4.47) demonstrates the agreement between our measurements and calculations based on the Leaky Box Model [71]. However the agreement with other models [72,83] is less obvious.

The second, i.e. under cutoff, deuterium spectrum is given in Tables 4.13 and 4.14 for different shuttle orientations and different $|\Theta_M|$ values. All observed features were identical to the features

Table 4.13
The deuteron differential flux in units of $(m^2\ s\ sr\ MeV)^{-1}$, with statistical and systematic errors, as a function of kinetic energy per nucleon (E_K/n), detected at different geomagnetic latitudes Θ_M and with 0° shuttle pointing

E_K/n (GeV/n)	$0.9 < \lvert\Theta_M\rvert \leqslant 1.0$	$0.8 < \lvert\Theta_M\rvert \leqslant 0.9$	$0.7 < \lvert\Theta_M\rvert \leqslant 0.8$
0.09–0.13	$(21.4 \pm 1.2 \pm 2.7) \times 10^{-3}$	$(10.1 \pm 1.1 \pm 1.3) \times 10^{-3}$	$(43.1 \pm 5.5 \pm 5.3) \times 10^{-4}$
0.13–0.19	$(18.8 \pm 1.0 \pm 1.3) \times 10^{-3}$	$(9.4 \pm 1.1 \pm 0.6) \times 10^{-3}$	$(37.8 \pm 4.4 \pm 2.6) \times 10^{-4}$
0.19–0.24	$(19.9 \pm 0.8 \pm 1.0) \times 10^{-3}$	$(64.2 \pm 9.7 \pm 3.2) \times 10^{-4}$	$(20.9 \pm 3.3 \pm 1.0) \times 10^{-4}$
0.24–0.31	$(20.6 \pm 0.9 \pm 0.8) \times 10^{-3}$	$(52.7 \pm 9.5 \pm 2.1) \times 10^{-4}$	$(12.1 \pm 1.9 \pm 0.4) \times 10^{-4}$
0.31–0.38	$(22.4 \pm 0.9 \pm 0.6) \times 10^{-3}$	$(65.9 \pm 8.0 \pm 1.9) \times 10^{-4}$	$(90.4 \pm 18.1 \pm 2.7) \times 10^{-5}$
0.38–0.45	$(21.5 \pm 0.9 \pm 1.0) \times 10^{-3}$	$(82.4 \pm 7.6 \pm 3.9) \times 10^{-4}$	$(64.7 \pm 13.4 \pm 3.1) \times 10^{-5}$
0.45–0.52	$(21.1 \pm 0.9 \pm 1.1) \times 10^{-3}$	$(10.7 \pm 0.8 \pm 0.5) \times 10^{-3}$	$(51.7 \pm 25.8 \pm 2.7) \times 10^{-5}$
0.52–0.60	$(20.1 \pm 0.8 \pm 1.3) \times 10^{-3}$	$(12.7 \pm 0.7 \pm 0.8) \times 10^{-3}$	$(61.0 \pm 15.7 \pm 4.1) \times 10^{-5}$
0.60–0.68	$(19.5 \pm 0.8 \pm 1.3) \times 10^{-3}$	$(14.3 \pm 0.7 \pm 1.0) \times 10^{-3}$	$(88.5 \pm 19.2 \pm 6.1) \times 10^{-5}$
0.68–0.85	$(16.1 \pm 0.6 \pm 1.5) \times 10^{-3}$	$(15.6 \pm 0.6 \pm 1.4) \times 10^{-3}$	$(10.7 \pm 1.3 \pm 1.0) \times 10^{-4}$
E_K(GeV/n)	$0.6 < \lvert\Theta_M\rvert \leqslant 0.7$	$0.2 < \lvert\Theta_M\rvert \leqslant 0.6$	$0.0 \leqslant \lvert\Theta_M\rvert \leqslant 0.2$
0.09–0.13	$(23.1 \pm 5.4 \pm 3.4) \times 10^{-4}$	$(19.7 \pm 2.7 \pm 2.9) \times 10^{-4}$	$(49.8 \pm 4.9 \pm 7.4) \times 10^{-4}$
0.13–0.19	$(18.5 \pm 3.9 \pm 1.2) \times 10^{-4}$	$(16.6 \pm 1.8 \pm 1.1) \times 10^{-4}$	$(43.7 \pm 4.3 \pm 3.0) \times 10^{-4}$
0.19–0.24	$(10.8 \pm 2.9 \pm 0.5) \times 10^{-4}$	$(10.8 \pm 1.3 \pm 5.4) \times 10^{-4}$	$(29.8 \pm 2.9 \pm 1.5) \times 10^{-4}$
0.24–0.31	$(63.1 \pm 19.6 \pm 2.5) \times 10^{-5}$	$(63.1 \pm 9.9 \pm 2.5) \times 10^{-5}$	$(20.0 \pm 2.3 \pm 0.8) \times 10^{-4}$
0.31–0.38	$(39.9 \pm 14.0 \pm 1.1) \times 10^{-5}$	$(35.1 \pm 7.9 \pm 0.9) \times 10^{-5}$	$(13.8 \pm 1.8 \pm 0.4) \times 10^{-4}$
0.38–0.45	$(25.9 \pm 11.0 \pm 1.2) \times 10^{-5}$	$(20.2 \pm 6.6 \pm 0.9) \times 10^{-5}$	$(90.4 \pm 15.8 \pm 4.3) \times 10^{-5}$
0.45–0.52	$(17.5 \pm 13.6 \pm 0.9) \times 10^{-5}$	$(13.5 \pm 3.8 \pm 0.7) \times 10^{-5}$	$(56.4 \pm 12.6 \pm 2.9) \times 10^{-5}$
0.52–0.60	$(14.0 \pm 5.8 \pm 0.9) \times 10^{-5}$	$(9.3 \pm 5.2 \pm 0.6) \times 10^{-5}$	$(35.1 \pm 10.4 \pm 2.3) \times 10^{-5}$
0.60–0.68	$(12.2 \pm 5.9 \pm 0.8) \times 10^{-5}$	$(6.5 \pm 3.2 \pm 0.4) \times 10^{-5}$	$(26.2 \pm 10.3 \pm 1.8) \times 10^{-5}$
0.68–0.85	$(6.7 \pm 4.7 \pm 0.6) \times 10^{-5}$	$(3.3 \pm 2.2 \pm 0.3) \times 10^{-5}$	$(17.1 \pm 6.4 \pm 1.6) \times 10^{-5}$

observed in the case of the second spectrum protons and were described in detail in the corresponding sections.

5. Conclusions

The main objectives of the precursor flight were achieved. The AMS detector was successfully operated in space. The radiation environment as well as background conditions for the International Space Station flight have been understood.

During the 10 day precursor flight a number of measurements in cosmic ray physics were performed. In particular the upper limit on the antimatter presence in cosmic rays was improved and the proton spectrum was measured with high precision. Detailed studies of particles with so called forbidden trajectories, i.e. when rigidities are below the local geomagnetic cutoff, were performed. The measurements by AMS in near Earth orbit (at 380 km from the Earth's surface), between the atmosphere and the radiation belts, show that the particles in this region follow a complicated path in the Earth's magnetic field. This behavior is different from that extrapolated from satellite observations in the radiation belts, where the protons bounce across the equator for a much longer time. It is

Table 4.14
The deuteron differential flux in units of $(m^2\ s\ sr\ MeV)^{-1}$, with statistical and systematic errors versus kinetic energy per nucleon (E_K/n), detected at geomagnetic latitude $0.2 < |\Theta_M| \leqslant 0.6$ and $0.0 \leqslant |\Theta_M| \leqslant 0.2$ at the shuttle attitudes 180°, 20° and 45°

E_K/n (GeV/n)	$0.0 \leqslant \lvert\Theta_M\rvert \leqslant 0.2$		
	180°	20°	45°
0.09–0.13	$(49.5 \pm 10.0 \pm 7.4) \times 10^{-4}$	$(42.3 \pm 4.2 \pm 5.2) \times 10^{-4}$	$(29.7 \pm 4.1 \pm 3.7) \times 10^{-4}$
0.13–0.19	$(40.7 \pm 6.4 \pm 2.8) \times 10^{-4}$	$(37.1 \pm 4.1 \pm 2.5) \times 10^{-4}$	$(26.0 \pm 3.4 \pm 1.8) \times 10^{-4}$
0.19–0.24	$(25.7 \pm 4.9 \pm 1.2) \times 10^{-4}$	$(27.5 \pm 2.9 \pm 1.3) \times 10^{-4}$	$(20.2 \pm 3.1 \pm 1.0) \times 10^{-4}$
0.24–0.31	$(17.4 \pm 3.1 \pm 0.6) \times 10^{-4}$	$(17.9 \pm 2.2 \pm 0.7) \times 10^{-4}$	$(12.5 \pm 2.2 \pm 0.5) \times 10^{-4}$
0.31–0.38	$(12.1 \pm 2.5 \pm 0.3) \times 10^{-4}$	$(10.1 \pm 2.0 \pm 0.3) \times 10^{-4}$	$(83.7 \pm 16.3 \pm 2.5) \times 10^{-5}$
0.38–0.45	$(75.4 \pm 21.8 \pm 3.6) \times 10^{-5}$	$(56.0 \pm 13.8 \pm 2.6) \times 10^{-5}$	$(51.6 \pm 15.5 \pm 2.4) \times 10^{-5}$
0.45–0.52	$(48.6 \pm 22.7 \pm 2.5) \times 10^{-5}$	$(37.7 \pm 13.2 \pm 1.9) \times 10^{-5}$	$(32.6 \pm 9.7 \pm 1.6) \times 10^{-5}$
0.52–0.60	$(32.9 \pm 13.4 \pm 2.2) \times 10^{-5}$	$(31.5 \pm 8.9 \pm 2.1) \times 10^{-5}$	$(22.5 \pm 9.1 \pm 1.5) \times 10^{-5}$
0.60–0.68	$(26.1 \pm 14.6 \pm 1.8) \times 10^{-5}$	$(28.8 \pm 9.1 \pm 2.0) \times 10^{-5}$	$(16.4 \pm 12.2 \pm 1.1) \times 10^{-5}$
0.68–0.85	$(13.5 \pm 8.4 \pm 1.2) \times 10^{-5}$	$(17.5 \pm 6.2 \pm 1.6) \times 10^{-5}$	$(9.8 \pm 4.4 \pm 0.9) \times 10^{-5}$

E_K/n (GeV/n)	$0.2 < \lvert\Theta_M\rvert \leqslant 0.6$		
	180°	20°	45°
0.09–0.13	$(21.0 \pm 4.4 \pm 3.2) \times 10^{-4}$	$(27.2 \pm 2.1 \pm 4.1) \times 10^{-4}$	$(30.2 \pm 2.4 \pm 4.0) \times 10^{-4}$
0.13–0.19	$(17.4 \pm 2.6 \pm 1.2) \times 10^{-4}$	$(22.8 \pm 1.9 \pm 1.5) \times 10^{-4}$	$(25.2 \pm 2.0 \pm 1.4) \times 10^{-4}$
0.19–0.24	$(10.6 \pm 2.1 \pm 0.5) \times 10^{-4}$	$(15.5 \pm 1.8 \pm 0.7) \times 10^{-4}$	$(15.0 \pm 1.7 \pm 0.7) \times 10^{-4}$
0.24–0.31	$(53.6 \pm 14.9 \pm 2.1) \times 10^{-5}$	$(78.4 \pm 11.5 \pm 3.1) \times 10^{-5}$	$(83.9 \pm 11.7 \pm 3.0) \times 10^{-5}$
0.31–0.38	$(29.6 \pm 9.2 \pm 0.8) \times 10^{-5}$	$(41.5 \pm 9.0 \pm 1.2) \times 10^{-5}$	$(53.5 \pm 9.7 \pm 1.6) \times 10^{-5}$
0.38–0.45	$(17.1 \pm 7.6 \pm 0.8) \times 10^{-5}$	$(24.7 \pm 6.8 \pm 1.1) \times 10^{-5}$	$(32.6 \pm 6.8 \pm 1.5) \times 10^{-5}$
0.45–0.52	$(11.9 \pm 4.1 \pm 0.6) \times 10^{-5}$	$(17.7 \pm 5.0 \pm 0.9) \times 10^{-5}$	$(20.3 \pm 5.0 \pm 1.0) \times 10^{-5}$
0.52–0.60	$(10.1 \pm 4.8 \pm 0.6) \times 10^{-5}$	$(12.8 \pm 4.9 \pm 0.8) \times 10^{-5}$	$(13.3 \pm 4.9 \pm 0.9) \times 10^{-5}$
0.60–0.68	$(8.2 \pm 5.3 \pm 0.5) \times 10^{-5}$	$(9.1 \pm 4.1 \pm 0.6) \times 10^{-5}$	$(10.4 \pm 4.0 \pm 0.7) \times 10^{-5}$
0.68–0.85	$(4.7 \pm 3.0 \pm 0.4) \times 10^{-5}$	$(4.1 \pm 2.3 \pm 0.4) \times 10^{-5}$	$(7.7 \pm 2.3 \pm 0.7) \times 10^{-5}$

also different from that extrapolated from balloon observations in the upper layer of the atmosphere, where the protons (or electrons) typically cross the equator once.

There are several new and unexpected observations related to the second spectrum beside the accurate measurement of the second spectrum itself:

- The presence of the two distinctly different types of particle trajectories, long-lived and short-lived.
- The long-lived component originates from a well defined geographic region.
- The predominance of positrons over electrons.
- The presence of almost pure ^{3}He isotope in near Earth orbit.

Some of these observations were understood to be the consequences of the primary cosmic ray interactions with the atmosphere and the Earth's magnetic field, others are still awaiting quantitative analysis.

The AMS shuttle flight has proved the accurate, high statistics, long duration measurements of energetic charged cosmic ray spectra are possible in real space flight conditions.

The AMS-02 experiment (see Fig. 1.2a) is being constructed based on the operational experience of AMS-01. The detector construction will be completed in 2003 and the construction of the super-conducting magnet will be completed in 2005. After intensive beam tests at CERN the detector will be installed on ISS in 2004.

In three years on the ISS the data estimated to be collected include approximately 2×10^9 helium events up to 3 TeV, $\sim 10^6$ proton events above 1 TeV, $\sim 10^6$ antiproton events above 5 GeV, $\sim 10^7$ electrons up to 1.4 TeV and $\sim 2 \times 10^6$ positrons above 5 GeV. This will provide us with a sensitive search for antimatter and dark matter up to the highest energies.

Acknowledgements

The success of the first AMS mission is due to many individuals and organizations outside of the collaboration. The support of NASA was vital in the inception, development and operation of the experiment. The dedication of Douglas P. Blanchard, Mark J. Sistilli, James R. Bates, Kenneth Bollweg and the NASA and Lockheed–Martin Mission Management team, the support of the Max–Planck Institute for Extraterrestrial Physics, the support of the space agencies from Germany (DLR), Italy (ASI), France (CNES) and China and the support of CSIST, Taiwan, made it possible to complete this experiment on time.

We are most grateful to the STS-91 astronauts, particularly to Dr. Franklin Chang-Diaz who provided vital help to AMS during the flight.

References

[1] A.D. Sakharov, JETP Lett. 5 (1967) 24;
A.D. Dolgov, Ya.B. Zeldovich, et al., Rev. Mod. Phys. 53 (1981) 1;
E.W. Kolb, M.S. Turner, Annu. Rev. Nucl. Part. Sci. 33 (1983) 645;
A.D. Dolgov, Phys. Rep. 222 (1992) 309;
D. Comelli, et al., Nucl. Phys. B 412 (1994) 441;
A.D. Dolgov, J. Silk, Phys. Rev. D 47 (1993) 4244;
M.Yu. Khlopov, Gravitation Cosmol. 4 (1998) 69–72;
A.G. Cohen, et al., Astrophys. J. 495 (1998) 539–549;
J. Rehm, K. Jedamzik, et al., Phys. Rev. Lett. 81 (1998) 3307–3310;
A.D. Dolgov, Lecture at 25th ITEP Winter School, hep-ph/9707419, 1997;
W. Kinney, et al., Phys. Rev. Lett. 79 (1997) 2620;
M.Yu. Khlopov, et al., Phys. Rev. D 62 (2000) 083505;
J. Rehm, K. Jedamzik, et al., arXiv: astro-ph/0006381, 2001.
[2] G.F. Smoot, et al., Phys. Rev. Lett. 35 (1975) 258–261;
G. Steigman, et al., Annu. Rev. Astron. Astrophys. 14 (1976) 339;
G. Badhwar, et al., Nature 274 (1978) 137;
A. Buffington, et al., Astrophys. J. 248 (1981) 1179–1193;
R.L. Golden, et al., Astrophys. J. 479 (1997) 992;
J.F. Ormes, et al., Astrophys. Lett. 482 (1997) 187.
[3] T. Saeki, et al., Phys. Lett. B 422 (1998) 319.
[4] L. Bergström, Rep. Prog. Phys. 63 (2000) 793–841.

[5] S. Ahlen, et al., Nucl. Instr. and Meth. A 350 (1994) 351.
[6] S.C.C. Ting, in: K. Huitu, M. Chaian, R. Orava (Eds.), The First Arctic Workshop on Future Physics and Accelerators, World Scientific, Singapore, 1995, pp. 1–26.
[7] D. Alvisi, et al., Nucl. Instr. and Meth. A 437 (1999) 212–221.
[8] G.K. Parks, An Introduction, Addison-Wesley, Reading, MA, 1991.
[9] G. Batignani, et al., Nucl. Instr. and Meth. A 277 (1989) 147.
[10] M. Acciarri, et al., Nucl. Instr. and Meth. A 351 (1994) 300.
[11] J.B. England, et al., Nucl. Instr. and Meth. 185 (1981) 43.
[12] J. Alcaraz, et al., Nouvo Cimento II 112A (1999) 1325–1344.
[13] F. Barao, et al., Analysis of the Aerogel Thershold Čerenkov data from AMS flight (STS-91), AMSnote-99-38, ISN 99.84, LAPP-EXP-99.06, November 3, 1999;
D. Barancourt, et al., Nucl. Instr. and Meth. A 454 (2000) 174–179.
[14] J.C. Hart, D.H. Saxon, Nucl. Instr. and Meth. 220 (1984) 309.
[15] AMS collaboration, J. Alcaraz, et al., Phys. Lett. B 461 (1999) 387–396.
[16] R. Brun, et al., GEANT 3, CERN DD/EE/84-1, Revised, 1987.
[17] A.A. Moiseev, J.F. Ormes, Astropart. Phys. 6 (1997) 379–386.
[18] Stanley C. Freden, R. Stephen White, Phys. Rev. Lett. 3 (1959) 9;
B.J. Teegarden, J. Geophys. Res. 72 (1967) 4857;
M.J. Ryan, Phys. Rev. Lett. 15 (1972) 985;
L.H. Smith, et al., Astrophys. J. 180 (1973) 987;
G.F. Smooth, et al., J. Geophys. Res. 10 (1973) 730;
R.E. Steitmatter, et al., Proceedings of the 21st ICRC, Vol. 3, 1990, p. 277;
F.B. McDonald, et al., Proceedings of the 21st ICRC, Vol. 6, 1990, p. 144;
M. Ichimura, et al., Phys. Rev. D 48 (1993) 1949;
J. Chen, et al., Adv. Space Res. 14 (1994) 10 765;
S.P. Swordy, et al., Proceedings of the 24th ICRC, Vol. 2, 1995, p. 652;
W. Mennet, et al., Proceedings of the 25th ICRC, Vol. 3, 1997, p. 409;
R. Bellotti, et al., Phys. Rev. D 60 (1999) 052002.
[19] S.D. Verma, J. Geophys. Res. 72 (1967) 915.
[20] W.R. Webber, Proceedings of the 20 ICRC, Vol. 2, 1987, p. 80.
[21] E.S. Seo, et al., Astrophys. J. 378 (1991) 763.
[22] P. Papini et al., Proceedings of the 23rd ICRC, Vol. 1, 1993, p. 579.
[23] M. Boesio, et al., Astrophys. J. 518 (1999) 457.
[24] B. Wiebel-Sooth, P.L. Biermann, H. Meyer, Astron. Astrophys. 330 (1998) 389.
[25] J.B. Cladis, et al., J. Geophys. Res. 66 (1961) 2297;
L.V. Kurnosova et al., Proceedings of the 15 ICRC, Plovdiv, Vol. 4, 1977, p. 185;
R.N. Basilova et al., Proceedings of the 16 ICRC, Kyoto, Vol. 3, 1979, p. 150;
N.L. Grigorov, et al., Dokl. Akad. Nauk SSSR 282 (1985) 81;
Yu.E. Efimov, et al., Chechoslovak J. Phys. 35 (1985) 1371;
S.A. Voronov, et al., Izv. Vyssh. Uchebn. Zaved. Fiz. 9 (1986) 19–24;
S.A. Voronov, et al., Geomagn. Aeronomy 27 (1987) 424;
A.F. Iydin, et al., Geomagn. Aeronomy 28 (1988) 103;
S.V. Koldashov, et al., Proceedings of the 24 ICRC, Roma, Vol. 4, 1995, p. 993;
A.M. Galper, et al., Proceedings of the 25 ICRC, Durban, Vol. 4, 1997, p. 333.
[26] P.L. Biermann, et al., Phys. Rev. D 51 (1995) 3450.
[27] W.R. Webber, J.A. Lezniak, Astrophys. Space Sci. 30 (1974) 361.
[28] J. Buckley, et al., Astrophys. J. 429 (1994) 736–747.
[29] K. Asakimori, et al., Proceedings of the 23rd ICRC, Calgary, Vol. 2, 1993, p. 25.
[30] K. Asakimori, et al., Astrophys. J. 502 (1998) 278.
[31] Y. Fukuda, et al., Phys. Lett. B 436 (1998) 33–41;
M. Honda, et al., Phys. Rev. D 52 (1995) 4985;
G. Battistoni, et al., Astropart. Phys. 12 (2000) 315–333;

Y. Tserkovnyak et al., A three-dimensional calculation of atmospheric neutrino fluxes, hep-ph/9907450, 1999;
P. Lipari, The primary protons and the atmospheric neutrino fluxes, hep-ph/9905506, 1999;
T. Gaisser, Nucl. Phys. Proc. Suppl. 87 (2000) 141–151;
N. Fornengo, et al., Nucl. Phys. B 580 (2000) 58–82.
[32] R.R. Daniel, S.A. Stephens, Phys. Rev. Lett. 15 (1965) 769;
C.J. Bland, et al., Phys. Rev. Lett. 17 (1966) 813;
C.J. Bland, et al., Nouvo Cimento LV B (1968) 451;
B. Agrinier, et al., Nouvo Cimento Lett. 1 (1969) 54;
J.L. Fanselow, et al., Astrophys. J. 158 (1969) 771;
J. Daugherty, et al., Astrophys. J. 198 (1975) 493;
A. Buffington, et al., Astrophys. J. 199 (1975) 669;
R. Hartman, C. Pellerin, Astrophys. J. 204 (1976) 927;
K.K. Tang, Astrophys. J. 278 (1984) 881;
R.L. Golden, et al., Astrophys. J. 287 (1985) 662;
D. Muller, K. Tang, Astrophys. J. 312 (1987) 183;
G. Barbiellini, et al., Astron. Astrophys. 309 (1996) L15;
R.L. Golden, et al., Astrophys. J. 457 (1996) L103;
S.W. Barwick, et al., Astrophys. J. 482 (1997) L191;
S. Torri, et al., Proceedings of the 26th ICRC, Vol. 3, 1999, p. 53;
M. Boezio, et al., Proceedings of the 26th ICRC, Vol. 3, 1999, p. 57;
S. Coutu, et al., Astropart. Phys. 11 (1999) 429.
[33] R.L. Golden, et al., Astrophys. J. 436 (1994) 769;
S.W. Barwick, et al., Astrophys. J. 498 (1998) 779;
M.A. DuVernois, et al., Proceedings of the 26th ICRC, Vol. 3, 1999, p. 49.
[34] S.W. Barwick, et al., J. Geophys. Res. 103 (1998) 4817.
[35] O.A. Bogdanova, et al., Proceedings of the 15 ICRC, Plovdiv, Vol. 3, 1977, p. 176;
M. Giler, et al., J. Phys. A 10 (1977) 843;
R.J. Protheroe, Astrophys. J. 254 (1982) 391.
[36] I.V. Moskalenko, A.W. Strong, Astrophys. J. 493 (1998) 694.
[37] AMS collaboration, J. Alcaraz, et al., Phys. Lett. B 472 (2000) 215–226.
[38] AMS collaboration, J. Alcaraz, et al., Phys. Lett. B 490 (2000) 27–35.
[39] AMS collaboration, J. Alcaraz, et al., Phys. Lett. B 494 (2000) 193–202.
[40] AMS collaboration, J. Alcaraz, et al., Phys. Lett. B 484 (2000) 10–22.
[41] P.A. Aamio, et al., FLUKA Users Guide, CERN TIS-RP-190, 1990.
[42] V. Innocente, M. Maire, E. Nagy, GEANE: Average Tracking and Error Propagation Package, CERN Program Library W5013-E, 1991.
[43] A. Kondor, Nucl. Instr. and Meth. 216 (1983) 177.
[44] G. D'Agostini, Nucl. Instr. and Meth. A 362 (1995) 487.
[45] V. Blobel, Unfolding Methods in High Energy Physics, in: Proceedings of the 1984 CERN School of Computing, CERN 85-09, 1985.
[46] A. Brekke, Physics of the Upper Polar Atmosphere, Wiley, New York, 1997, pp. 127–145.
[47] V.F. Turchin, V.A. Nozik, Izv. Acad. Nauk USSR Ser. Fiz. 5 (1969) 29;
V.F. Turchin, V.P. Kozlov, M.S. Malkevich, Phys. Usp. 102 (2) (1970) 345.
[48] M.A. Huang, et al., Chinese J. Phys. 39 (2001) 1–11.
[49] N.A. Tsyganenko, A.V. Usmanov, Planet. Space. Sci. 30 (1982) 985–998;
N.A. Tsyganenko, et al., Unknown, Software for Computations of Geomagnetic Field and Related Coordinate Systems, Soviet Geophysical Committee, Special Report, 1987;
N.A. Tsyganenko, Planet. Space Sci. 35 (1987) 1347–1358;
N.A. Tsyganenko, Planet. Space Sci. 37 (1989) 5–20;
N.A. Tsyganenko, J. Geophys. Res. 100 (1995) 5599–5612;
N.A. Tsyganenko, D.P. Stern, J. Geophys. Res. 101 (1996) 27187–27198;

R.L. Langel, Chairman, IAGA Div. V Working Group 8, J. Geomag. Geoelectr. 47 (1995) 1251–1261;
G. Gustafsson, N.E. Papitashvili, V.O. Papitashvili, J. Atmos. Terr. Phys. 54 (1992) 1609–1631.
[50] V.L. Ginzburg, V.S. Ptuskin, Rev. Mod. Phys. 48 (1976) 161.
[51] W.R. Webber, et al., Astrophys. J. 390 (1991) 96–104.
[52] A.D. Erlykin, A.W. Wolfendale, Eur. J. Phys. 20 (1999) 409–418.
[53] T. Sanuki, et al., Astrophys. J. 545 (2000) 1135.
[54] W. Menn, et al., Astrophys. J. 533 (2000) 281.
[55] A.D. Erlykin, et al., Phys. Lett. B 482 (2000) 337–342.
[56] S.B. Treiman, Phys. Rev. 91 (1953) 957;
E.C. Ray, J. Geophys. Res. 67 (1962) 3289.
[57] S.B. Treiman, Phys. Rev. 93 (1954) 544.
[58] P. Lipari, The fluxes of sub-cutoff particles detected by AMS, the cosmic ray albedo and atmospheric neutrinos, astro-ph/0101559, 31 January 2001.
[59] M.H. Israel, J. Geophys. Res. 74 (1969) 4701.
[60] J.P. Wefel, et al., Proceedings of the 24th ICRC, Vol. 4, 1995, p. 1021.
[61] J. Chen, et al., Geophys. Res. Lett. 21 (1994) 1583;
M.D. Looper, et al., Radiat. Meas. 26 (1996) 967;
R.S. Selesnick, R.A. Mewaldt, J. Geophys. Res. 101 (1996) 19745–19757.
[62] L. Derome, et al., Phys. Lett. B 489 (2000) 1–8.
[63] L. Derome, et al., Phys. Lett. B 515 (2001) 1–5.
[64] L. Derome, M. Buenerd, Origin of light nuclei in near earth orbit, Phys. Lett. B 521 (2001) 139.
[65] E. Fiandrini, et al., Talk at International School Of Astroparticle Physics, Workshop on Space For Peace Technology: Physics with AMS, Erice, Sicily, May 06–14; astro-ph/0106241, 2000.
[66] V. Plyaskin, Phys. Lett. B 516 (2001) 213–235.
[67] P. Zuccon, et al., A Monte Carlo simulation of the interactions of cosmic rays with the atmosphere, CERN-OPEN-2001-068, 2001.
[68] G. Jungman, M. Kamionkowski, Phys. Rev. D 49 (1994) 2316;
A. Bottino, et al., Astropart. Phys. 3 (1995) 77.
[69] L. Bergstrom, et al., Astrophys. J. 526 (1999) 215.
[70] S. Orito, et al., Phys. Rev. Lett. 84 (2000) 1078.
[71] S.A. Stephens, Adv. Space Res. 9 (1989) 145.
[72] E.S. Seo, et al., Astrophys. J. 432 (1994) 656.
[73] W.R. Webber, S.M. Yushak, Astrophys. J. 275 (1983) 391.
[74] R. Kroeger, Astrophys. J. 303 (1986) 816;
K.C. Hsieh, J.A. Simpson, Astrophys. J. 158 (1969) L37;
J.J. Beatty, Astrophys. J. 311 (1986) 425;
R.A. Mewaldt, E.C. Stone, R.E. Vogt, Astrophys. J. 206 (1976) 616;
M. Garcia-Munoz et al., Proceedings of the 14th ICRC, Vol. 1, 1975, p. 319.
[75] W.R. Webber, et al., Astrophys. J. 380 (1991) 230–234;
P.S. Freier, C.J. Waddington, J. Geophys. Res. 73 (1969) 4261.
[76] E.A. Bogomolov et al., Proceedings of the 24th ICRC, Vol. 2, 1995, p. 598.
[77] E.A. Bogomolov, Proceedings of the 16th ICRC, Vol. 1, 1979, p. 330;
R.L. Golden, et al., Proceedings of the 19th ICRC, Vol. 2, 1985, p. 68;
K.M.V. Apparao, Proceedings of the 13th ICRC, Vol. 1, 1973, p. 126.
[78] E.S. Seo, et al., Adv. Space Res. 19 (1997) 751.
[79] R.J. Glauber, in: W.E. Brittin, et al. (Eds.), Lectures in Theoretical Physics, Vol. 1. New York, 1959, p. 315;
S. Forte, Nucl. Phys. A 467 (1987) 665;
S.Yu. Shmakov, et al., Comput. Phys. Commun. 54 (1988) 125;
A.S. Pak, et al., Sov. J. Nucl. Phys. 30 (2) (1979) 178;
I.V. Andreev, A.V. Chernov, Sov. J. Nucl. Phys. 28 (2) (1978) 243;
Z. Omboo, et al., Unknown, JINR-E, 90-21, 1990;
G. Faldt, I. Hulthage, Nucl. Phys. A 316 (1979) 251.

[80] L.S. Azhgieri, et al., Sov. J. Nucl. Phys. 30 (6) (1979) 818;
J.P. Burg, et al., Nucl. Phys. B 187 (1981) 205;
A. Bujak, et al., Phys. Rev. D 23 (1981) 1895;
V. Franco, Phys. Rev. C 6 (1972) 748;
G.D. Alkhazov, et al., Nucl. Phys. A 280 (1977) 365;
W. Bell, et al., Phys. Lett. B 117 (1982) 131;
J. Jaros, et al., Phys. Rev. C 18 (1978) 2273;
V.G. Ableev, et al., Z. Phys. A 340 (1991) 340;
V.G. Ableev, et al., Acta Phys. Pol. B 16 (1985) 913;
L. Satta, et al., Phys. Lett. B 139 (1984) 263.
[81] H. Sorge, Phys. Rev. C 52 (1995) 3291.
[82] L.J. Gleeson, W.I. Axford, Astrophys. J. 154 (1968) 1011.
[83] R.A. Mewaldt, Proceedings at Cosmic Abundance of Matter Conference, Vol. 183, 1989, p. 124.